Synthesis and Sintering of Nanocrystalline Alumina and Aluminum Nitride

by

Martin Lawrence Panchula

M.S. Materials Science, Iowa State University, 1994

B.S. Ceramic Engineering, Iowa State University, 1994

Submitted to the Department of Materials Science and Engineering in Partial Fulfillment of the Requirements for the Degree of

Doctor of Philosophy in Ceramics

at the

MASSACHUSETTS INSTITUTE OF TECHNOLOGY

September 1999

Signature of Author:_____
Department of Materials Science and Engineering
August 6, 1999

Certified by:_____
Jackie Y. Ying
Associate Professor of Chemical Engineering
Thesis Supervisor

Read by:_____
Yet-Ming Chiang
Kyocera Professor of Ceramics

Accepted by:_____
Linn W. Hobbs
John F. Elliott Professor of Materials
Chairman, Departmental Committee on Graduate Students

Synthesis and Sintering of Nanocrystalline Alumina and Aluminum Nitride

by

Martin Lawrence Panchula

Submitted to the Department of Materials Science & Engineering
on August 6, 1999 in Partial Fulfillment of the Requirements
for the Degree of Doctor of Philosophy in Ceramics

Abstract

The use of nanocrystalline particles can greatly increase the sinterability and properties of many ceramic materials. This work focused on the synthesis and processing of nanocrystalline alumina (Al_2O_3) and aluminum nitride (AlN). Nanocrystalline transitional Al_2O_3 is very easy to synthesize, however it sinters poorly due to a low nucleation density of the α-phase during heating. This makes final densification difficult and temperatures >1600°C are necessary to attain >98% of theoretical density. Previous investigators have found that adding seed particles can greatly increase the kinetics of the transformation, reduce the crystallite size, and enhance densification significantly. This work examined the use of high-energy ball milling to mechanically transform a small fraction of the transitional γ-Al_2O_3 nanocrystalline particles to α-Al_2O_3 seeds. This in-situ formation of α-Al_2O_3 greatly increased the transformation rate and lowered the transformation temperature, thereby improving powder densification.

Conventional coarse-grained AlN typically requires high temperatures (~1900°C) or the use of oxide additives in order to achieve full densification and high thermal conductivity. Unfortunately, AlN is very hygroscopic and its thermal conductivity is very sensitive to the oxygen content so that less than 1 wt% oxygen can reduce the thermal conductivity by over 30%. This thesis investigated the synthesis and processing of nanocrystalline AlN to promote sintering of high-purity nitride ceramics. A forced-flow reactor was used to produce nanocrystalline AlN, and the effects of the reactor variables on the powder purity, surface area, crystallite size, and morphology were evaluated. Through careful synthesis and processing, it was possible to achieve high-density AlN (>95%) via pressureless, additive-free sintering by 1700°C. The influence of yttria (Y_2O_3) additions on the AlN densification was also investigated, and it was found that the effectiveness of the additive depended strongly on the Y_2O_3 particle size. The sintered AlN ceramic attained in this study has a very low oxygen content and high thermal conductivity. Another interesting aspect of this research was the discovery that nanocrystalline AlN, when produced under certain conditions, could be formed into a highly textured material when

hot pressed. Such bulk textured AlN materials are unique, and offer interesting possibilities for piezoelectric applications, especially at high temperatures.

Thesis Supervisor: Jackie Y. Ying
Title: Associate Professor of Chemical Engineering

Acknowledgments

I thank my advisor, Professor Jackie Ying, for the opportunity to work in her laboratory with an exceptional group of researchers. The effort required to support such a group is very much appreciated. I also thank my committee members, Professors Yet-Ming Chiang and Sam Allen, for their helpful discussions and interest in this research.

I appreciate the friendship and assistance of Dr. Darren Castro, the designer and builder of the forced-flow reactor that made the research on nanocrystalline AlN possible. I thank Beatrice Wang for her help with the mechanical seeding and hot pressing of γ-Al_2O_3. The assistance of Andrey Zarur for high-resolution TEM and light scattering studies and Michael Wong and Mark Fokema for photoacoustic FTIR and DRIFT measurements is greatly appreciated. The efforts of undergraduate students Jessica West, Reginald Rogers, and Ranjit Survanshi, are also acknowledged. Finally, the friendship and assistance of the many other members of the group must be recognized; without their presence the lab would have certainly been a less interesting and educational place to work.

My thanks are also extended to Vista Chemical Company and H. C. Starck, Inc. for samples of their products. Special thanks are given to Mike Frongillo of the Center for Materials Science and Engineering for all his assistance and patient training with the electron microscopes.

Finally, my greatest appreciation is reserved for my wife, Lynann, and my family. Lynann's patient support permitted me the freedom to pursue a Ph.D. program, and the influence of my parents and family on my goals, values, and accomplishments cannot be overstated. I also acknowledge my grandmother, Delia Carrión Fischer, to whom this thesis is dedicated. Although she passed away before I completed my Ph.D., she was always one of my proudest supporters and instilled within me, and the rest of her family, a love for education and life.

This research was sponsored by the Office of Naval Research, Robert Bosch GmbH, and the MIT Sloan Fund. Financial support also came from the National Science Foundation Graduate Fellowship program.

Table of Contents

List of Figures

List of Tables

1. Introduction

1.1 Nanocrystalline Materials

1.1.1 Definition

Nanocrystalline is a term used to describe a crystalline material with a particle or grain size less than 100 nm. Conventional materials, both bulk (such as steel or concrete) and powdered (such as sand or table salt), typically have grain sizes on the orders of microns to millimeters. By reducing the grain or particle size to the nanometer regime, the specific surface area and grain boundary volume of these materials are greatly increased, which can have a large effect on the properties of the materials. Figure 1-1 shows the change in surface area and grain boundary volume fraction as the particle or grain size of a material is decreased. If the surface or grain boundary structure or chemistry is different from the bulk, then the nanocrystalline materials should exhibit behavior different from their microcrystalline form. The properties of the material can also change due to quantum confinement effects rather than interfacial effects. Electronic properties (as observed in quantum dots and wires), magnetic properties (exhibited through superparamagnetism or giant magnetoresistance), and optical properties (such as a shift in the absorption edge) can be dominated by quantum confinement effects. It is these differences between the bulk and nanocrystalline systems and the associated potential applications that have spawned numerous research programs on nanocrystalline materials around the world.

1.1.2 Properties

The creation of a surface or interface, such as cleaving a crystal, requires an increase in the energy of the system. The interfaces produced are locations of higher bond strains and relatively high disorder compared to the bulk crystal. In addition, interfaces can produce charge effects by adsorption of charged species onto the surface, or through the intrinsically produced ion concentration gradients in the near-interface region. These effects become more pronounced as the particle size and the radius of curvature are

decreased. Just as the vapor pressure of a liquid increases as the droplet size decreases, the interfacial energies of solids can change as the particle size is reduced. This can affect the catalytic activity of the materials or increase the diffusion rate along grain boundaries in nanocrystalline compacts. Of particular interest for ceramic applications are the increased driving force for densification and the potential improvement in densification rates due to increased grain boundary volume fraction as the particle and crystallite sizes are reduced to the nanometer regime.

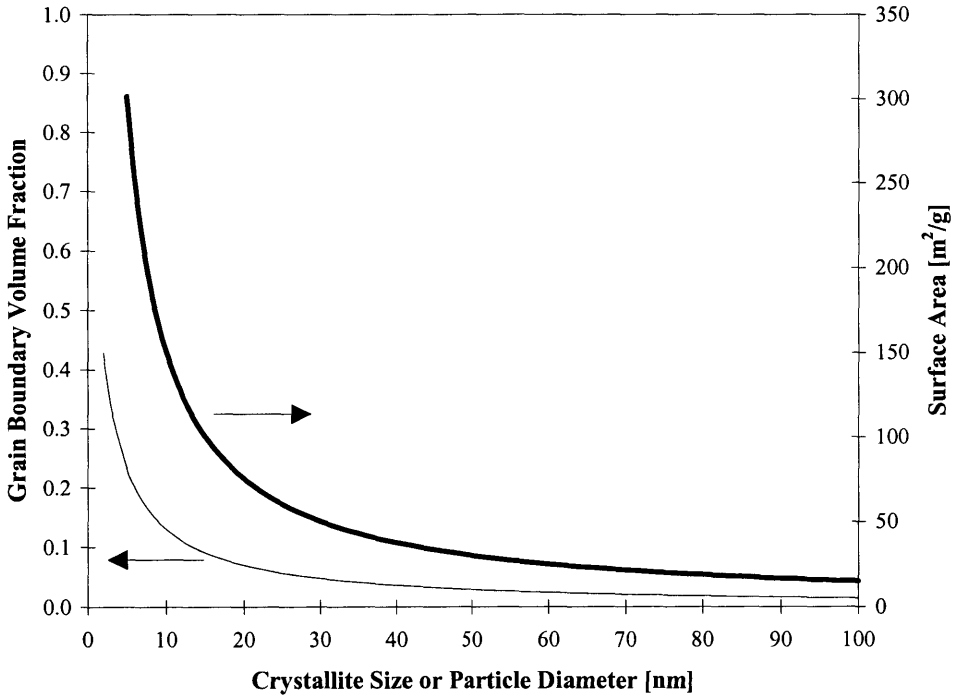

Figure 1-1. Grain boundary volume fraction and surface area as a function of crystallite size or particle size, respectively. Grain boundary volume fraction was calculated assuming a 5 Å-thick grain boundary; surface area was calculated for dense monodisperse spherical AlN particles.

1.1.3 Uses and Applications

Nanoparticles have been produced commercially for hundreds of years, and nature has been using nanocomposites for considerably longer. For example, carbon black has been produced since ancient times and is currently generated on the scale of millions of tons

per year for use in automobile tires and other products. Large quantities of silica and titania nanoparticles are also produced for abrasive and pigment applications. Biologically, nanocomposites such as bone (which is made of nanocrystalline carbonated apatite and collagen) are used where a light-weight, high elastic modulus, and high fracture toughness material is required. The highly complex nanostructures that have been constructed by nature for millions of years (e.g. seashells) are only now being simulated and replicated by human technology, albeit generally at a much simpler level.

Most of the current research on nanocrystalline materials is focused on high value-added, engineered systems whereby the material is designed at the nanometer scale to optimize specific properties for catalytic, electronic, optical, or magnetic applications. Also of interest is the generation of nanoparticles for production of bulk ceramic articles. The goal of such research is to understand, optimize, and reduce the costs of nanoparticle synthesis and processing to (i) produce materials that can be densified at lower temperatures and (ii) enhance the properties or lower the cost of specialized products. The improved densification of nanoparticulate compacts is due in part to the high surface areas of these materials, which result in a large driving force for sintering. The decrease in diffusion distances and the increased grain boundary volume in nanoparticulate systems also enhance the densification kinetics. These effects are illustrated through a generalized densification rate equation,

$$\frac{d\rho}{dt} = \frac{1}{G^N} \exp(-Q/RT) \qquad \text{(Equation 1-1)}$$

where the sintering rate ($d\rho/dt$) is inversely proportional to the grain size (G) to the third or fourth power (N), depending on whether surface or grain boundary diffusion dominates the sintering. Thus, by decreasing the particle size by a factor of 10, the sintering rate could increase by a factor of 1000 or more. This would have a direct impact on the cost of producing dense parts by reducing the temperature and/or time necessary to achieve full density. In addition, the milder sintering conditions might allow the nanocrystalline structure to be retained after densification, and the ultrafine grain size could lead to

improved mechanical properties such as hardness, strength, and wear resistance. However, the high costs of nanoparticle production, materials handling difficulties, and purity issues have thus far limited the widespread commercial application of nanocrystalline ceramics.

1.1.4 Nanoparticle Synthesis Methods

Ceramic nanoparticles are produced by many different methods that can be broadly categorized as wet-chemical synthesis, combustion synthesis, attrition, and gas-phase reaction techniques. Wet-chemical synthesis techniques encompass precipitation, hydrolysis-condensation reactions, salt reactions followed by calcination, etc. whereby the particle morphology is defined while in a liquid medium. Combustion synthesis techniques include flash pyrolysis of oxidizer/fuel mixtures, flame pyrolysis, and rapid evaporation techniques whereby the particles are formed very rapidly as the reactants undergo rapid heating. The attrition techniques, which have been used mostly for the preparation of nanocrystalline and amorphous metallic systems, utilize mechanical energy to obtain a nanocrystalline structure from typically microcrystalline starting materials. The gas-phase techniques, such as plasma reactions, evaporation-condensation reactions, and sputtering, usually rely on the homogeneous condensation of particles in the gas phase to produce the desired nanocrystals.

Each of these techniques has a number of advantages and disadvantages, and they are used in different applications depending on the composition, quantity, and purity that need to be produced. Since the mid 1980's, there have been significant research efforts devoted to these nanoparticle synthesis processes. The three synthesis techniques examined in this thesis were chemical precipitation, mechanical attrition, and gas-phase evaporation-condensation. Nanostructured alumina was obtained via precipitation and attrition, while nanocrystalline aluminum nitride particles were produced directly via a condensation-reaction process.

1.2 Alumina

1.2.1 Introduction

Alumina is one of the most widely used and studied ceramic materials. Over 30 million tons are produced each year, and although the majority of this is used for aluminum production, a considerable amount of alumina is utilized for abrasive, electronic, refractory, thermal management, optical, and catalytic applications. While the use of alumina in these various applications has involved a considerable amount of investigation and scientific understanding, much remains unknown about this material. In part, this is due to the wide variety of transitional aluminas and hydroxides that can be formed during the synthesis of alumina (see Section 1.2.2) and the fact that impurities, even at very low levels, can have significant effects on the electrical properties, phase stability, and diffusion rates. In fact, the general transformation mechanisms between the different transitional forms were not agreed upon until recently, and the translational pathways for the topotactical transformations of the transitional aluminas are still not well understood.

1.2.2 Metastable Forms and Phase Transformations

Alumina can exist in a surprisingly large number of structural configurations as shown in Figure 1-2. If you add to this list the five common hydroxides of alumina, then 14 forms of alumina are observed at atmospheric pressures. The technical report by Wefers and Misra [1] gives an excellent review of the hydrated and non-hydrated forms of alumina, and describes the structural differences among the forms as well as the methods to produce them. Generally, α-Al_2O_3 is considered the thermodynamically stable phase although recent studies have suggested that at a very fine particle size, γ-Al_2O_3 may be the lower energy crystal structure due to surface energy contributions [2,3]. As shown in Figure 1-2, the hydroxide phases from which the aluminas are derived can have a large effect on the crystal forms that evolve during thermal treatments. The only hydrated phase that does not produce transitional alumina phases during heating is diaspore ($Al_2O_3 \cdot H_2O$), which transforms directly to α-Al_2O_3 after dehydration at temperatures greater than 500°C.

Although diaspore would be very useful for making fine-grained, highly reactive α-Al_2O_3, it requires high temperatures and pressures to synthesize and is not found in sufficient quantities and purity to be commercially attractive for advanced applications [4].

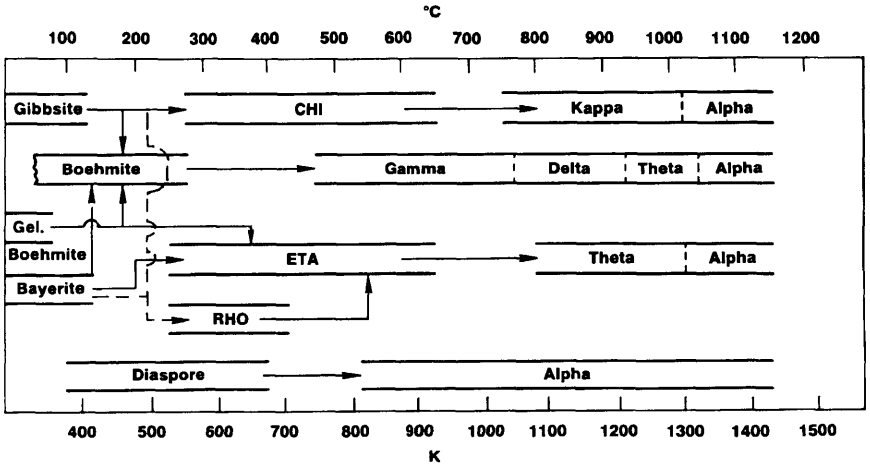

Figure 1-2. Schematic of alumina phase transformations with thermal treatments, from Wefers and Misra [1].

In general, the transitional phases are easily produced as ultrafine-grained materials with crystallite sizes in the nanometer range. Nanocrystalline alumina synthesis methods include precipitation and calcination, gas-phase synthesis, arc discharge, laser ablation, and thermal evaporation [5-8]. According to Herring's scaling law [9], these ultrafine crystals should result in a large reduction of the temperatures needed for sintering. Unfortunately, pressureless sintering of a nanocrystalline transitional alumina compact does not ensure that improved densification will occur. As the transitional phases are heated, relatively few α-Al_2O_3 nuclei (approximately 10^{10}-10^{11} nuclei/cm^3 [10,11]) are produced. These nucleated grains undergo rapid grain growth, consuming the transitional alumina matrix, resulting in a porous vermicular structure (Figure 1-3(b)). A contributing factor to this phenomenon is the large change in molar volume that occurs when the transitional aluminas transform to the α-Al_2O_3 phase. For instance, the transformation from θ-Al_2O_3 to α-Al_2O_3 involves shrinkage of 8% in molar volume. The combination of low nucleation density,

high growth rate through the fine-grained transitional alumina matrix, and the change in molar volume produces large porous α-Al_2O_3 grains. During the final stages of sintering, the pores are typically trapped within the grains (Figure 1-3(c)), making their removal extremely difficult. Therefore, the transitional aluminas are not directly used in the commercial production of dense ceramic parts. Instead, they are calcined to temperatures greater than 1100°C to obtain α-Al_2O_3, which is then milled to yield a reactive alumina powder for ceramic applications. This process of calcining the material at high temperatures, milling, forming and then sintering is inherently energy-intensive; significant savings could be achieved if the first two steps were eliminated or shortened.

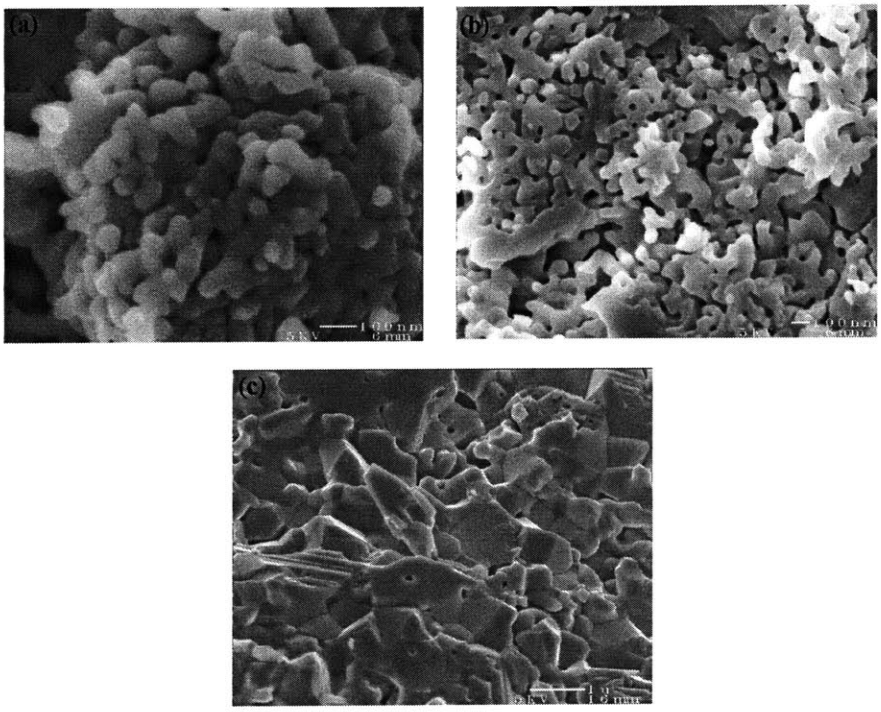

Figure 1-3. Fracture surfaces of γ-Al_2O_3 hot pressed for 30 minutes under 50 MPa at (a) 1100°C, (b) 1200°C, and (c) 1400°C.

1.2.3 Research Objectives

One of the goals of this thesis was to improve the transformation kinetics and densification of nanocrystalline transitional aluminas. The specific approach investigated

was the use of mechanical energy to transform a fraction of the transitional alumina to the α–phase. The nanocrystalline α-Al_2O_3 particles seeded within the transitional phases would help to lower the transformation temperature, improve the transformation kinetics, reduce the average grain size, and enhance the sinterability of the material. Additional background information, results on high-energy milling, and transformation kinetic studies are presented in Chapter 2. In Chapter 3, the sintering results and microstructural evolution are correlated to the mechanical seeding effects.

1.3 Aluminum Nitride

1.3.1 Introduction

The use of nanostructure processing to improve densification rates may be most beneficial for non-oxide ceramics. Metal nitrides and carbides typically have much lower diffusion rates than their oxide counterparts, making their densification more difficult. Nanostructure processing of aluminum nitride is of particular interest as pure AlN is difficult to sinter and this material is attractive for high value-added thermal management applications. AlN has a high thermal conductivity, low thermal expansion coefficient, high dielectric strength, and good mechanical properties compared to alumina, which is the material currently used in many electronic packaging applications. A comparison of AlN and other high thermal conductivity ceramics with silicon is shown in Table 1-1. The detriments of the alternative materials are significant: BeO can be toxic in powder form, SiC has relatively high dielectric losses, and bulk diamond is very expensive to produce. AlN has detriments as well -- most notably its oxygen affinity and its difficulty in metallization, which must be overcome for electronic substrate applications. The oxygen affinity is problematic because oxygen dissolved in the aluminum nitride reduces the thermal conductivity drastically through a relatively complex mechanism. At low levels, oxygen is dissolved in AlN by incorporation into nitrogen sites. To compensate for the charge imbalance, aluminum vacancies are created as follows:

$$Al_2O_3 \xrightarrow{AlN} 2Al_{Al} + 3O_N^{\bullet} + V_{Al}''' \qquad \text{(Equation 1-2)}$$

Due to electrostatic and size effects, these aluminum vacancies form extended defect structures known as inversion domain boundaries, which disrupt phonon transport within the grains. Through this mechanism, less than 1 wt% oxygen can reduce the thermal conductivity of AlN by over 30%. A substantial amount of work therefore has been directed towards understanding how the defect structures are formed [12-15], how to prevent initial oxygen incorporation, and how to minimize oxygen effects on thermal conductivity via materials processing.

Table 1-1. Materials properties of various high thermal conductivity ceramics in comparison to silicon. Data taken primarily from Prohaska and Muller [16]. (TCE is thermal coefficient of expansion.)

Properties		AlN	Al_2O_3	BeO	SiC	Diamond	Si
Physical							
Density (g/cm^3)		3.26	3.75	2.9	3.2	3.51	2.3
Young's Modulus (Mpsi)		48	49	47	57	1220	24
Vickers Hardness (kg/mm^2)		1200	2500	1200	2000	10,000	
Bending Strength (kg/mm^2)		40	35	25	45		
Electrical							
Volume Resistivity (Ω-cm)		$>10^{14}$	$>10^{14}$	$>10^{14}$	$>10^{14}$	$>10^{14}$	
Dielectric Constant (MHz)		8.5-8.7	9	6.7	40	5.7	
Dissipation Factor, x 10^{-4}, 1 MHz		<14	3	3	500		
Dielectric Strength (kV/mm)		15	15	12	.07	1000	
Thermal							
Thermal Conductivity (W/m/K)		160-250	25	260	270	2000	150
TCE (ppm /°C)	RT-100°C	2.65	7	6.5	3.7	1.1	2.3
	RT-400°C	4.8	7.4	8	3.7		

1.3.2 Conventional Processing

AlN can be synthesized in a number of different ways. The two most widely used commercial methods are carbothermal reduction and nitridation of aluminum oxide, and direct nitridation of aluminum metal. The carbothermal reduction-nitridation process starts with an intimate mixture of γ-Al_2O_3 (used for its small particle size and high surface area) and a finely divided carbon source. This mixture is heated under nitrogen to concomitantly reduce and nitride the alumina. Generally, an excess of carbon is used, which must be

removed after nitridation through controlled oxidation at ~600°C. The direct nitridation involves heating powdered aluminum in an atmosphere of ammonia or nitrogen to form AlN. In both of these diffusion-limited processes, the materials must typically be heated to temperatures in excess of 1600°C, ground, and reheated to assure complete reaction. The high temperatures can result in a relatively coarse material, which must be ground to obtain reactive AlN. Powder purity is a big issue with these processing methods, and very high purity products (>99%) are difficult to achieve, especially for high surface area materials. In addition to the residual oxygen that might remain from the γ-Al_2O_3 or on the surface of the aluminum, there is also the possibility of oxygen contamination from the carbon removal step and from surface hydrolysis during or after the milling operations.

After synthesis, the powder must be formed and sintered to obtain a useful article. Because of its highly reactive nature, AlN must be handled under dry conditions unless the surfaces are treated to prevent hydrolysis. Bowen *et al.* [17] showed that unprotected 1.2 μm-sized particles of AlN decomposed rapidly into AlOOH and ammonia when exposed to deionized water. After 2 hours and 8 hours of contact, the AlN contained over 6 wt% and 15 wt% oxygen, respectively; 80% conversion to aluminum hydroxide was observed after 24 hours of contact. Preventive measures, such as the formation of a relatively impermeable Al_2O_3 layer through controlled oxidation, or the application of a polymer coating, have been shown to reduce AlN hydrolysis considerably thereby allowing aqueous processing [18]. However, non-aqueous and dry powder processing approaches are still the dominant techniques for AlN forming operations.

Even after nearly ideal air-free processing, the oxygen contamination from powder synthesis is still generally sufficient to disrupt the thermal transport within AlN. The effect of low diffusivities causing poor sinterability also remains to be overcome. The solution, which has been found after considerable research, is to add a sintering additive such as Y_2O_3 or CaO, which promotes the formation of a liquid phase. The diffusion of material within the liquid phase is orders of magnitude higher than in the solid phase so that sintering is greatly enhanced. The proposed sintering model is that the Y_2O_3 forms a melt,

which initially wets the grain boundaries, promoting material transport and densification. However, as the Al_2O_3 content in the melt increases, the interfacial energy between the melt and the AlN grains increases. The increase in interfacial energy causes the secondary phase to retreat from the grain boundaries to the triple points. The dissolution of Al_2O_3 into the liquid phase effectively scavenges oxygen from the AlN grains, thereby increasing the thermal conductivity. The degree of oxygen removal is reportedly proportional to the heat of formation of the associated aluminate. Unfortunately, the heats of reaction for many of the possible aluminates at the sintering temperatures were not known, so many experiments with lanthanide oxides and basic oxides at various concentrations have been conducted to determine the optimal sintering additive or mixture of additives [19-21]. The model is complicated by recent reports that suggest that the oxygen does not diffuse out of the grains, but the grains themselves are dissolved and reprecipitated [22]. This argument is based in large part on the low oxygen/nitrogen interdiffusion values observed for polycrystalline AlN [23]. The authors calculated the observed O/N interdiffusion rate to be approximately 2 orders of magnitude too low for solid-state diffusion to effectively purify the AlN grains. However, another paper [24] reported values for the O/N interdiffusion that were 1-2 orders of magnitude higher, and suggested a strong relationship between oxygen conductivity in the grain boundary and the yttrium content in the grain boundary at high temperatures. Many more experiments will have to be conducted before the purification mechanism is fully understood. Nevertheless, AlN with 2-15 wt% Y_2O_3 additive can be pressureless sintered to full density and can attain a thermal conductivity as high as 200 W/m·K. It has also been shown that if the secondary phases are removed from the samples, either through extended heat treatments at high temperatures or other means, the thermal conductivity can approach 260 W/m·K.

1.3.3 Research Objectives

One of the goals of this thesis is to produce a high-purity nanocrystalline aluminum nitride powder that can be sintered without additives to full density. As described above, if additives are not used and if the oxygen content of the grains can be kept very low, then the

detrimental effects associated with the secondary phases and impurities on the thermal conductivity can be minimized. The first step in achieving this research objective is to produce high-purity nanocrystalline AlN powder. This was accomplished through the use of a novel forced-flow reactor built by Darren Castro [25] of our laboratory. Reactor modifications and process optimization, along with powder characterization, are described in Chapter 4. Processing, sintering, microstructure, and properties of AlN are discussed in Chapter 5.

1.4 References

[1] K. Wefers and C. Misra, "Oxides and Hydroxides of Aluminum," *Alcoa Technical Paper 19, Rev.* Alcoa Technical Center, 1987, p. 47.

[2] J. M. McHale, A. Auroux, A. J. Perrotta, and A. Navrotsky, "Surface Energies and Thermodynamic Phase Stability in Nanocrystalline Aluminas," *Science*, **277**, 788-91 (1997).

[3] J. M. McHale, A. Navrotsky, and A. J. Perrotta, "Effects of Increased Surface Area and Chemisorbed H_2O on the Relative Stability of Nanocrystalline γ-Al_2O_3 and α-Al_2O_3," *J. Phys. Chem. B,* **101** [4] 603-13 (1996).

[4] T. Tsuchida and K. Kodaira, "Hydrothermal Synthesis and Characterization of Diaspore, β-$Al_2O_3 \cdot H_2O$," *J. Mater. Sci.*, **25** [10] 4423-26 (1990).

[5] T. Hirayama, "High-Temperature Characteristics of Transition Al_2O_3 Powder with Ultrafine Spherical Particles," *J. Am. Ceram. Soc.*, **70** [6] C122-24 (1987).

[6] C. E. Warble, "Surface Structure of Spherical Gamma-Alumina," *J. Mater. Sci.*, **20**, 2512-16 (1985).

[7] E. Borsela, S. Botti, R. Giorgi, S. Martelli, S. Turtu, and G. Zappa, "Laser-Driven Synthesis of Nanocrystalline Alumina Powders from Gas-Phase Precursors," *Appl. Phys. Lett.*, **63** [10] 1345-47 (1993).

[8] G. P. Johnston, R. Muenchausen, D. M. Smith, W. Fahrenholtz, and S. Foltyn, "Reactive Laser Ablation Synthesis of Nanosize Alumina Powder," *J. Am. Ceram. Soc.*, **75** [12] 3293-98 (1992).

[9] C. Herring, "Effect of Change of Scale on Sintering Phenomena," *J. Appl. Phys.*, **21**, 301-03 (1950).

[10] W. A. Yarbrough and R. Roy, "Microstructural Evolution in Sintering of AlOOH Gels," *J. Mater. Res.*, **2** [4] 494-515 (1987).

[11] G. L. Messing and J. C. Huling, "Transformation, Microstructure Development and Sintering in Nucleated Alumina Gels"; pp. 669-79 in *Processing of Ceramics,* Proceedings of the 3rd European Ceramic Society Conference, Vol. 1. Edited by P. Duran and J.F. Fernandez. Faenze Editrice Iberica S.L., 1993.

[12] J. H. Harris, R. A. Youngman, and R. G. Teller, "On the Nature of the Oxygen-Related Defect in Aluminum Nitride," *J. Mater. Res.,* **5** [8] 1763-73 (1990).

[13] A. Westwood, R. Youngman, M. McCartney, A. Cormack, and M. Notis, "Oxygen Incorporation in Aluminum Nitride via Extended Defects: Part I. Refinement of the Structural Model for the Planar Inversion Domain Boundary," *J. Mater. Res.,* **10** [5] 1270-86 (1995).

[14] A. Westwood, R. Youngman, M. McCartney, A. Cormack, and M. Notis, "Oxygen Incorporation in Aluminum Nitride via Extended Defects: Part II. Structure of Curved Inversion Domain Boundaries and Defect Formation," *J. Mater. Res.,* **10** [5] 1287-1300 (1995).

[15] A. Berger, "Nucleation and Growth of Inversion Domains in AlN: Part I, Study of Fundamental Processes," *J. Am. Ceram. Soc.*, **78** [1] 153-60 (1995).

[16] G. W. Prohaska and G. R. Miller, "Aluminum Nitride: A Review of the Knowledge Base for Physical Property Development," *Mater. Res. Soc. Symp. Proc.,* **167**, 215-27 (1990).

[17] P. Bowen, J. G. Highfield, A. Mocellin, and T. A. Ring, "Degradation of Aluminum Nitride Powder in an Aqueous Environment," *J. Am. Ceram. Soc.,* **73** [3] 724-28 (1990).

[18] E. G. Groat and T. J. Mroz, "Aqueous Slip Casting of Stabilized AlN Powders," *Bull. Am. Ceram. Soc.*, **73** [11] 75-78 (1994).

[19] K. Watari, A. Tsuzuki, and Y. Torii, "Effect of Rare-Earth Oxide Addition on the Thermal Conductivity of Sintered Aluminum Nitride," *J. Mater. Sci. Lett.*, **11**, 1508-10 (1992).

[20] T. B. Troczynski and P. S. Nicholson, "Effect of Additives on the Pressureless Sintering of Aluminum Nitride between 1500° and 1800°C," *J. Am. Ceram. Soc.*, **72** [8] 1488-91 (1989).

[21] P. S. de Baranda, A. K. Knudsen, and E. Ruh, "Effect of Yttria on the Thermal Conductivity of Aluminum Nitride," *J. Am. Ceram. Soc.*, **77** [7] 1846-50 (1994).

[22] A. V. Virkar, T. B. Jackson, and R. A. Cutler, "Thermodynamic and Kinetic Effects of Oxygen Removal on the Thermal Conductivity of Aluminum Nitride," *J. Am. Ceram. Soc.*, **72** [11] 2031-42 (1989).

[23] M. Sternitzke and G. Müller, "EELS Study of Oxygen Diffusion in Aluminum Nitride," *J. Am. Ceram. Soc.,* **77** [3] 737-42 (1994).

[24] H. Solmon, D. Robinson, and R. Dieckmann, "Oxygen Transport in Aluminum Nitride Substrates," *J. Am. Ceram. Soc.,* **77** [11] 2841-48 (1994).

[25] D. T. Castro, *Synthesis, Processing, and Properties of Nanocrystalline Nitrides*, Sc.D. Thesis. Massachusetts Institute of Technology, Cambridge, MA, 1997.

2. Transformation Kinetics of Mechanically Seeded Alumina

2.1 Introduction

This chapter describes the effects of high-energy ball milling (HEBM) on the γ-to-α phase transformation kinetics of Al_2O_3. The background section (2.1.1) describes several methods previously used to affect the transformation kinetics and some of their limitations. In the experimental section (2.2), the equipment and methods of sample preparation are described, and the efficacies of the HEBM process and other methods reported in the literature are compared based upon experimentally determined phase transformation activation energies. Finally, a phase transformation model for finite particle systems is derived and used to evaluate the validity of applying the Johnson-Mehl-Avrami-Kolmogorov (JMAK) model to a seeded alumina system.

2.1.1 Background

The difficulties associated with densifying the nanocrystalline transitional aluminas are well documented, and several different approaches to solving this problem have been reported. As described in Chapter 1, the fundamental problem in transitional alumina densification lies in the low nucleation density of the α-Al_2O_3 phase [1, 2]. This problem is further aggravated by the change in molar volume of approximately 8% associated with the θ-to-α transformation. In addition, the grain growth rate during the transformation is significantly higher than the sintering rate, so pores become surrounded by the newly transformed "vermicular" α-Al_2O_3 grains. Upon further densification, the pores become trapped within the grains, and the pathway for their removal becomes bulk diffusion rather than grain boundary diffusion. Since bulk diffusion is 1-2 orders of magnitude slower than grain boundary diffusion, the pores remain trapped within the grains. These intragranular pores effectively prevent theoretical density from being achieved unless very high temperatures and long sintering times are used. The successful approaches to tackling these densification problems typically involve enhancing the nucleation rate, decreasing the grain growth rate, improving the sintering kinetics, or a combination thereof. By increasing the

nucleation density, the average grain size of the transformed particles can be reduced and the sintering kinetics (as described by Equation 1-1) are increased. These effects can result in significant improvements in the sintering behavior of alumina.

2.1.1.1 Isostructural Seeding

One simple way to enhance the nucleation rate is to add seed particles that have the same structure as the desired phase. The seed particles provide locations with a lower surface energy barrier for transformation, which results in easier nucleation. The reduction in the nucleation barrier depends on the structural similarity between the new phase and the seed particle. The nucleation density, and therefore the resulting crystallite size, will be determined by the heterogeneous interfacial area, which is determined by the particle size and number of seeds that are added.

Many different materials have been added to the transitional alumina phases, both as solid particles and in solution, to determine their effect on the transformation rate. For instance, Xue and Chen [3] investigated the effect of a wide variety of additives on the γ-to-α phase transformation. They found that B_2O_3, SiO_2, and ZrO_2 additions retarded the transformation while additives that promoted a liquid phase, such as ZnF_2, CuO, V_2O_5, and Li_2O, increased the transformation kinetics, probably by increasing the growth rate during transformation. Sintering studies using alumina seeded with these materials were not performed.

As discussed previously, however, one would expect that those materials that are isostructural with α-Al_2O_3 would reduce the transformation barrier most significantly. For example, Fe_2O_3 and Cr_2O_3 additions have been investigated and were found to have a large effect on the transformation kinetics [4, 5]. Boehmite (AlOOH) gels seeded with α-Fe_2O_3 showed an increase in the transformation kinetics that corresponded to a 17% decrease in the transformation activation energy. The increased nucleation density resulted in a finer microstructure, and improved the densification kinetics considerably. Instead of creating the characteristic vermicular microstructure, the seeding resulted in the formation of small, dense α-Al_2O_3 grains. After pressureless sintering at 1300°C for 2 hours, the Fe_2O_3-seeded

compacts (with 10^{14} seeds/cm^3) were fully dense, while unseeded compacts had achieved only 80% of theoretical density.

Although these results are interesting, the presence of impurities, even at low concentrations, is generally not desirable. This is especially true for electronic and optical applications where the alumina purity must be 99.9% or higher, and transition metal impurities should be kept in the ppm range.

2.1.1.2 α-Al_2O_3 Seeding

The obvious solution to the problem of impurities is to use α-Al_2O_3 particles to seed the γ-to-α phase transformation. In this way, the purity may be retained while improving the transformation kinetics at the same time. This method has been studied extensively by Professor Gary Messing's group at Pennsylvania State University [6-12] and other researchers [1, 13-15]. Their approach has been to grind α-Al_2O_3 to produce submicron particles, which were then classified and harvested via sedimentation. The seed particles were then dispersed in a boehmite sol to obtain intimate contact between the seeds and the boehmite particles. After gelling and drying, the material was lightly ground and densified by hot pressing, sinter forging, or pressureless sintering. Seeding and processing the boehmite sols in this manner produced powders that could be densified at very low sintering temperatures and, when sinter-forged, could generate fully dense material with 230 nm-sized grains [12]. This method and variations of this process have been patented, primarily for the synthesis of abrasive grains rather than bulk articles [16-18].

2.1.1.3 High-Energy Approaches

The approaches described above rely on the external addition of seed particles or the introduction of a liquid phase to enhance the transformation kinetics. It is also possible to increase the density of nuclei through mechanical operations on the powder or compact. There are two arguments that have been invoked to describe the effects of pressure and mechanical energy on the nucleation process. The first argument is based upon the fact that nucleation will most likely occur in locations where the local packing of the aluminum and

oxygen atoms is similar to α-Al_2O_3, or where defects reduce the energy requirement for nucleation. This desired atomic packing and/or defect presence will most likely occur at the interface between two particles. This argument was used by Pach *et al.* [19] to describe the influence of particle packing (which was changed in boehmite gels via cold isostatic pressing) on the transformation kinetics. They stated that "there is a higher number of potential nucleation sites ... at a higher average coordination number of alumina particles" [19]. At higher pressures, a denser packing was obtained, increasing the number and area of particle-particle contacts, thereby enhancing the kinetics of nucleation and growth. A similar argument was used to explain differences observed in α-Al_2O_3 nucleation in boehmite gels that had been prepared differently, but had not been subjected to significant external pressures [20]. In this case, both the microstructure and the atomic arrangement of the gels were different due to the different methods of preparation, so it was difficult to determine which dominated the nucleation kinetics.

The second argument used to explain the effect of pressure on the nucleation kinetics is that the applied pressure directly creates α-Al_2O_3 nuclei. This argument is based upon the observed effect of pressure on the transformation of transitional alumina to α-Al_2O_3 [21]. In their study, Ishitobi *et al.* showed that η-Al_2O_3 could be transformed directly into α-Al_2O_3 in less than 5 minutes at temperatures as low as 600°C under an applied pressure of 1.5 GPa. While this combination of pressures and temperatures is not easily achieved with conventional compaction techniques, high-energy processes such as dynamic shock compaction, explosive compaction [22], and high-energy milling [23-30] have been shown to produce sufficient increases in localized temperature and pressure to generate α-Al_2O_3 directly from the transitional phases.

Depending on the amount and type of energy introduced into the system and the speed at which it is applied, one or more of the above mechanisms may be affecting the nucleation density. During these high-energy processes, a significant amount of particle rearrangement can occur, and superplastic deformation of the nanometer-sized grains has also been reported. In addition, some of the alumina can be amorphized during these high-

energy processes, which may enhance not only the nucleation rate but also the subsequent growth rate.

Theoretically, the relative effects of pressure on the phase transformation and the particle rearrangement to reduce the nucleation barrier could be experimentally determined. However, the complexity of the system makes this a daunting task. In addition to the effects discussed earlier, it has been reported that the presence of water [31], impurities [1-3], degree of crystallinity [32], crystallite size, previous thermal history, surface area [33, 34], and even the presence of large electric fields [35] can influence the phase transformation kinetics of alumina. Given the variety of synthesis routes and chemical precursors for alumina, it is not surprising that researchers have come to different conclusions concerning the relative importance and the effects of these parameters on the phase transformations of alumina.

2.2 Experimental

The starting γ-Al_2O_3 for these experiments was obtained by calcining boehmite (AlOOH) at temperatures between 550°C and 700°C for 4 hours in air. This was found to give a high surface area γ-Al_2O_3 with a crystallite size of ~8 nm. The boehmite precursor used for most of these experiments was Catapal® B, generously donated by Vista Chemical Company (Houston, Texas). Additional boehmite samples, primarily those containing MgO as a dopant, were synthesized in the laboratory. These samples were prepared by adding 250 ml of a 0.4 M $Al(NO_3)_3$ (99.9%, Fluka Chemical Company) ethanolic solution dropwise to a stirred solution of 200 ml ethanol, 200 ml of water and 100 ml of ammonium hydroxide (30%). The resulting solution was aged overnight and washed with ethanol via centrifugation. There were no detectable differences in the transformation kinetics of the differently prepared γ-Al_2O_3 samples.

High-energy ball milling was conducted in a SPEX 8000 Mixer/Mill (SPEX CertiPrep, Metuchen, New Jersey) with a ball-to-powder weight ratio of 5:1. The milling vials and balls used were either WC/Co (3 balls, total ball weight ~ 30 g) or ZrO_2 (2 balls,

total ball weight ~ 12 g). All milling was performed on dry γ-Al_2O_3 powder without any additives.

Surface area and pore size distribution of the powders were determined by nitrogen adsorption using a Micromeritics ASAP 2000 analyzer. Since the phase transformation is exothermic, the transformation temperature was investigated using a Perkin Elmer System 7 Differential Thermal Analyzer. Differential thermal analysis (DTA) was performed at a heating rate of 10°C/min under flowing nitrogen using platinum sample cups.

X-ray diffraction (XRD) was performed for phase identification and quantitative analysis with a Siemens D5000 θ-θ diffractometer (40 kV and 40 mA) using Cu-K_α radiation and a nickel filter. The internal standards used for quantitative analysis were either elemental silicon (Si) or fluorite (CaF_2). Prior to analysis, the internal standard was added to the sample so that a standard-to-sample weight ratio of 1:4 was used. Mixing was performed by hand in an agate mortar and pestle. The ratio of the peak areas of the internal standard and α-Al_2O_3 was then compared to a previously prepared calibration curve to obtain the fraction of α-Al_2O_3 present in the sample. The peaks analyzed depended on the internal standard. With CaF_2 as the standard, the (012) peak of α-Al_2O_3 and the (111) peak of CaF_2 were measured; with Si as the standard, the (110) peak of α-Al_2O_3 and the (311) peak of Si were used. The average α-Al_2O_3 content from two measurements was used in each case; the sample was removed from the XRD slide after the first analysis, mixed, and then reloaded for the second analysis.

2.3 Effects of High-Energy Ball Milling

2.3.1 Effect of Milling Time

The first step in this research was to reproduce previous researchers' claims that nanocrystalline α-Al_2O_3 could be produced through high-energy milling of the transitional phases. An initial powder charge of 6 g of γ-Al_2O_3 in the WC/Co ball-and-vial set was subjected to 12 hours of milling in the SPEX 8000 Mixer/Mill. A small amount of powder,

approximately 0.25 g, was removed after every 2 hours of milling for phase determination by XRD. The diffraction patterns obtained from this experiment are shown in Figure 2-1. As the powder was milled, it converted from γ-Al_2O_3 to nanocrystalline α-Al_2O_3 as shown by the increasing intensity of the α-Al_2O_3 peak and the gradual disappearance of the broad nanocrystalline γ-Al_2O_3 peak. The final α-Al_2O_3 crystallite size after 12 hours of milling was determined by Kochendörfer's method [36] to be 22 nm with a residual strain of 0.48%. The time necessary to achieve complete conversion was on the order of 12 hours. During this extended milling, a considerable amount of WC was incorporated, which was unacceptable if a high-purity alumina was desired. Interestingly, a small amount of α-Al_2O_3 was observed after only two hours of milling. A simple calculation showed that only $6x10^{-4}$ wt% of 22-nm, spherical α-Al_2O_3 seeds were required to obtain 10^{12} seeds/cm^3. This calculation gave only an approximate value, since the milling operation does not necessarily produce evenly distributed nuclei. However, it suggested that the γ-Al_2O_3 would not have to be milled for 12 hours to significantly impact the nucleation density.

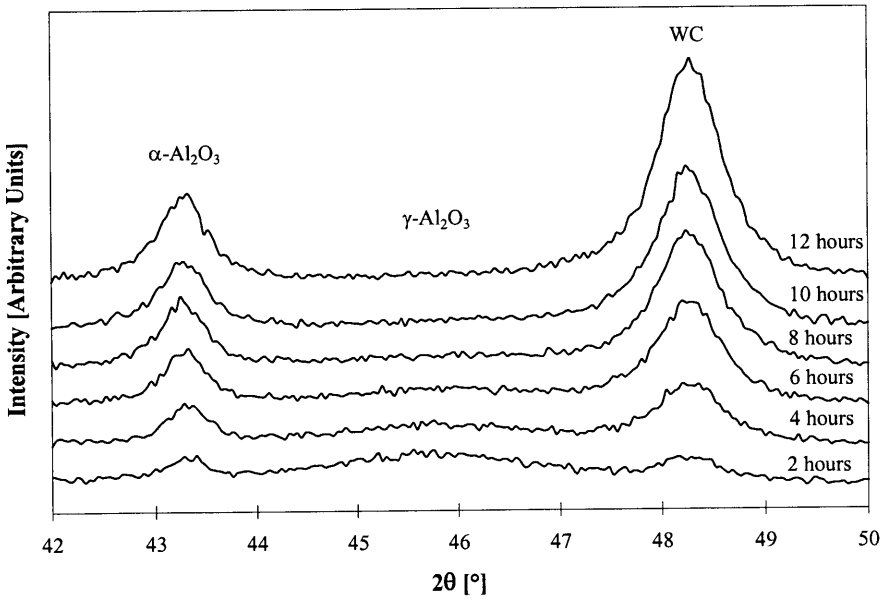

Figure 2-1. X-ray diffraction patterns of γ-Al_2O_3 powder after milling for different periods with a WC/Co ball-and-vial set.

2.3.2 Effects on Phase Transformation Temperature

The next step, therefore, was to determine how HEBM affects the transformation kinetics. A simple way to measure this is to examine the γ-to-α transformation temperature as a function of milling time. The γ-to-α transformation is exothermic with a ΔH of approximately -20 kJ/mol [37], so the temperature at which the transformation occurs can be observed through DTA studies. Plots of the transformation temperature as a function of milling time for samples that had been milled with either WC/Co or ZrO_2 ball-and-vial sets are shown in Figure 2-2. 2 hours of milling reduced the transformation temperature from 1220° to approximately 970°C, which was even lower than that obtained with external α-Al_2O_3 seed additions (1050°C) [7].

Milling periods longer than 2 hours did not appreciably decrease the transformation temperature further. This suggested that the transformation process changed from nucleation-limited to growth-limited kinetics, and the activation energy required for transformation was significantly reduced through seeding. Although the transformation from γ-Al_2O_3 to α-Al_2O_3 does not require long-range atomic motion, it is still not a diffusionless operation and will be strongly temperature-dependent. Thus, although additional seeds were created at longer milling times, the transformation temperature was not reduced further because of diffusional limitations to the growth of the new phase.

The changes in transformation temperature with milling time were strikingly similar for γ-Al_2O_3 samples milled in WC/Co and ZrO_2 ball-and-vial sets. One would usually expect that the ball-and-vial set made of the higher density material would have a greater, more rapid effect on the phase transformation, as widely accepted in mechanical metallurgy and attrition milling literature [38]. However, in this instance, the influence of milling media appeared to be minor even though they differed in density by ~ 2.5 times (densities were 5.86 g/cm^3 for ZrO_2 and 15 g/cm^3 for WC/Co). A plausible explanation for this observation was that the important milling effects in this case occurred in the first few minutes of milling. Therefore, the initial transformation rates (for < 10% conversion),

rather than the time periods to achieve complete reaction, were being measured here; the former might be less sensitive to the milling media density.

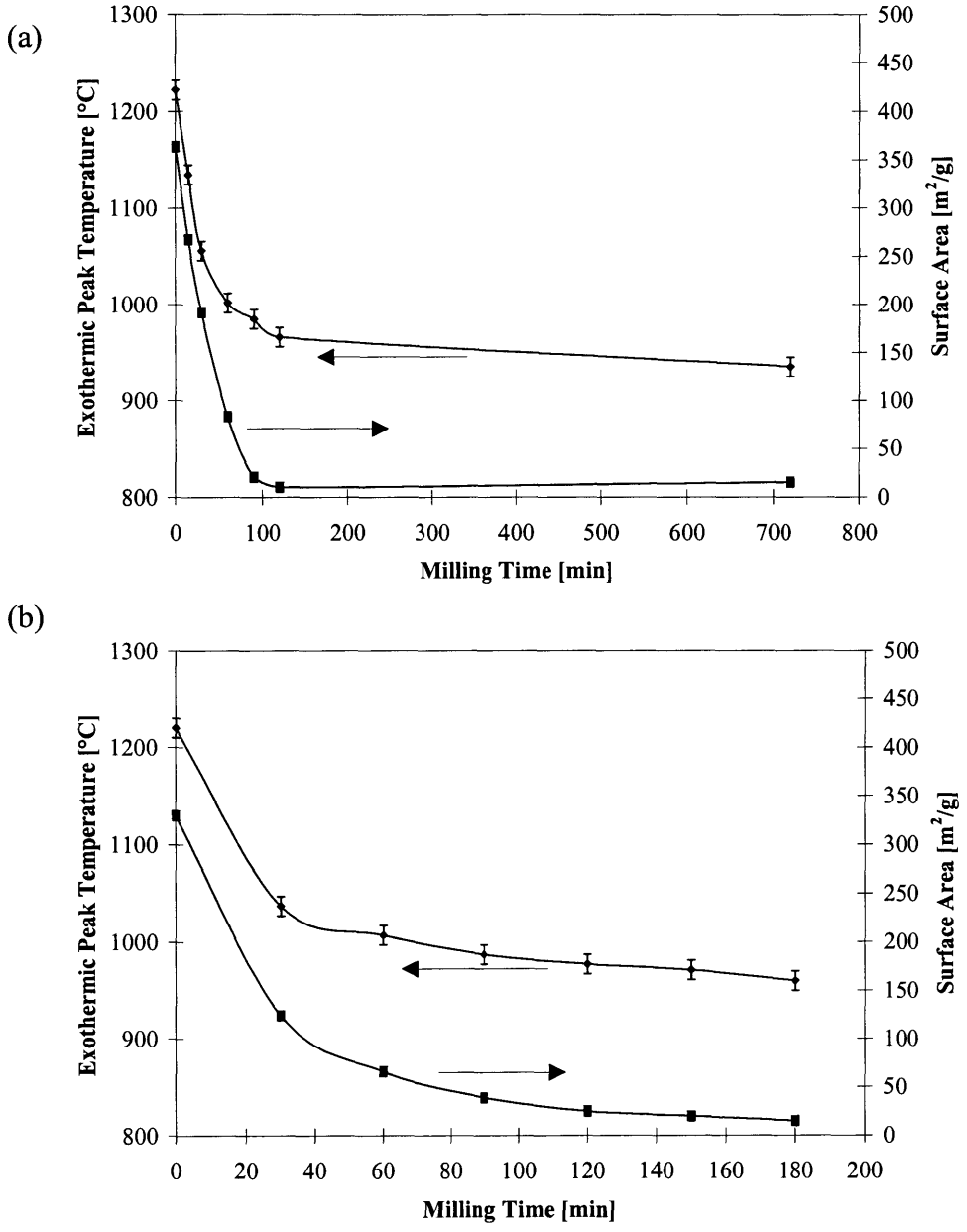

Figure 2-2. Transformation exothermic peak temperature and B.E.T. surface area as a function of milling time for γ-Al_2O_3 milled with (a) WC/Co and (b) ZrO_2 ball-and-vial sets.

The large change in surface area with milling time was also shown by Figure 2-2 to be relatively independent of the milling media. The loss of surface area with milling was due primarily to pore closure (pore volume decreased from 0.95 cm^3/g to 0.04 cm^3/g after 2 hours of milling with a WC/Co ball-and-vial set); however, powder agglomeration and impurity introduction (due to wear of the milling media) probably had an effect at longer milling times.

2.3.3 Transformation under Isothermal Heat Treatments

Another way to study the influence of mechanical seeding is to measure the transformation rate of the milled powder under heat treatments at isothermal conditions. The experiments were performed on a small amount of powder (0.3-0.4 g) in a small quartz crucible in a preheated box furnace. A small thermocouple was kept within 3 cm of the crucible to measure the temperature, and assure that the box furnace was kept under isothermal conditions. Samples were removed after the specified time and rapidly cooled to <600°C within seconds. The powders were then mixed with the internal standards and characterized by quantitative X-ray diffraction analysis as described in Section 2.2.

The results obtained from experimental runs at 900°C and 950°C are shown in Figure 2-3. These plots of mass fraction of α-Al_2O_3 present as a function of log(time) displayed the S shape characteristic of nucleation and growth transformations. In contrast, an unmilled γ-Al_2O_3 sample would gradually transform to δ-Al_2O_3 instead of α-Al_2O_3 at these temperatures.

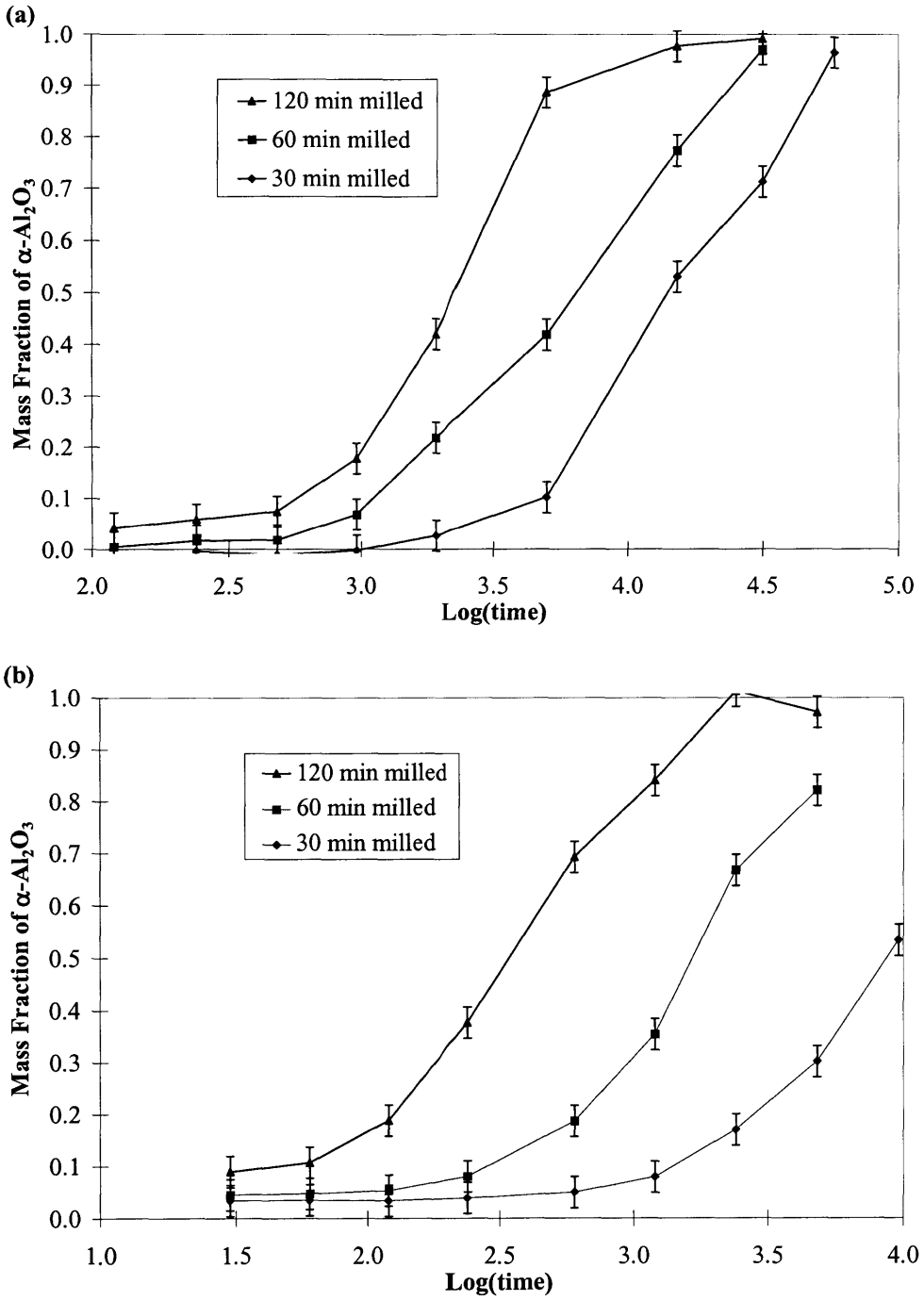

Figure 2-3. Mass fraction of α-Al_2O_3 present in the γ-Al_2O_3 samples after they had been milled in a WC/Co ball-and-vial set and heat treated for various time periods (in seconds) at (a) 900°C and (b) 950°C.

2.3.4 Application of JMAK Model

The data obtained from the transformation studies under isothermal heat treatments can be used to determine the transformation kinetics by applying the Johnson-Mehl-Avrami-Kolmogorov (JMAK) model. The JMAK equation for a model system with homogeneous nucleation and growth is

$$X = 1 - \exp\left(-\frac{\pi G^3 I t^4}{3}\right) \qquad \text{(Equation 2-1)}$$

where X is the fraction transformed in time t as a function of the growth rate G and nucleation rate I. For a system with preexisting nuclei (seeds) with a nuclei density of I', the JMAK model becomes

$$X = 1 - \exp\left(-\frac{4\pi G^3 I' t^3}{3}\right) \qquad \text{(Equation 2-2)}$$

Various special cases of these basic equations have been derived using the concept of extended volume fraction (for wires, thin films, grain boundary nucleation, surface nucleation, etc.) [39-43]. From these expressions, the transformation of an idealized material may be obtained if the geometry, growth rate, and nucleation rate (or seed density) are known. However, in most cases, these quantities are unknown and the reverse operation is desired, namely the determination of the transformation kinetics from a set of transformation data. This may be obtained by simplifying Equations 2-1 and 2-2 to the following generalized JMAK expression:

$$X = 1 - \exp\left(-(kt)^n\right) \qquad \text{(Equation 2-3)}$$

This relationship combines the nucleation and growth kinetics into a single reaction rate, k. The equation can be transformed so that the data can be easily fitted using linear least-squares regression,

$$Log\left(Ln\left(\frac{1}{1-X}\right)\right) = n \cdot Log(k) + n \cdot Log(t) \qquad \text{(Equation 2-4)}$$

A plot of Log(-Ln(1-X)) vs. Log(t) should result in a line with a slope of n and a y-intercept of n·Log(k), which allows the so-called Avrami exponent n and the reaction kinetic constant

k to be determined. If the reaction rate is assumed to follow an Arrhenius dependence, then an effective activation energy can be determined by plotting Ln(k) vs. $1/T$ for data collected isothermally at different heat treatment temperatures T.

Although the JMAK model is often used to determine activation energies and even the geometry of a transformation (based upon the observed value of n), this must be done with considerable caution and additional supporting data. As mentioned previously, the activation energy determined through this model is actually an *effective* activation energy averaged over the entire transformation. The rate constant k of the reaction is a function of both the nucleation and growth kinetics so that the observed activation energy incorporates both of these items. In addition, the rate-limiting step of the transformation may change (i.e. from nucleation- to growth-limited) during the transformation so that the reaction rate obtained is actually a time-weighted average of the kinetics of the rate-limiting step. Finally, the model is based upon a large (infinite) volume of material transforming so that finite size effects are neglected. This is not important for conventional materials with a small surface-to-volume ratio; however, the finite size effects can become very important as the particle size is reduced to the submicron or nanometer regime.

Plots of the data obtained at 900°C and 950°C are shown in Figure 2-4 along with the linear fit to the JMAK expression. The error bars shown were 0.1 unit for the y-axis, which was approximately three times the estimated ±3-5% uncertainty in the XRD determination of α-Al_2O_3 mass fraction [44]. The error in the transformed data, however, was actually a very strong function of the mass fraction of α-Al_2O_3 present as shown in Figure 2-5. This plot was obtained by differentiating the left side of Equation 2-4 by the mass fraction X, multiplying the result by 3% or 5% of the mass fraction, and plotting the resulting value as a function of mass fraction of α-Al_2O_3. It showed that for a mass fraction of α-Al_2O_3 above 0.95, the error in the transformed data became extraordinarily large and should not be relied upon in determining the fitted line. The average value for the Avrami exponent n for these transformations was found to be 1.07. However, no physical

interpretation was assigned to this value since the system did not fit the homogeneous and semi-infinite criteria as discussed previously.

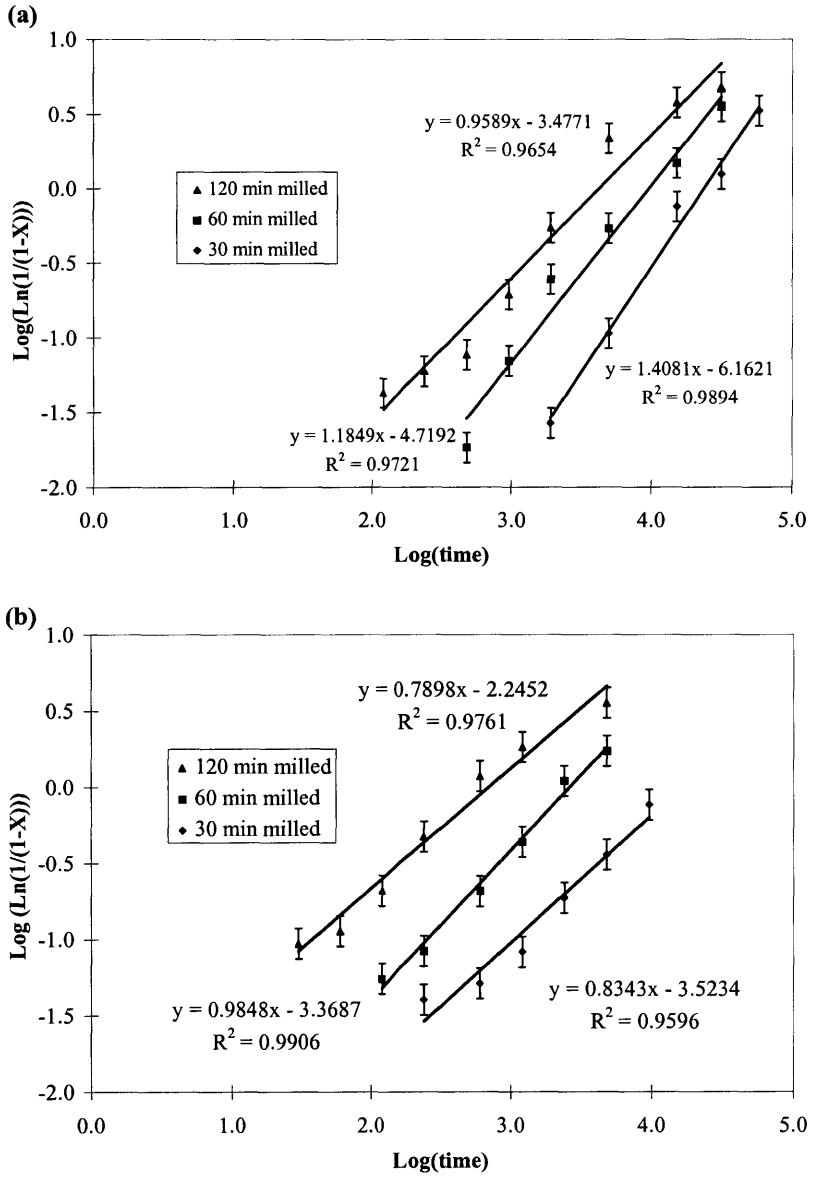

Figure 2-4. Linearized plots of the transformation data of Figure 2-3 obtained from isothermal heat treatments at (a) 900°C and (b) 950°C, showing a reasonable fit with the JMAK generalized transformation model (Equation 2-4). The γ-Al_2O_3 samples studied were milled in a WC/Co ball-and-vial set and heat treated isothermally for various time periods (in seconds).

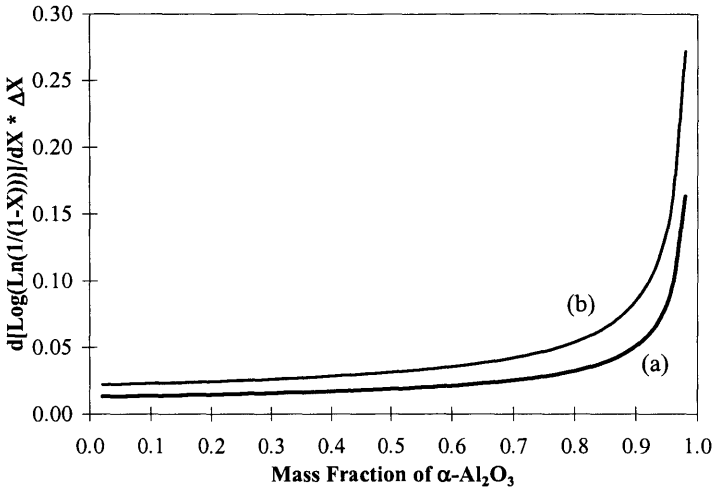

Figure 2-5. Error analysis for the linearized transformation data shown in Figure 2-4, assuming an uncertainty of (a) 3% and (b) 5% in the mass fraction of α-Al_2O_3 determined through quantitative XRD analysis.

By assuming an Arrhenius dependence of the reaction rate with temperature, the effective activation energy E_a may be determined. The slope of a line through the data plotted as -Ln(k) vs. $1/T$ will give E_a/R, where R is the universal gas constant. The kinetic data obtained for γ-Al_2O_3 powders milled for 30, 60, and 120 minutes with WC/Co ball-and-vial set is shown in Figure 2-6. The slopes of the lines, although slightly different, were found to be statistically comparable, giving an effective activation energy of 333 ± 22 kJ/mol. These results agree well with those obtained by Shelleman *et al.* [8], who reported an activation energy of 352 kJ/mol for γ-Al_2O_3 that had been externally seeded with α-Al_2O_3 particles at a concentration of 2.6 x 10^{13} seeds/cm^3. A comparison of the activation energies for different systems is shown in Table 2-1. The only system with an activation energy reportedly lower than that obtained via HEBM was an α-Al_2O_3-seeded system that also contained 10 wt% V_2O_5. At temperatures approximately 200°C above the melting point of V_2O_5 (650°C), the activation energy of this system decreased from 402 to 117 kJ/mol. The large decrease in activation energy when a liquid phase was present supported the hypothesis that once sufficiently seeded, the limiting step in the transformation is growth rather than nucleation.

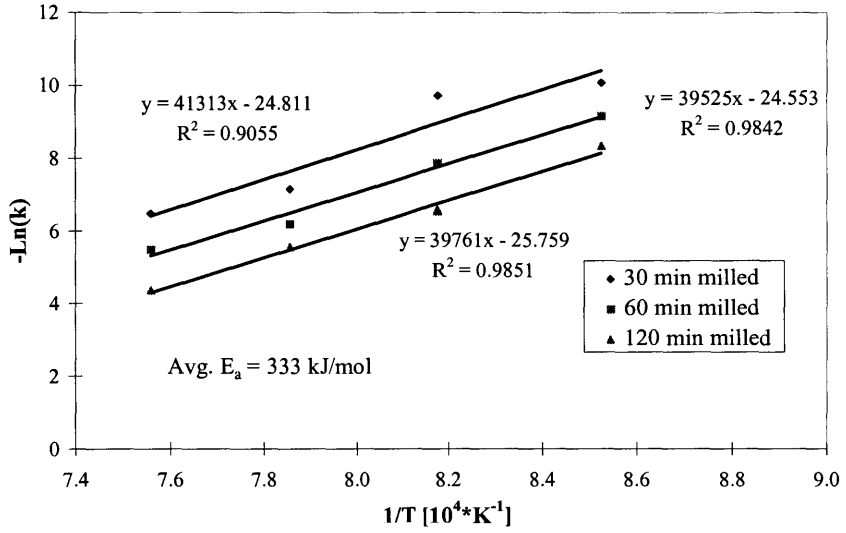

Figure 2-6. Arrhenius plots of the kinetic results obtained through JMAK fitting of the isothermal transformation data for γ-Al_2O_3 samples milled in a WC/Co ball-and-vial set.

Table 2-1. Activation energies associated with the γ-to-α phase transformation for various systems.

System	Determination Method	E_a (kJ/mol)	Reference
Unseeded γ-Al_2O_3 powder	Non-Isothermal DTA	600	[37]
γ-Al_2O_3 from boehmite compact	Isothermal JMAK	578	[5]
Boehmite with 10^{14} α-Fe_2O_3 seeds/cm^3	Isothermal JMAK	476	[5]
Unseeded γ-Al_2O_3	Isothermal JMAK	442	[9]
γ-Al_2O_3 with 1.8 x 10^{11} α-Al_2O_3 seeds/cm^3	Isothermal JMAK	439	[9]
γ-Al_2O_3 with 2.7 x 10^{13} α-Al_2O_3 seeds/cm^3	Isothermal JMAK	352	[9]
Mechanically seeded (HEBM) γ-Al_2O_3	Isothermal JMAK	333	This work
γ-Al_2O_3 with 2.7 x 10^{13} α-Al_2O_3 seeds/cm^3 and 10 wt% V_2O_5	Isothermal JMAK	402 at T < 850°C 117 at T > 850°C	[9]

2.4 Modeling of Phase Transformations in Finite Particles

The limitations of the JMAK model were a consequence of the assumptions made in the derivation of the model. The primary limitation of concern for the transformations of fine powders involved the assumption of a semi-infinite medium. Therefore, a finite particle model was created to determine the effect of particle size on the transformation kinetics. Its derivation was based on the time cone method developed by J. W. Cahn [45], which is outlined below for an idealized system of dense, finite, and spherical particles. Other publications that were useful in deriving and evaluating this model included reference [46] by Orihara and Ishibashi and computer simulations [47] by Levine *et al.*

2.4.1 Derivation of Spherical Finite Particle Model

The time cone method of J. W. Cahn [39] utilizes the fact that it is mathematically easier to determine the probability P that a point has not transformed than if it has transformed. The probability that a point q has not transformed at time t is the same as the probability that a nucleation event has not occurred anywhere in the surrounding volume that could have transformed the point of interest by time t. Figure 2-7 shows a 2-dimensional diagram of the model with point q as the location of interest. If a nucleation event had occurred within volume M during some previous time, then the point q would have transformed. As we get closer to time t, the nucleation event would have had to occur in a smaller volume L in order to transform point q. This change in volume can be seen in Figure 2-8, which is an exploded view of the particle cross-section and the nucleation volume boundary with time. The resulting picture is a cone expanding backwards in time, truncated by the particle boundary. The probability that point q would not have transformed is therefore a function of the nucleation probability and the volume of the cone, which is a function of the growth rate and time. Finite size effects can be imposed upon this model by changing the shape of the cone to account for the finite dimensions of the specimen. In Figure 2-8, the particle radius is R, the growth rate is G, and the point of interest is q, which is offset from the center of the sphere by a distance s. At times infinitely long ago, nucleation anywhere within the particle would have transformed the point of interest by

time t -- this is region C in the figure. During some intermediate time span (region B), the cone was bounded in only one area by the finite size of the particle, the other constraint was the growth rate of the transformed volume. At a more recent point in time (region A), the cone was entirely determined by the growth rate and was not truncated since it lies entirely within the particle.

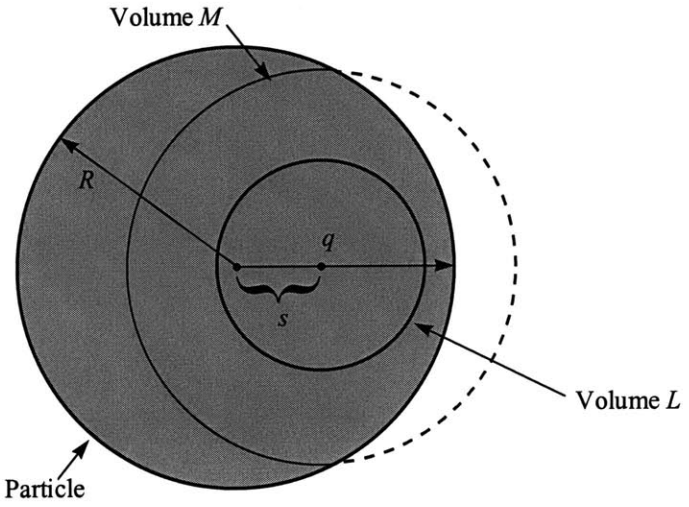

Figure 2-7. Cross-section of particle and nucleation volumes at different times.

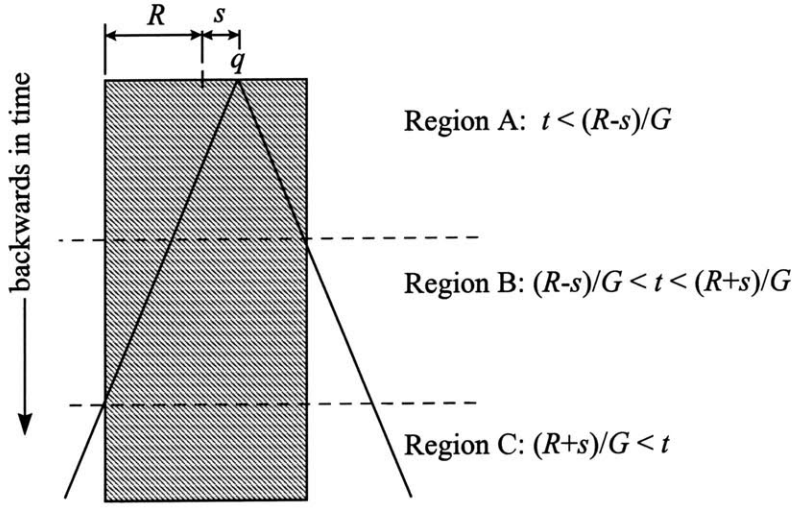

Figure 2-8. An exploded view of the cone of influence expanding backwards in time from a point q through a spherical particle. The impinged region for the cone volume is given as a function of particle radius R, distance from center of particle s, and growth rate G.

In this derivation, the primary assumptions are that the nucleation events (or seeds) are randomly distributed within the particle, and that the nucleation events can be described by a Poisson distribution. In addition, surfaces are assumed to have no effect other than to define the limits of the volume (i.e. surface nucleation is not considered). Finally, it is assumed that there are no particle-particle interactions (e.g. the transformed surface of one particle acting as a seed for another). The mathematical limits of the time cone can be described by the parameters *s*, *R*, *G*, and *t*. As shown in Figure 2-8, there are three different integration limits for the boundaries of the time-cone, so numerical integration must be used. In order to set up this problem, an array of 100 points were evenly spaced along the radius of a particle. The cone volume was calculated for each point at each time step, multiplied by the probability of nucleation, and numerically integrated over time. This would give the expected number of nuclei in the volume at time *t*, which is $\langle N \rangle_C$ using Cahn's notation. The probability that this point has not transformed is then:

$$P = e^{-\langle N \rangle_C} \qquad \text{(Equation 2-5)}$$

This probability for each point along the radius is then weighted to account for the difference in relative volume that each point represents due to the spherical geometry of the particle. The fraction that has transformed is then given by 1-*P*. A spreadsheet was used to perform the repetitive calculations necessary to create the model.

Values for the growth rate and nucleation rate were approximated by fitting Avrami curves to literature data [2] for compacts of seeded and unseeded γ-Al_2O_3 systems transformed isothermally at 1050°C. This approach would only provide an order of magnitude approximation for these values, but it should give some insight into the effect of particle size on the transformation kinetics of finite γ-Al_2O_3 particles.

2.4.2 Finite Size Effects on Seeded and Unseeded Systems

The plots obtained by applying the above model and fitted data to particles of various diameters are shown in Figures 2-9 and 2-10. These plots were produced by using a growth rate of 4 Å/s, and either a homogeneous nucleation rate of 10^6 events/cm^3·s or a seed

density of $3x10^{13}$ seeds/cm^3. In both figures, the transformation curves for a semi-infinite material are also plotted using the JMAK model for spherical transformation volumes (using Equations 2-1 and 2-2 for the unseeded and seeded cases, respectively).

Reduction of the particle size significantly affects the time necessary to achieve complete conversion in the case of spontaneous nucleation (Figure 2-9). As the particle size is reduced, the volume within which a nucleation event can occur is also reduced so that nucleation is much less likely to occur. Since the growth phase of the transformation will be relatively rapid compared to the time scale of nucleation within small particles, the transformation kinetics become essentially nucleation-controlled. The greatest disparity between this finite particle model and a real system may be attributed to neglecting particle-particle interactions in the former. In a real system, particle-particle interactions would undoubtedly occur and could greatly reduce the time required for complete transformation. In fact, the microstructure of transformed alumina suggests that particle-particle interactions do take place under spontaneous nucleation conditions. The transformed α-Al_2O_3 areas have been described as (i) porous single crystals (several times larger than the parent γ-Al_2O_3 crystallites) or (ii) made up of several crystallites with low-angle grain boundaries. In either case, the structure is very similar to what might be expected if particle-particle interactions occurred on a large scale with minimal sintering during phase transformation.

The effect of a reduced particle size on the transformation of a seeded system is less significant due to the fact that the nucleation is not time-dependent. In this case, the number of nuclei per particle is determined by the size of the particle. As the particle size decreases, the number of nuclei per particle decreases so that transformation becomes growth-controlled. In the extreme case, there are fewer nuclei than particles and the transformation does not proceed to completion. This is illustrated in Figure 2-10 whereby the finest particles ($\leq$0.3 μm-sized) do not approach full conversion due to the shortage of nuclei. This upper limit in transformation is partially due to the restriction that spontaneous nucleation cannot occur in this system. A comparison of the time scales for spontaneous nucleation of smaller particles and transformation times for a seeded system suggests that

this is not a bad approximation. For example, it takes ~10^7 vs. $10^{2.7}$ seconds for 50% conversion of unseeded vs. seeded particles of 0.5 μm diameter.

Other researchers have relied upon the statistical analysis of computer simulations to determine the effect of finite size on the transformation kinetics. In particular, Levine *et al.* [47] suggested a truncated polynomial equation of the form,

$$x_v(R) \approx 1 - \exp\left[-N\left(L^3 - \frac{9}{16}L^4 + \frac{m}{32}L^6\right)\right] \qquad \text{(Equation 2-6)}$$

where N is equal to the number of spherical nuclei growing in the particle, and L is equal to the radius of the transformed region divided by the particle radius. For large numbers of nuclei per particle (i.e. large N), the solution is exact with $m = 1$. However, when fewer nuclei are present in the particle, the correction factor m is given by the larger of

$$\begin{Bmatrix} 5.26 - 0.26N \\ 1.0 \end{Bmatrix} \qquad \text{(Equation 2-7)}$$

in order to obtain reasonable fit with the computer simulations. The finite particle model derived here fits the computer simulations and Levine *et al.*'s formula [47] very well for seeded systems. It is difficult, however, to compare this finite particle model with Levine *et al.*'s model for the case of spontaneous nucleation because the nucleation rate they used was independent of volume -- an assumption that is not very realistic. The model derived here is superior to Levine *et al.*'s model in that it does not involve the approximations used in the latter, and that it includes the effect of volume change on the nucleation probability within finite particles. However, this model is much more complex and difficult to apply to systems that are not well characterized.

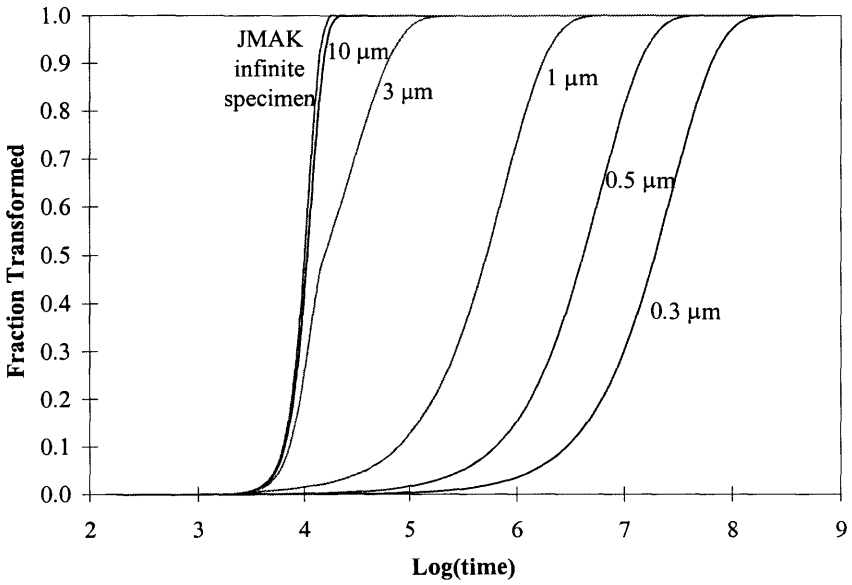

Figure 2-9. Isothermal transformation plots as a function of time (in seconds) for unseeded systems (spontaneous nucleation I at 10^6 events/cm^3·s) of different particle sizes ($G = 4$ Å/s).

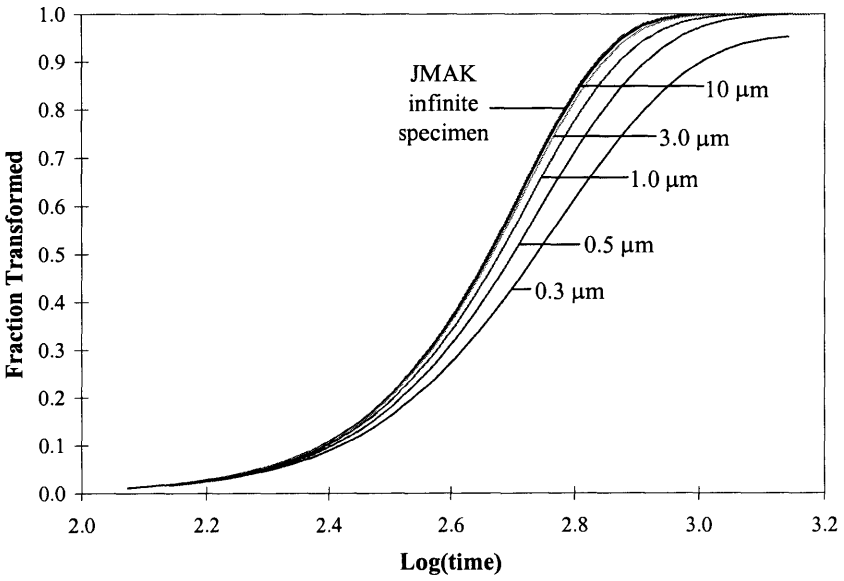

Figure 2-10. Isothermal transformation plots as a function of time (in seconds) for seeded systems (I = 3x10^{13} seeds/cm^3) of different particle sizes (G = 4 Å/s).

2.4.3 Effect of Finite Particle Size on JMAK Evaluation of Transformation Kinetics

The effect of finite particle size on the transformation kinetics can be seen in Figures 2-11 and 2-12. These plots were created by applying the linearized JMAK expression (Equation 2-4) to the fraction transformed values of the finite particle model (Figures 2-9 and 2-10). The JMAK model is widely applied to determine the kinetics of a nucleation-and-growth transformation. This is because most of the other models (including the one derived here) require a great deal of initial knowledge about the system and are cumbersome to apply for many complex particle or growth geometries. The goal, therefore, is to see how the finite particle size affects the kinetics that would normally be determined by applying the JMAK model to an "unknown" finite particle system. Figures 2-11 and 2-12 show that the transformations can be reasonably fitted by the JMAK model. The poorest fits to the JMAK model occur at intermediate particle sizes for the case of spontaneous nucleation, and at small particle sizes for the seeded system. In the case of spontaneous nucleation, the poor fit is due to the fundamental shift in the rate-limiting step from nucleation-and-growth controlled (n = 4) to purely nucleation-controlled (n = 1). For seeded systems of small particles, the kinetics are no longer limiting the transformation. Instead, the probability of a nuclei present in the particle becomes the controlling factor, and the slope decreases from the expected value of 3. The effect of finite size on the effective rate constant as determined from these plots is illustrated in Figure 2-13. Particle size has a large effect on the apparent reaction rate in the case of spontaneous nucleation, but gives rise to only a small shift in the observed reaction rate for the seeded system.

These results suggest that the system of interest (i.e. a seeded system of finite size) can be reasonably well evaluated by applying the JMAK model. The kinetics of the transformation are only modestly affected by the finite nature of the system. Therefore, the JMAK method of analysis can be used as a simple and reasonable approach to determine the kinetics and the activation energy of the transformation process in γ-Al_2O_3 samples that have been seeded via high-energy ball milling.

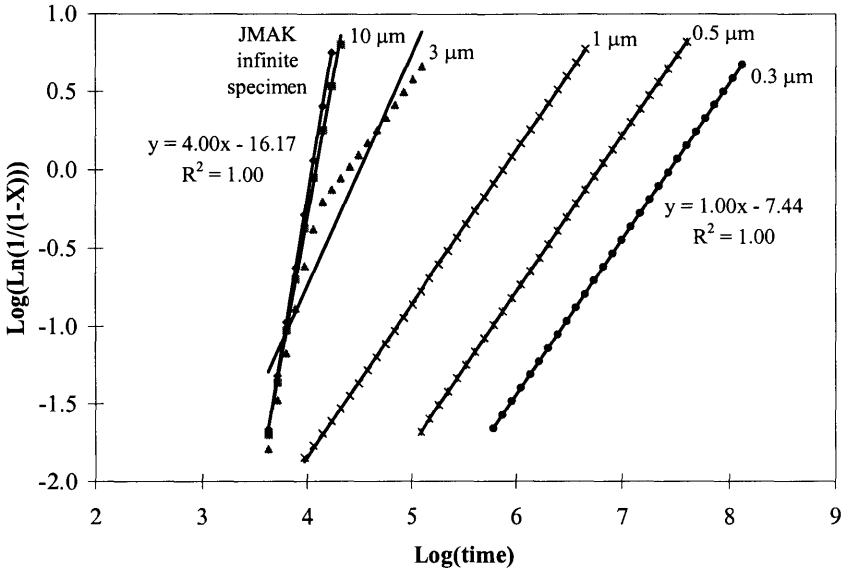

Figure 2-11. Data of JMAK model and finite particle model from Figure 2-9 (unseeded systems) plotted using the linearized JMAK expression (Equation 2-4) as a function of time (in seconds).

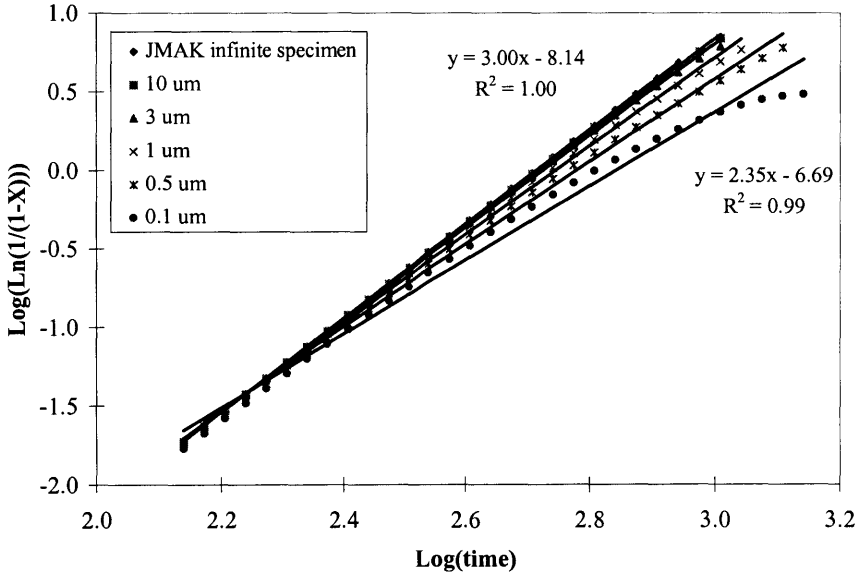

Figure 2-12. Data of JMAK model and finite particle model from Figure 2-10 (seeded systems) plotted using the linearized JMAK expression (Equation 2-4) as a function of time (in seconds).

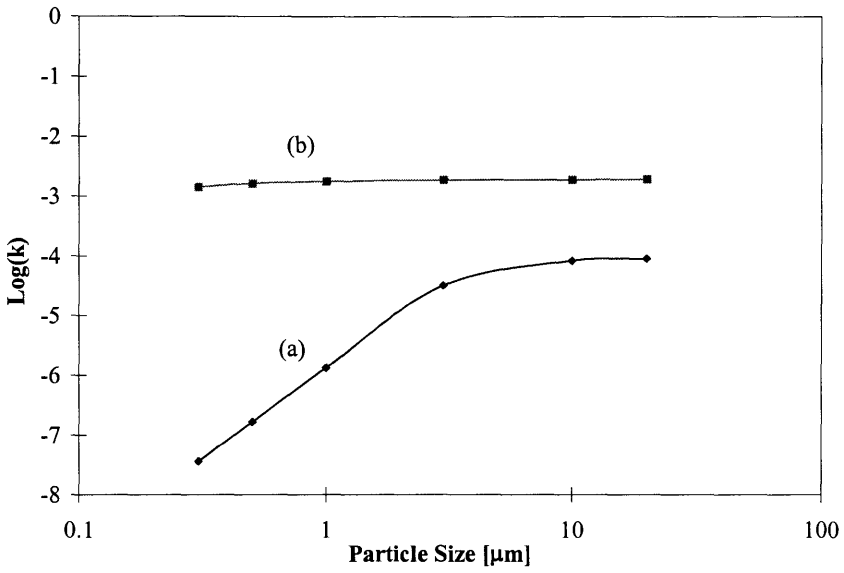

Figure 2-13. Effect of particle size on the reaction rate constant k as obtained by applying the linearized JMAK expression (Equation 2-4) to the transformation kinetics of the finite particle model for (a) unseeded and (b) seeded systems. Values for $n \cdot \text{Log}(k)$ are obtained from the y-intercepts of plots in Figures 2-11 and 2-12 for the unseeded and seeded systems, respectively.

2.5 Conclusions

The transformation kinetics of alumina have been demonstrated to be greatly affected by high-energy ball milling of γ-Al_2O_3 powders. It was shown that high-energy ball milling even for short periods of time could have a large effect on the transformation temperature, which was reduced by >250°C after only 2 hours of milling. The kinetics of the transformation were analyzed using the JMAK model; the activation energy obtained for the transformation (333 kJ/mol) was consistent with previous researchers who used external seeding approaches. To judge the applicability of the JMAK transformation model to a finite particle system, such as that investigated here, a new model was developed that incorporated the effects of finite particle size in the transformation kinetics. For seeded

systems with particle sizes greater than 0.3 μm, the JMAK model and the finite particle model gave nearly equivalent results. This suggests that the JMAK model can be reliably employed to approximate the activation energy for seeded finite systems. On the other hand, the JMAK model does not work well for cases of strictly homogeneous, bulk nucleation in the absence of particle-particle interactions. Incorporating the effects of surface nucleation and particle-particle interactions into the finite particle model would better approximate real systems.

2.6 References

[1] W. A. Yarbrough and R. Roy, "Microstructural Evolution in Sintering of AlOOH Gels," *J. Mater. Res.*, **2** [4] 494-515 (1987).

[2] G. L. Messing and J. C. Huling, "Transformation, Microstructure Development and Sintering in Nucleated Alumina Gels"; pp. 669-79 in *Processing of Ceramics,* Proceedings of the 3rd European Ceramic Society Conference, Vol. 1. Edited by P. Duran and J. F. Fernandez. Faenze Editrice Iberica S.L., 1993.

[3] L. A. Xue and I. W. Chen, "Influence of Chemical Additives on the γ-to-α Transformation of Alumina," *J. Mater. Sci. Lett.*, **11** [8] 443-45 (1992).

[4] J. McArdle, G. Messing, L. Tietz, and C. Carter, "Solid-Phase Epitaxy of Boehmite-Derived α-Alumina on Hematite Seed Particles," *J. Am. Ceram. Soc.*, **72** [5] 864-67 (1989).

[5] J. McArdle and G. Messing, "Transformation, Microstructure Development, and Densification in α-Fe_2O_3-Seeded Boehmite-Derived Alumina," *J. Am. Ceram. Soc.*, **76** [1] 214-22 (1993).

[6] M. Kumagai and G. L. Messing, "Enhanced Densification of Boehmite Sol-Gels by α-Alumina Seeding," *J. Am. Ceram. Soc.*, **67** [11] C230-31 (1984).

[7] M. Kumagai and G. L. Messing, "Controlled Transformation and Sintering of a Boehmite Sol-Gel by α-Alumina Seeding," *J. Am. Ceram. Soc.*, **68** [9] 500-05 (1985).

[8] R. A. Shelleman, G. L. Messing, and M. Kumagai, "Alpha Alumina Transformation in Seeded Boehmite Gels," *J. Non-Cryst. Solids*, **82**, 277-85 (1986).

[9] R. A. Shelleman and G. L. Messing, "Liquid-Phase-Assisted Transformation of Seeded γ-Alumina," *J. Am. Ceram. Soc.*, **71** [5] 317-22 (1988).

[10] G. L. Messing and M. Kumagai, "Low-Temperature Sintering of α-Alumina-Seeded Boehmite Gels," *Am. Ceram. Soc. Bull.*, **73** [10] 88-91 (1994).

[11] C. S. Nordahl and G. L. Messing, "Transformation and Densification of Nanocrystalline θ-Alumina during Sinter Forging," *J. Am. Ceram. Soc.*, **79** [12] 3149-54 (1996).

[12] O. Kwon, C. S. Nordahl, and G. L. Messing, "Submicrometer Transparent Alumina by Sinter Forging Seeded γ-Al_2O_3 Powders," *J. Am. Ceram. Soc.*, **78** [2] 491-94 (1995).

[13] L. Pach, R. Roy, and S. Komarneni, "Nucleation of Alpha Alumina in Boehmite Gel," *J. Mater. Res.*, **5** [2] 278-85 (1990).

[14] E. Prouzet, D. Fargeot, and J. F. Baumard, "Sintering of Boehmite-Derived Transition Alumina Seeded with Corundum," *J. Mater. Sci. Lett.*, **9**, 779-81 (1990).

[15] I. P. Kilbride and A. J. Barker, "Enhanced Densification by Seeding of Extruded Boehmite Gels Derived by Hydrothermal Decomposition of Basic Aluminium Acetate," *Brit. Ceram. Trans.*, **93** [5] 187-91 (1994).

[16] P. S. Jayan, N. Ananthaseshan, B. Subramaniam, and M. V. Murugappan, "Process for the Preparation of Alumina Abrasives," U.S. Pat. No. 5782940, Jul. 21, 1998.

[17] T. E. Cottringer, R. H. van de Werde, R. Bauer, and W. A. Yarbrough, "Abrasive Material and Method," U.S. Patent No. 5395407, Mar. 7, 1995.

[18] T. E. Wood, "Impregnation Method for Transformation of Transition Alumina to a Alpha Alumina," U.S. Patent No. 5139978, Aug. 18, 1992.

[19] L. Pach, S. Kovalik, J. Majling, and J. Kozankova, "Effect of Pressure on α-Alumina Nucleation in Boehmite Gel," *J. Eur. Ceram. Soc.*, **12**, 249-55 (1993).

[20] T. Nishio and Y. Fujiki, "Phase Transformation Kinetics of Precursor Gel to α-Alumina," *J. Mater. Sci.*, **29** [13] 3408-14 (1994).

[21] Y. Ishitobi, M. Shimada, and M. Koizumi, "Sintering of Dense Alumina by Direct Transformation from Eta to Alpha Al_2O_3 Under High Pressure," *Proc. Round Table Meet. Spec.*, 113-33 (1979).

[22] E. K. Beauchamp and M. J. Carr, "Kinetics of Phase Change in Explosively Shock-Treated Alumina," *J. Am. Ceram. Soc.*, **73** [1] 49-53 (1990).

[23] O. V. Andryushkova, V. A. Ushakov, G. N. Kryukova, O. A. Kirichenko, and V. A. Poluboyarov, "Solid Phase Transformation of Mechanically Activated Alumina During Thermal Treatment," *Chem. Sust. Dev.*, **4**, 15-26 (1996).

[24] L. Kacsalova, "Transformation of Bayerite into α-Al_2O_3 Under Mechanical Impact," *Acta Chim. Acad. Sci. Hung.*, **99** [2] 115-20 (1979).

[25] M. L. Panchula and J. Y. Ying, "Mechanical Synthesis of Nanocrystalline α-Al_2O_3 Seeds for Enhanced Transformation Kinetics," *Nanostr. Mater.*, **9** [1-8] 161-64 (1996).

[26] M. L. Panchula and J. Y. Ying, "Enhanced Transformation and Sintering of Transitional Alumina through Mechanical Seeding"; pp. 319-333 in *Nanostructured Materials*. Edited by G.-M. Chow and N. Noskova. Kluwer Academic Publishers, Dordrecht, The Netherlands, 1998.

[27] A. Tonejc, C. Kosanovic, M. Stubicar, A. M. Tonejc, B. Subotic, and I. Smit, "Equivalence of Ball Milling and Thermal Treatment for Phase Transitions in the Al_2O_3 System," *J. Alloys Comp.*, **204**, L1-3 (1994).

[28] A. Tonejc, M. Stubicar, A. M. Tonejc, K. Kosanovic, B. Subotic, and I. Smit, "Transformation of γ-AlOOH (Boehmite) and $Al(OH)_3$ (Gibbsite) to α-Al_2O_3 (Corundum) Induced by High Energy Ball Milling," *J. Mater. Sci. Lett.*, **13** [7] 519-20 (1994).

[29] P. A. Zielinski, R. Schulz, S. Kaliaguine, and A. Van Neste, "Structural Transformations of Alumina by High Energy Ball Milling," *J. Mater. Res.*, **8** [11] 2985-92 (1993).

[30] M. V. Zdujic, O. B. Milosevic, and Lj. C. Karanovic, "Mechanochemical Treatment of ZnO and Al_2O_3 Powders by Ball Milling," *Mater. Lett.*, **13**, 125-29 (1992).

[31] R. B. Bagwell and G. L. Messing, "Effect of Seeding and Water Vapor on the Nucleation and Growth of α-Al_2O_3 from γ-Al_2O_3," *J. Am. Ceram. Soc.*, **82** [4] 825-32 (1999).

[32] S. K. Mehta, A. Kalsotra, and M. Murat, "A New Approach to Phase Transformations in Gibbsite: The Role of Crystallinity," *Therm. Acta*, **205**, 191-203 (1992).

[33] J. M. McHale, A. Auroux, A. J. Perrotta, and A. Navrotsky, "Surface Energies and Thermodynamic Phase Stability in Nanocrystalline Aluminas," *Science*, **277**, 788-91 (1997).

[34] J. M. McHale, A. Navrotsky, and A. J. Perrotta, "Effects of Increased Surface Area and Chemisorbed H_2O on the Relative Stability of Nanocrystalline γ-Al_2O_3 and α-Al_2O_3," *J. Phys. Chem. B,* **101** [4] 603-13 (1996).

[35] K. J. D. Mackenzie and G. Hosseini, "Effect of Electric Fields on the Transformation of Gamma to Alpha Alumina," *Trans. J. Brit. Ceram. Soc.*, **77** [6] 172-76 (1976).

[36] A. Kochendorfer, *Z. Kristallogr.*, **105**, 393 (1944).

[37] H. Schaper and L. L. Van Reijen, "A Quantitative Investigation of the Phase Transformation of Gamma to Alpha Alumina With High Temperature DTA," *Therm. Acta,* **77**, 383-93 (1984).

[38] C. C. Koch, "Mechanical Milling and Alloying"; Chapter 5, pp. 194-245 in *Processing of Metals and Alloys*, Materials Science and Technology, Vol. 15. Edited by R. W. Cahn, P. Haasen, and E. J. Kramer. VCH, New York, NY, 1991.

[39] J. W. Cahn, "The Kinetics of Grain Boundary Nucleated Reactions," *Acta Metall.*, **4** 449-59 (1956).

[40] M. Avrami, "Kinetics of Phase Change I," *J. Chem. Phys.*, **7**, 1103-12 (1939).

[41] M. Avrami, "Kinetics of Phase Change II," *J. Chem. Phys.*, **8**, 212-24 (1940).

[42] M. Avrami, "Kinetics of Phase Change III," *J. Chem. Phys.*, **9**, 177-84 (1941).

[43] M. C. Weinberg and D. P. Birnie III, "Transformation Kinetics for Randomly Oriented Anistropic Particles," *J. Non-Cryst. Solids*, **189**, 161-66 (1995).

[44] H. P. Klug and L. E. Alexander, *X-ray Diffraction Procedures*. John Wiley & Sons, New York, NY, 1974.

[45] J. W. Cahn, "The Time Cone Method for Nucleation and Growth Kinetics on a Finite Domain," *Mater. Res. Soc. Symp. Proc.,* **398**, 425-37 (1996).

[46] H. Orihara and Y. Ishibashi, "A Statistical Theory of Nucleation and Growth in Finite Systems," *J. Phys. Soc. Jpn.,* **61** [6] 1919-25 (1992).

[47] L. E. Levine, K. L. Narayan, and K. F. Kelton, "Finite Size Corrections for the Johnson-Mehl-Avrami-Kolmogorov Equation," *J. Mater. Res.*, **12** [1] 124-32 (1997).

3. Densification and Microstructural Characterization of Alumina

This chapter describes the effects of mechanical seeding on the sinterability of alumina powder. After high-energy ball milling, the powder was washed for impurity removal, jar milled to reduce particle agglomeration, and then hot pressed. Density as a function of hot pressing temperature was reported for samples milled with WC/Co and ZrO_2 ball-and-vial sets. The differences in the densification behavior between these samples were discussed and related to the seeding effects and milling detritus. Fracture surfaces as well as polished and etched surfaces of the densified samples were examined to illustrate the morphological differences between seeded and unseeded alumina samples.

3.1 Post-HEBM Processing

After HEBM, the powder contained significant amounts of WC/Co or ZrO_2 impurities due to wear of the milling media and container. Samples milled in WC/Co containers could be purified with aqua regia before further processing. Unfortunately, the ZrO_2 impurities could not be removed by a similar technique because of the chemical stability of ZrO_2. The removal of the WC/Co was performed by mixing approximately 5 g of milled alumina in a solution of 120 ml of 37 vol% hydrochloric acid, 40 ml of 69 vol% nitric acid, and 40 ml of water in a Teflon beaker. The acid solution is highly corrosive and must be handled with extreme care. The water was added to prevent the aqua regia from releasing "objectionable quantities of chlorine and other gases" [1]. Following the aqua regia wash, the powders were further washed by centrifugation with water and ethanol, and then dried. A plot of the tungsten content, determined by chemical analysis (Luvak, Inc. Waltham MA), as a function of washing time is shown in Figure 3-1 for the powder that had been milled in a WC/Co ball-and-vial set for two hours. By washing the powder for 12 hours, it was possible to reduce the tungsten content to approximately 0.02 wt%. This is equivalent to a W/Al molar ratio of 55 ppm.

In order to remove agglomerates and produce a more uniform powder, the samples that had been high-energy milled and washed with aqua regia were jar milled in polypropylene containers with ethanol and ZrO_2 media for 12 hours. Particle size

measurements (Horiba CAPA-500 centrifugal particle size analyzer) showed that after this process the particle size distributions of the 30-, 60-, and 120-minute WC/Co-milled powders were similar with a volume-averaged particle size of 0.65 μm. Approximately 70 vol% of the powder was finer than 1 μm and the particle size distribution had a log-normal distribution with a tail extending to about 5 μm. The unseeded powder had a larger average particle size of 1.5 μm, with a maximum particle size of less than 5 μm. Following jar milling, the seeded alumina powders were dried and calcined at 600°C to convert any aluminum hydroxides produced during the acidic washing step back to γ-Al_2O_3 prior to the sintering studies.

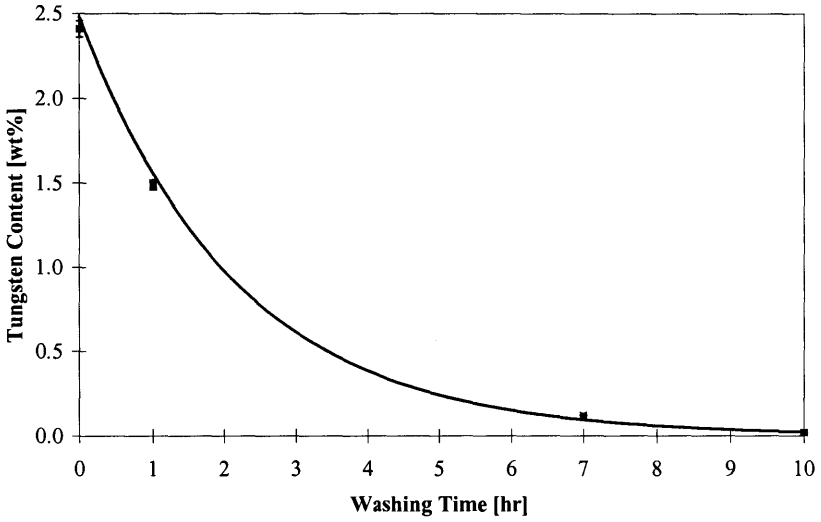

Figure 3-1. Effect of aqua regia wash time on the tungsten content in the γ-Al_2O_3 powder that had been milled with a WC/Co ball-and-vial set for two hours.

3.2 Densification

The samples were densified via uniaxial hot pressing in a MRF graphite hot press under 50 MPa of applied pressure. Approximately 3 g of powder was placed into a ½ inch-diameter graphite die, and evacuated and purged 3 times with nitrogen in the hot press. After the final evacuation, the load was applied and the temperature was ramped at 25°C/min to the sintering temperature. After soaking at the sintering temperature for 30

minutes, the pressure was released and the press was cooled to room temperature. The entire cycle time was less than 3 hours.

3.2.1 Effect of Seeding on Alumina Densification

Densification curves for unmilled and WC/Co-milled alumina powders are shown in Figure 3-2. It is clear that the high-energy milling had a large effect on the sintering of the alumina. The unmilled powder did not show any significant densification until 1300°C, whereas the milled materials have already achieved >90% of theoretical density by this temperature. Longer milling times also led to greater densification at a given sintering temperature. This suggested that seeding via HEBM and the associated increase in phase transformation kinetics did improve the densification of the alumina. Notably, near theoretical density was obtained at 1400°C in half an hour with powders that had been milled for only 30 minutes. The high-density pellets were nearly transparent except at the edges, although the small amount of residual tungsten and cobalt tended to give them a dark coloring. Chemical analysis results of the WC/Co- and ZrO_2-milled powders used in the densification studies are shown in Table 3-1. The differences in tungsten content did not appear to have a large effect on the sinterability of the powders. This can be seen by comparing powders that had been milled for 30 and 60 minutes, which contained the same amount of tungsten after washing, but showed very different densification behaviors. In contrast, the 60-minute and 120-minute milled samples had very different tungsten contents, but exhibited similar densification behaviors. These results supported the hypothesis that the sintering behavior was governed by the milling time, and therefore seed concentration, rather than by the WC or Co impurities from the milling process.

The improvement in densification with high-energy ball milling occurred through two mechanisms. The primary mechanism was the increased nucleation density due to milling. The effect of seeding has been shown by many other researchers to have a large effect on both the resulting microstructure and the densification rate [2-4]. A second effect of the high-energy ball milling process was a significant reduction in the pore volume of the samples as shown in Figure 3-3. At the same time, the average pore diameter, determined

by the BJH method on the desorption isotherm, decreased from 7.7 nm to 5.7 nm during the first hour of milling. As described previously, the particle size distributions for the milled samples were nearly identical, so the decrease in pore volume and pore diameter was primarily a result of the intraparticle pore removal and the increase in particle density. The increased particle density led to an increase in the green density of the compacts. For instance, pellets made from powders that had been high-energy ball milled for 0, 30, 60 and 120 minutes achieved green densities that were 24%, 25%, 32%, and 39% of the theoretical α-Al_2O_3 density, respectively, when pressed in a stainless steel die at 50 MPa. These green densities would be considered quite low for conventional ceramic compacts. However, due to the nanocrystalline nature of the powders and the dry pressing process employed here, these low densities were not unexpected. If colloidal processing rather than dry pressing had been used, then green densities on the order of 45-50% of theoretical density could have been obtained as shown by other researchers [2,4]. The fact that the green densities were similar for samples milled for 0 and 30 minutes, while the densification curves were different, suggested that the increased nucleation density from HEBM had the primary role in increasing the densification.

X-ray diffraction patterns of several hot-pressed pellets are shown in Figure 3-4. While the unseeded specimen still contained significant amounts of δ- and θ-Al_2O_3 at 1000°C, the mechanically seeded samples have already transformed completely to α-Al_2O_3. The unseeded sample did completely transform to α-Al_2O_3 by 1100°C, however, its microstructure was very different from that of the seeded samples, as will be seen in the fracture surfaces of these materials (Section 3.3.1).

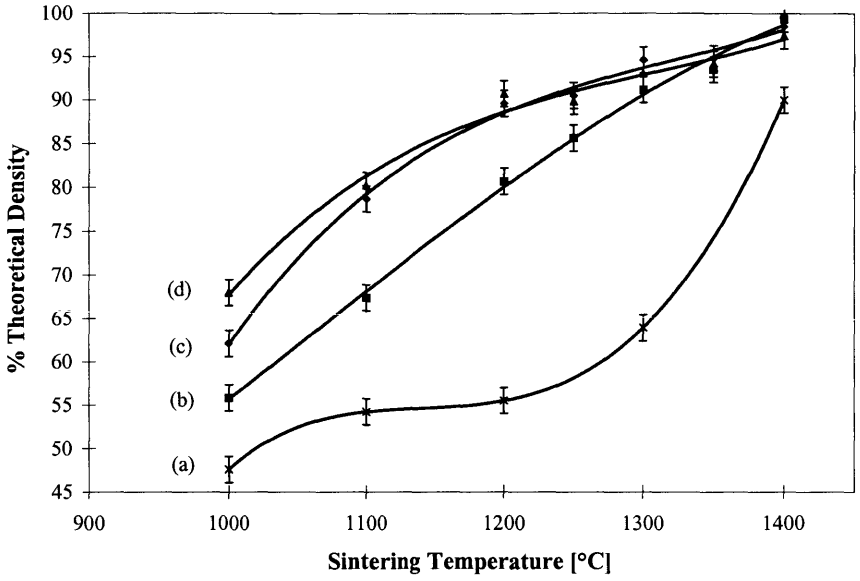

Figure 3-2. Hot-press densification curves for (a) unmilled γ-Al_2O_3 powders, and γ-Al_2O_3 powders that had been milled with a WC/Co ball-and-vial set for (b) 30 minutes, (c) 60 minutes, and (d) 120 minutes.

Table 3-1. Chemical analysis of γ-Al_2O_3 samples milled with WC/Co or ZrO_2 ball-and-vial sets. WC/Co-milled samples were washed with aqua regia for ~15 hours before analysis.

WC/Co-milled	wt % Tungsten	wt % Cobalt	wt% Silicon
30 min	0.029	<0.001	0.017
60 min	0.029	0.001	0.022
120 min	0.220	0.005	0.019

ZrO_2-milled	wt% Zirconium	wt% Yttrium	wt % Silicon
30 min	0.003	0.030	0.021
60 min	0.360	0.031	0.015
120 min	1.570	0.039	0.023

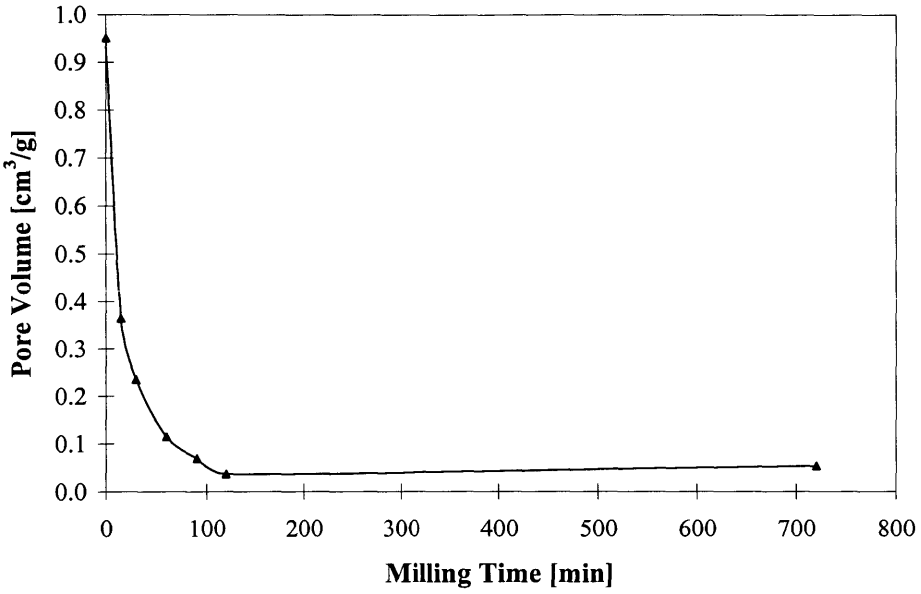

Figure 3-3. Pore volume of γ-Al_2O_3 powders milled for various time periods with a WC/Co ball-and-vial set.

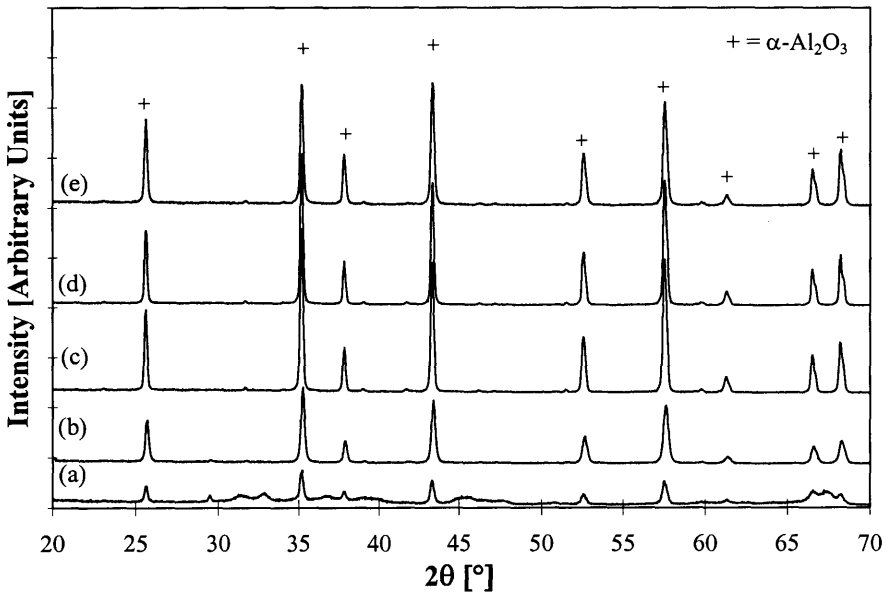

Figure 3-4. X-ray diffraction patterns of unseeded γ-Al_2O_3 samples hot pressed at (a) 1000°C and (b) 1100°C, and γ-Al_2O_3 samples hot pressed at 1000°C after milling with a WC/Co ball-and-vial set for (c) 30 minutes (d) 60 minutes, and (e) 120 minutes. α-Al_2O_3 peaks are marked by +. Other peaks correspond to δ- and θ-Al_2O_3.

Densification curves of the ZrO_2-milled samples are shown in Figure 3-5. Although the milling increased the sinterability of the powders, the effect was not as dramatic as in the case of WC/Co-milled powders. In addition, there was no distinct correlation between powder sinterability and milling time. It appeared that the sinterability of the powders improved with increased milling time from 30 to 60 minutes, and then decreased with further milling. The effect of milling time on the sinterability of ZrO_2-milled powders was complicated by impurity content. As mentioned earlier, the WC/Co-milled powders could be washed to remove most of the tungsten and cobalt impurities. The ZrO_2-milled samples, however, could not be purified by acid washes since ZrO_2 is nearly as stable as Al_2O_3. Therefore, the ZrO_2-milled alumina samples were processed and hot pressed with the ZrO_2 debris still present. It is interesting to note the rapid increase in impurity content with milling time as shown in Table 3-1. After 30 minutes of milling the powder contained only 0.003 wt % Zr, but the Zr content increased to approximately 0.36 wt% and 1.57 wt% after 60 minutes and 120 minutes of milling, respectively. It was hypothesized that the ZrO_2 particles introduced during HEBM hindered the densification of alumina. For milling times of 30 minutes and 60 minutes, the low levels of zirconia impurities did not appear to have a significant impact on sintering; however, the densification of the 120 minute-milled sample appeared to have been greatly retarded by the presence of 2.12 wt% ZrO_2. Other researchers have reported similar observations with ZrO_2-Al_2O_3 composites. For example, Lange *et al.* [5] reported that 2 vol% ZrO_2 additions to colloidally processed alumina could increase the temperature corresponding to maximum sintering rate and bulk densification by 100°C. The zirconia particles introduced by HEBM were probably not as homogeneously dispersed, nor as uniform in size, as those in Lange *et al.*'s study, so it was expected that the densification of alumina would be more adversely affected by the ZrO_2 addition in this study.

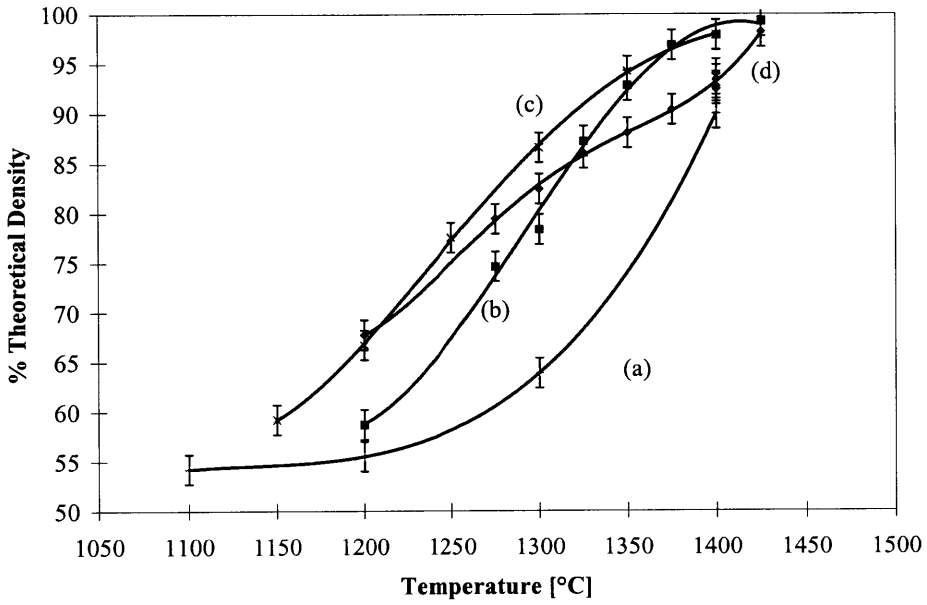

Figure 3-5. Hot-press densification curves for (a) unmilled γ-Al_2O_3 powders, and γ-Al_2O_3 powders that had been milled with a ZrO_2 ball-and-vial set for (b) 30 minutes, (c) 60 minutes, and (d) 120 minutes.

The dramatic increase in impurity level with milling time was not fully understood, but correlated with the reduction in the surface area of the powder (see Figure 2-2). There were two mechanisms through which this might have occurred. First, as the powder was compressed and the large soft agglomerates were replaced by smaller harder agglomerates, the alumina might have become more abrasive, increasing the wear rate of the ball-and-vial set. Second, as milling progressed, the volume of powder in the vial decreased through compaction. The reduced powder volume might allow the milling media to achieve a higher velocity, thereby increasing the impact energy during the milling process. Either of these two mechanisms could explain the increase in the wear rate, and a combination of these mechanisms might have led to the non-linear increase in impurity content with milling time.

A comparison in the sintering of WC/Co- and ZrO_2-milled powders is shown in Figure 3-6. These 30-minute milled samples have very low impurity contents and therefore should give the clearest insight into the differences in densification due to milling with the

two media. While both mechanically seeded samples densified better than the unmilled sample, the WC/Co-milled powder began sintering at lower temperatures than the ZrO_2-milled sample. This is somewhat surprising given that the decreases in the transformation temperatures and surface areas of the powders milled in the two media were fairly similar, as discussed in Section 2.3.2. The source of the different sintering behaviors was not clear, but might have to do with differences in the post-milling processing of the samples, or might be attributed to the density difference between the milling media. It was possible that the acid washing step, which both the unseeded and WC/Co-milled powders underwent, reduced the agglomerate size or strength allowing for improved powder packing. The large difference in the density of the milling media might also have affected the agglomerate strength, agglomerate density, and particle packing in the green compact, leading to different sinterabilities for the WC/Co-milled and ZrO_2-milled materials.

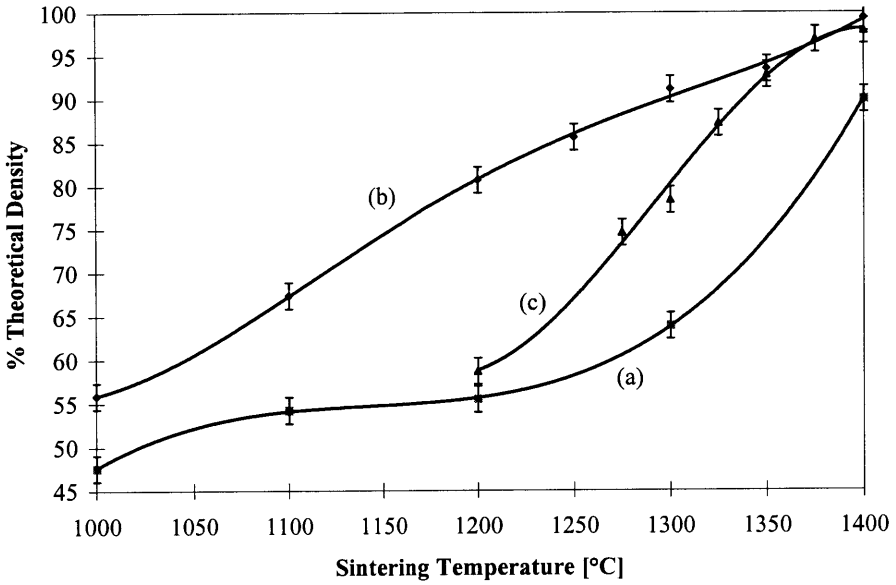

Figure 3-6. Hot-press densification curves for (a) unmilled γ-Al_2O_3 powders, and γ-Al_2O_3 powders that had been milled for 30 minutes with (b) WC/Co or (c) ZrO_2 ball-and-vial sets.

3.3 Microstructure

As expected from the results of other researchers on externally seeded alumina systems [6,7], the microstructure of the mechanically seeded alumina specimens was considerably different from that of the unseeded alumina. Fracture surfaces, as well as polished and etched surfaces, of the WC/Co-milled samples were used to investigate and quantify the differences in microstructure associated with milling time and hot-pressing temperature.

3.3.1 Fracture Surfaces

A JEOL 6320FV field emission gun scanning electron microscope was used to examine sample fracture surfaces that had been coated with ~60 Å of a Au-Pd alloy to prevent charging. Representative micrographs of the samples are shown in Figure 3-7. It was clear from these images that mechanical seeding had a significant effect on the microstructural development of Al_2O_3. The unseeded material displayed the characteristic vermicular structure observed in conventionally processed γ-Al_2O_3 powders, whereas the mechanically seeded materials showed a very different, dense particle morphology, even when hot pressed at low temperatures.

There might be two mechanisms through which the dense particle morphology improved the densification. During the early stages of heat treatment (~950°C), the seeded γ-Al_2O_3 underwent transformation to the α-Al_2O_3 phase with the associated ~11 vol% shrinkage. With the high nucleation density, however, the individual transformed volumes were kept small and discrete so that grains with low connectivity could rearrange under the applied load, thereby increasing sample density. During the final stages of hot pressing, this discrete, dense particle morphology promoted densification because the residual porosity was between the grains, and could be easily removed via grain boundary diffusion. In contrast, the vermicular structure of the unseeded γ-Al_2O_3 greatly hindered densification due to trapping of pores within the grains.

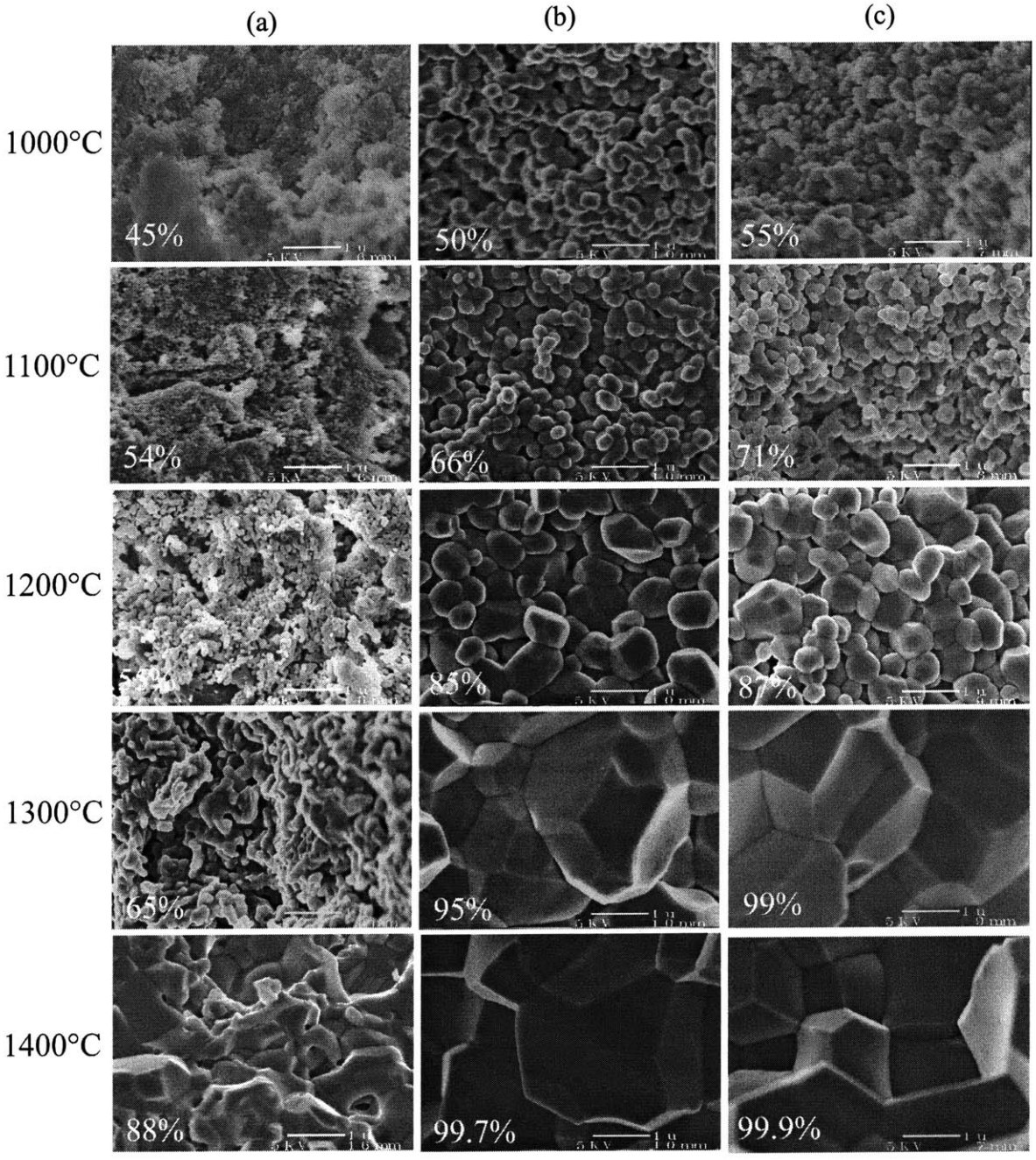

Figure 3-7. SEM micrographs of fracture surfaces for hot-pressed Al_2O_3 samples that (a) were not milled, or had been milled with a WC/Co ball-and-vial set for (b) 60 minutes and (c) 120 minutes. The samples were hot pressed for 30 minutes at the temperature shown on the left. The % theoretical density achieved by each sample is noted in white at the lower left hand corner of each micrograph.

3.3.2 Polished and Etched Surfaces

Polished and etched specimens were prepared using standard ceramographic polishing techniques with final polishing performed using a 0.1-μm diamond suspension. Chemical etching was preferred to thermal etching because the high temperatures or long times required for thermal etching could change the microstructure. Therefore, etching was performed by suspending samples from a gold wire in boiling phosphoric acid for 10-18 minutes, depending on sample density. Samples were coated with ~60 Å of Cr prior to imaging. Chromium was used, despite its oxidation susceptibility, instead of Au-Pd because it could be easily removed by the phosphoric acid if additional etching of the sample was necessary. Specimens <90% dense were difficult to prepare as polished specimens due to a propensity for grain pull-out and surface damage. Some representative micrographs of polished and etched surfaces of high-density specimens are shown in Figure 3-8. These micrographs were taken near the center of the pellets, which was more dense than the edges of the pellets due to frictional effects of the die walls. A few pellets were soaked at the sintering temperature for three hours, instead of 30 minutes, and it was found that the fully dense (transparent) center region grew significantly with a longer sintering period. The micrographs in Figure 3-8 illustrated that the grain size was on the order of a few microns for the WC/Co-milled samples hot pressed at 1400°C, and that there was very little porosity within the grains. The asymmetric appearance of the grain boundaries was due to chemical etching, which was more aggressive towards certain crystalline directions. In general, the grain size was quite uniform within the pellet with only small variations due to local density differences. Of over 100 micrographs examined, only 2 micrographs had grains that were 2-3 times larger than the average grain size. The sintering times for these samples were very short (30 minutes) and hot pressing was used so that grain growth, and in particular abnormal grain growth, would have little time to occur and would be suppressed by the applied pressure. On the other hand, these samples were processed without the use of MgO, so the ability to obtain fully dense specimens from mechanically seeded γ-Al_2O_3 without abnormal grain growth is noteworthy.

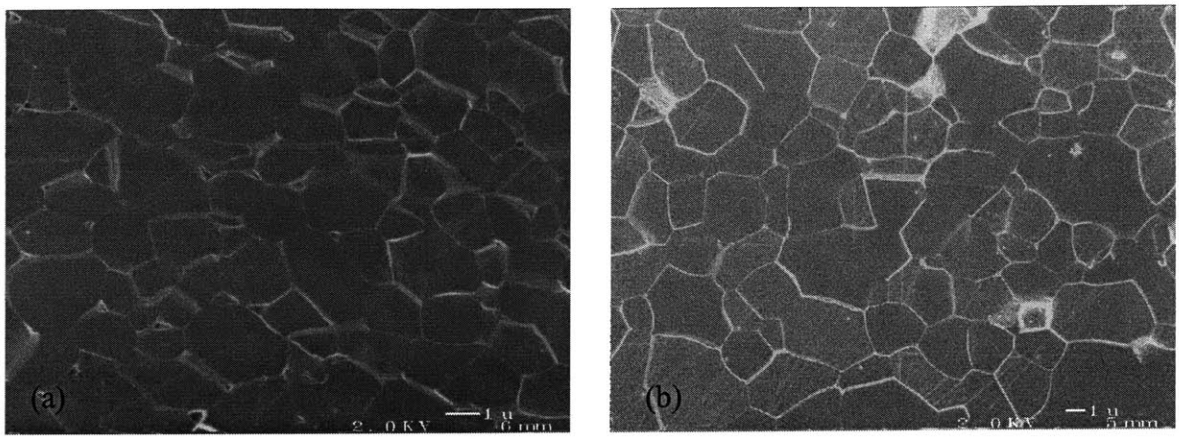

Figure 3-8. SEM micrographs of polished and chemically etched pellets after hot pressing at 1400°C for 30 minutes. Samples were prepared from γ-Al_2O_3 powders that had been milled with a WC/Co ball-and-vial set for (a) 30 minutes and (b) 120 minutes.

3.3.3 Grain Growth

In order to fully characterize this system, it is important to understand the effect of mechanical seeding on the average grain size in the sintered pellets. Toward this end, the lineal intercept method was applied to analyze the polished and etched surfaces of WC/Co-milled specimens that had been sintered to ≥90% of theoretical density. More than 500 grain intercepts were measured for each sample from micrographs that had been taken at random locations on the cross-sectional surface. The effect of porosity was taken into account by using the modified lineal intercept method of Wurst and Nelson [8]. Grain sizes of samples that were <90% dense were estimated from fracture surfaces. The average grain size as a function of % theoretical density was plotted in Figure 3-9. The mechanically seeded alumina underwent dramatic grain growth as the density exceeded 90%, which is common for many systems. Based on the transformation temperature studies of this thesis and the results of Messing and Huling [9], it would be logical to expect that as the milling time increased, the seed density would increase, and the average grain size would therefore decrease. This effect was apparent at low densities (i.e. immediately after the γ-to-α phase transformation), as shown by the decreasing grain size with increased milling time, but as densification continued this trend was obscured. During the final stages of densification

(i.e. after ≥90% of theoretical density has been achieved) the grain sizes of the samples became very similar, except for one outlying point. The coalescence of these trajectories was believed to be a result of the use of hot pressing, which would tend to limit grain growth. The samples that were milled for 30 minutes and 60 minutes have nearly the same grain growth trajectory, while the 120-minute milled sample grew rapidly at the highest sintering temperature, producing the outlying point, which might have to do with the high tungsten impurity level. As shown in Table 3-1, the tungsten impurity concentrations in the 30-minute and 60-minute milled samples were similar, but the 120-minute milled sample has ~8 times as much tungsten. It is possible that tungsten enhanced grain growth at high sintering temperatures, which would explain the large increase in grain size for the 120-minute milled sample. The effect of tungsten on grain growth as a function of temperature might be a topic for further investigation.

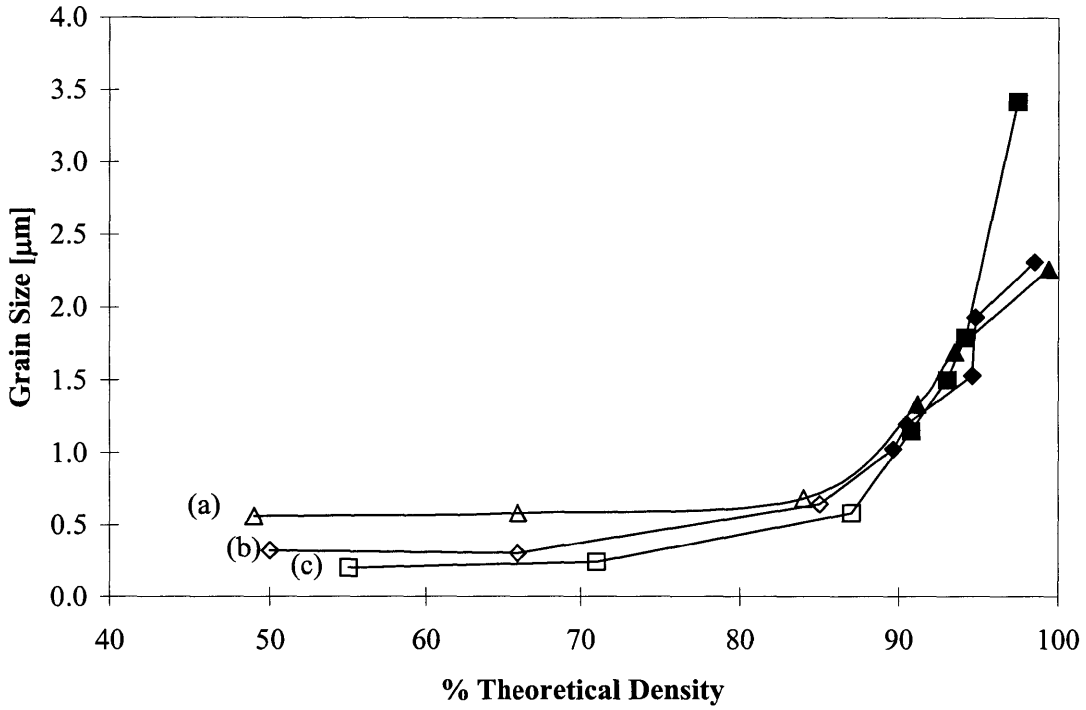

Figure 3-9. Grain growth trajectories for hot-pressed alumina samples that had been milled in a WC/Co ball-and-vial set for (a) 30 minutes, (b) 60 minutes, and (c) 120 minutes. Grain sizes for samples <90% dense (open symbols) and ≥90% dense (filled symbols) were estimated from fracture surfaces and polished/etched surfaces, respectively.

3.4 Conclusions

The densification of γ-Al_2O_3 powders was shown to be greatly enhanced by high-energy ball milling prior to compaction. The microstructures of hot pressed samples made from milled powders were substantially different from those made from unmilled powders. The milled samples tended to form discrete, dense particles after phase transformation, whereas the unmilled powders produced the characteristic vermicular structure that resisted densification. In addition, it was observed that densification was improved by milling for longer periods. While a significant fraction of the improvement in densification after milling was due to the increase in transformation rate and the corresponding changes in microstructural development, high-energy ball milling also allowed the samples to attain higher green densities, which might have also facilitated densification during hot pressing.

Finally, analysis of the mechanically seeded samples that were hot pressed to >90% of theoretical density showed very similar grain sizes, which might be attributed to the use of pressure-assisted densification. The various mechanically seeded alumina compacts were successfully hot pressed to full density without abnormal grain growth and without the need of MgO sintering additives.

3.5 References

[1] *Handbook of Chemistry and Physics,* 70th Edition, p. D-130. CRC Press, Inc., Boca Raton, FL, 1990.

[2] M. Kumagai and G. L. Messing, "Enhanced Densification of Boehmite Sol-Gels by α-Alumina Seeding," *J. Am. Ceram. Soc.*, **67** [11] C230-31 (1984).

[3] R. A. Shelleman, G. L. Messing, and M. Kumagai, "Alpha Alumina Transformation in Seeded Boehmite Gels," *J. Non-Cryst. Solids*, **82**, 277-85 (1986).

[4] M. Kumagai and G. L. Messing, "Controlled Transformation and Sintering of a Boehmite Sol-Gel by α-Alumina Seeding," *J. Am. Ceram. Soc.*, **68** [9] 500-05 (1985).

[5] F. F. Lange, T. Yamaguchi, B. I. Davis, and P. E. D. Morgan, "Effect of ZrO_2 Inclusions on the Sinterability of Al_2O_3," *J. Am. Ceram. Soc.*, **71** [6] 446-48 (1998).

[6] J. McArdle and G. Messing, "Transformation, Microstructure Development, and Densification in α-Fe_2O_3-Seeded Boehmite-Derived Alumina," *J. Am. Ceram. Soc.*, **76** [1] 214-22 (1993).

[7] K. Hirao, M. Ohashi, M. E. Brito, and S. Kanzaki, "Processing Strategy for Producing Highly Anistropic Silicon Nitride," *J. Am. Ceram. Soc.*, **78** [6] 1687-90 (1995).

[8] J. C. Wurst and J. A. Nelson, "Lineal Intercept Technique for Measuring Grain Size in Two-Phase Polycrystalline Ceramics," *J. Am. Ceram. Soc.*, **55** [2] 109 (1972).

[9] G. L. Messing and J. C. Huling, "Transformation, Microstructure Development and Sintering in Nucleated Alumina Gels"; pp. 669-79 in *Processing of Ceramics*,

Proceedings of the 3rd European Ceramic Society Conference, Vol. 1. Edited by P. Duran and J. F. Fernandez. Faenze Editrice Iberica S.L., 1993.

4. Synthesis of Nanocrystalline Aluminum Nitride

AlN powders to be used in advanced ceramics applications should have a small particle size to facilitate densification, a low oxygen content to maximize thermal conductivity, and low impurity levels to keep dielectric losses to a minimum. Commercially available powders typically contain 1-3 wt% oxygen and have an average particle size of 1-4 microns. The commercial AlN substrates are generally produced with yttria (Y_2O_3) and/or other oxide additives totaling 2-9 wt% to facilitate densification and to scavenge oxygen from the AlN grains. As beneficial as the sintering aids are to the densification and oxygen removal, the residual secondary phase from the incorporation of sintering aids can reduce the thermal conductivity of AlN by 10-15%. In theory, nanocrystalline AlN powders should densify at significantly lower temperatures than commercial microcrystalline powders, so that sintering additives would not be necessary. The first goal of this project, therefore, was to create and optimize a process for producing nanocrystalline AlN powders. This chapter describes the synthesis of nanocrystalline AlN and the physical and chemical properties of this powder.

4.1 Reactor Design and Modifications

The equipment used to produce the nanocrystalline AlN was a forced-flow reactor. A schematic of the reactor, which was designed and built by D. T. Castro [1] of our laboratory, is shown in Figure 4-1. The forced-flow reactor is a low-pressure reactor (1-30 mbar), which allows the production of high-purity and high surface area metal and metal nitride particles. The reactor can be divided into four zones. The first zone, to the left in Figure 4-1, is the evaporation chamber. In this area, a resistively heated graphite crucible is used to evaporate the metal. Gases metered in by mass flow controllers (MFC) flow past the crucible, quenching the metal or metal nitride vapors and capturing the particles. The gas stream then carries the particles into the second zone, which consists of a quartz tube within which a 2.45 GHz, 1000 W microwave plasma can be generated. The microwave plasma is used to atomize nitrogen molecules in the gas stream and reheat the particles to promote nitridation. This design of separate evaporation and reaction zones is important

since it prevents the molten metal in the crucible from nitriding, thereby allowing the metal to be evaporated continuously. The third zone is the sample collection area or filter assembly. The filter in this case is a non-woven metal fiber mesh (Sika-fil, G.K.N. Sinter Metals, Inc.), which captures the ultrafine particles from the gas stream. The filter collection unit can be sealed with gate valves and loaded into a glovebox without exposing the powder to air. This aspect is crucial, as many of the metal nitrides are oxygen- and water-sensitive. The fourth zone includes the throttle valve and vacuum pump system. The throttle valve is connected to a pressure sensor in the evaporation chamber and is automatically adjusted to maintain a constant pressure in the reactor during an evaporation run. The gases used were all 99.999% pure and, with the exception of ammonia, were passed through an oxygen trap prior to use. The aluminum feed was in the form of 99.99% pure aluminum wire (2 mm diameter) from Alfa-Aesar.

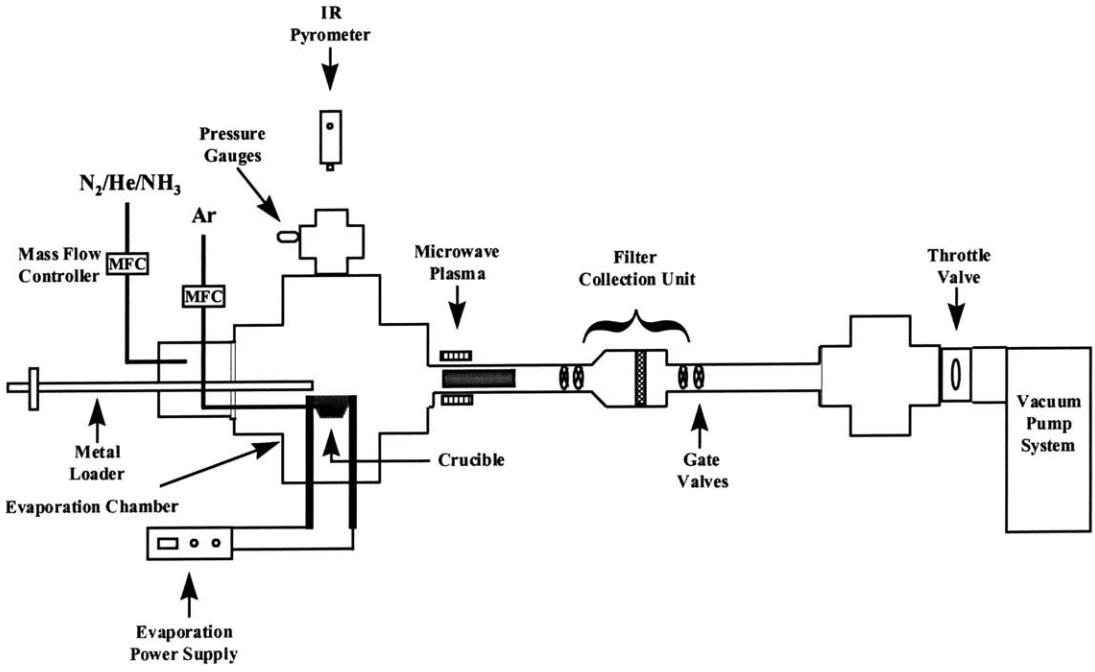

Figure 4-1. Schematic of the forced-flow reactor used in the production of nanocrystalline metals and metal nitrides (adapted from D. T. Castro [1]).

There were four major design changes made to the reactor over the course of this research. The first change was the introduction of a series of baffles and cones in order to

better direct the air flow within the evaporation chamber and produce a more laminar flow. This improved powder collection slightly by reducing the amount of material that impacted and adhered to the reactor walls. The second design change was the introduction of a crucible purge. This was accomplished by introducing argon into the melt zone via holes bored through the ends of the crucible. This purge improved the powder yield significantly, and allowed nitrogen and ammonia to be fed upstream of the crucible without nitridation of the melt prior to evaporation, thereby enhancing the degree of nitridation attainable. The crucible purge, in effect, separated the evaporation and nitridation zones with an argon flow. The third reactor design change involved the addition of a backflush system to the filter assembly. This allowed the filter to be cleared of powder with a blast of high-purity nitrogen so that the run could continue until the raw materials (i.e. metal supply) were completely consumed. The fourth major change was a refitting of all of the gas supply connections and valves with stainless steel components so that ammonia could be used as a reactant.

4.1.1 Reactor Variables and Effects

A reactor this complex has a large number of variables that might influence the powder characteristics and the production rate. A list of these variables is given in Table 4-1 along with standard operating conditions. It was found fairly early on during this research that the best way of evaporating aluminum was a flash evaporation method, whereby the crucible was heated between 1600°C and 2100°C, and the aluminum was added in small pieces so that each piece would evaporate entirely before further aluminum additions. In this way, the melt has little time to react with (a) the atmosphere to form AlN within the crucible, or (b) the crucible to form Al_4C_3. Both of these reactions still occurred but were minimized through this approach. The effects of the other reactor variables on the degree of nitridation and powder morphology are discussed in the following sections.

Table 4-1. Forced-flow reactor variables, ranges of conditions, and standard operating conditions for in-situ synthesis of nanocrystalline AlN (see Section 4.1.2 for details).

Variable	Range	Standard Conditions
Crucible Temperature	1500-2200°C	1900°C
Microwave Plasma	0-1000 Watts	0 Watts
Reactor Pressure	1-50 mbar	30 mbar
Gas Flow Rate	1-15 slpm	3.2 slpm
Nitriding Gas	N_2 and/or NH_3	N_2 and NH_3
Gas Composition	0-100% N_2 or NH_3	73% N_2, 27% NH_3
Crucible Purge (Ar)	0-1 slpm	0 slpm

4.1.2 Synthesis Methods

Two methods were initially examined for the production of nanocrystalline AlN. The first method was a post-synthesis nitridation process, whereby the forced-flow reactor was used to produce nanocrystalline aluminum that was later nitrided. This method is termed the "ex-situ" method since the nitridation was performed outside the forced-flow reactor. The second method was "in-situ" synthesis of nanocrystalline AlN. This was accomplished by introducing a nitriding gas into the forced-flow reactor so that nanocrystalline AlN could be produced directly.

4.1.2.1 Ex-Situ Nitridation

The first step in the ex-situ process was the generation of nanocrystalline aluminum. The optimal reactor conditions for nanocrystalline aluminum synthesis involved a helium flow rate of 2.3 slpm, a reactor pressure of 3 mbar, and a crucible temperature of 1700°C. The particles produced by this method were generally spherical and have a volume-averaged crystallite size of 30 nm as determined by Scherrer's method. The particles, however, have a broad size distribution ranging from 8 to 200 nm, as determined by transmission electron microscopy. Due to the short diffusion distances, these

nanocrystalline aluminum particles can be converted to AlN at surprisingly low temperatures. As shown in Figure 4-2, slow heating of nanocrystalline aluminum powder in a Perkin Elmer System 7 Thermogravimetric Analyzer (TGA) under a 80-sccm flow of nitrogen yielded a high degree of nitridation. At a temperature of 550°C, which is 110°C lower than the melting temperature of aluminum, the nanocrystalline aluminum was already >50% converted to AlN; full conversion was achieved at 700°C. The commercial aluminum (Aldrich), on the other hand, showed an insignificant amount of conversion (<6%) even at 700°C. These results indicated that the nitridation of nanocrystalline aluminum was greatly enhanced compared to that of conventional aluminum, which normally would require temperatures in excess of 1600°C to achieve full conversion.

The formation of AlN from aluminum nitridation is an exothermic reaction ($\Delta H^{\circ}_{f,298\ K}$ = -76.5 kcal/mol). As a result, the heating rate of the nanocrystalline aluminum had to be kept quite low (≤5°C/min) to prevent rapid heating of the sample and melting of the nanocrystalline aluminum. Since the nanocrystalline aluminum powder was fully converted by 700°C, well below the temperature range where rapid grain growth of AlN would occur, the AlN resulting from this ex-situ nitridation also had a nanocrystalline grain size. This is shown in Figure 4-3(b), which is an X-ray diffraction pattern of the nanocrystalline AlN powder derived from nitridation of nanocrystalline aluminum in the TGA at 900°C. The AlN synthesized in this manner has a 15-nm crystallite size and an unusually intense (002) peak. Textured growth of AlN has been reported previously, although usually in gas-phase synthesized powders. The additional peaks observed in this sample corresponded to aluminum oxynitride (AlON) diffractions, possibly from exposure of powder to air during the loading or operation of the TGA. Determination of the nitridation kinetics for nanocrystalline aluminum was thwarted by the broad particle size distribution since it prevented reasonable fits to standard diffusion-limited or reaction-limited models from being obtained.

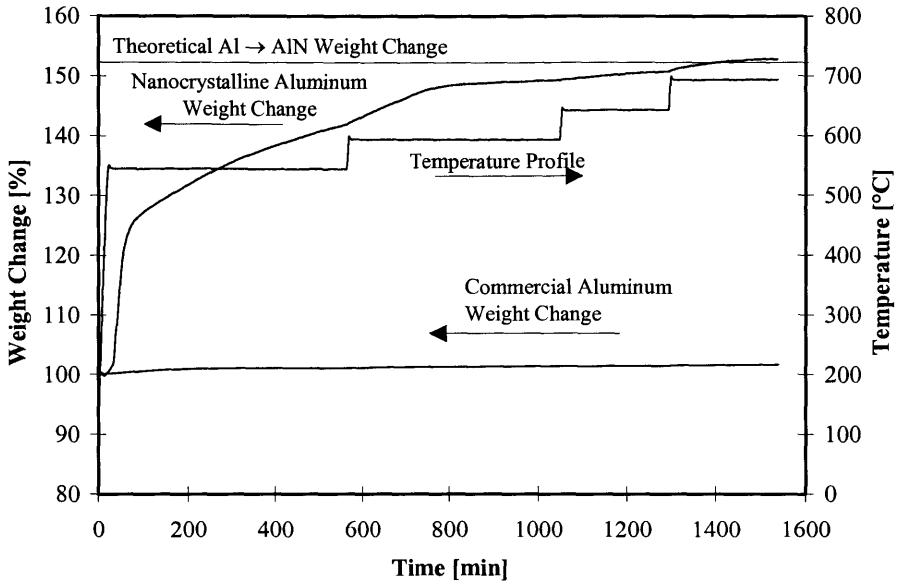

Figure 4-2. Nitridation of nanocrystalline aluminum *vs.* commercial aluminum (Aldrich) when heated in a nitrogen atmosphere in the TGA.

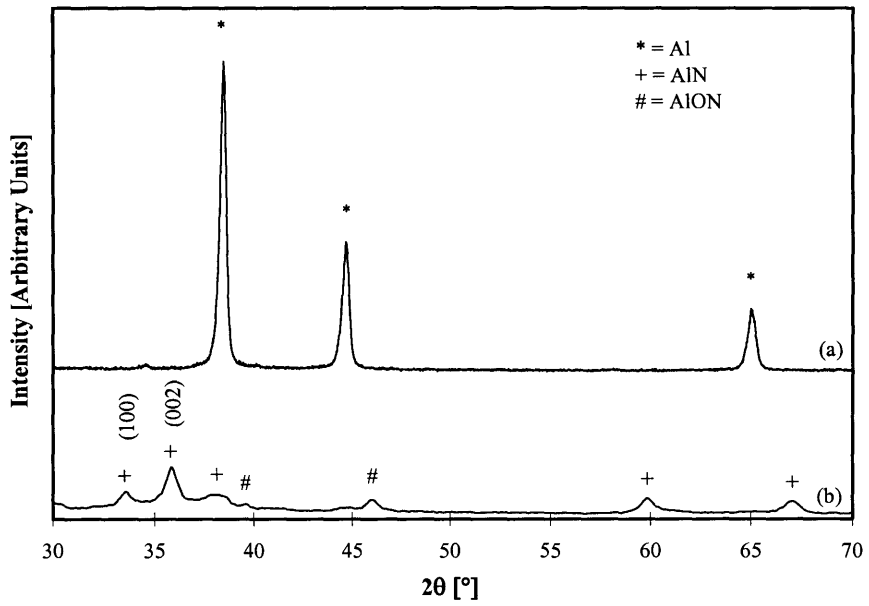

Figure 4-3. X-ray diffraction patterns of (a) the starting nanocrystalline aluminum powder, and (b) the nanocrystalline AlN powder produced by ex-situ nitridation of nanocrystalline aluminum with nitrogen in the TGA at 900°C.

4.1.2.2 In-Situ Nitridation

The in-situ synthesis of nanocrystalline AlN was more difficult than originally anticipated. Initially, attempts were made to produce nanocrystalline AlN simply by replacing the helium carrier gas (used to produce the nanocrystalline aluminum) with nitrogen/helium mixtures of various concentrations, and adjusting the reactor pressure. As shown in Figure 4-4(a), this proved to be unfruitful as the only crystalline material obtained was nanocrystalline aluminum instead of AlN. This was not particularly surprising, however, since nitrogen-nitrogen bonds are extremely stable, and extended soak periods at temperatures greater than 550°C were necessary to convert the nanocrystalline aluminum as shown in Figure 4-2. The next logical step was to use the microwave plasma [1] to help dissociate the nitrogen, reheat the particles, and promote nitridation. Powders synthesized with the microwave plasma were generally smaller, more uniform, and contained significantly more nitrogen. The use of the microwave plasma produced a mixture of Al and AlN phases (Figure 4-4(b)), giving a maximum of ~80 wt% nanocrystalline AlN, although the high microwave power levels (~800 W) necessary tended to reduce yields considerably. A more reactive nitridation gas, ammonia (NH_3), was then utilized without the microwave plasma for nanocrystalline AlN production (Figure 4-4(c)). Ammonia is much less stable than nitrogen; it dissociates at temperatures greater than 600°C to produce nitrogen and hydrogen. A glow appeared over the crucible when ammonia was added upstream of the evaporation zone. It was believed to result from the chemical decomposition of ammonia and the formation of nanocrystalline aluminum nitride. This in-situ nitridation synthesis with ammonia gas was used for all subsequent experiments since it resulted in a completely nitrided powder with a high yield and crystallite sizes between 10 nm and 100 nm under standard reactor operating conditions.

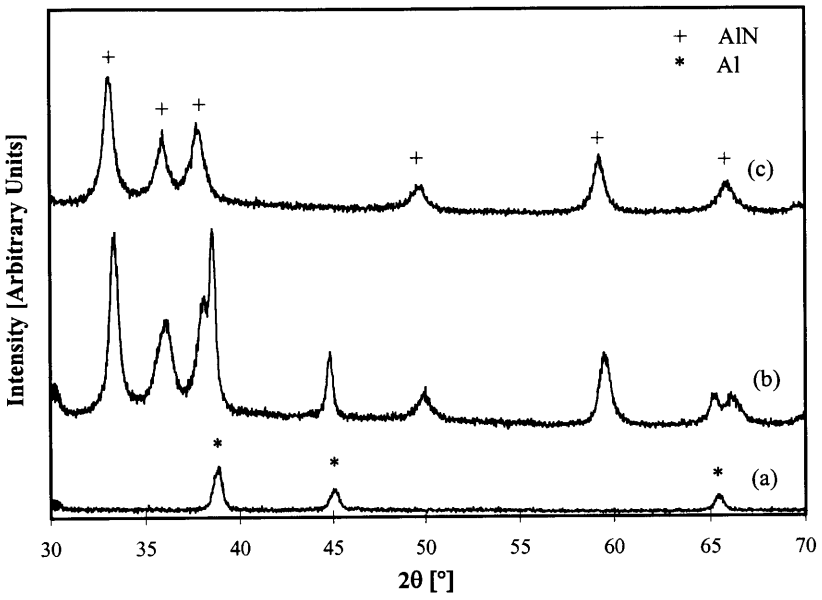

Figure 4-4. X-ray diffraction patterns of powders produced in the forced-flow reactor with (a) 45 vol% nitrogen, (b) 45 vol% nitrogen with the microwave operated at 800 W, and (c) 27 vol% ammonia; helium was used as the carrier gas in all cases.

4.2 Reactor Characterization

Once a reproducible and reliable method of producing nanocrystalline AlN had been determined, the next step was to examine which reactor parameters influenced the powder characteristics. The first variable that was examined was the amount of ammonia necessary to produce pure AlN powder. As expected, the amount of ammonia needed was strongly dependent upon the aluminum evaporation rate and the overall gas volume, but only weakly dependent on the reactor pressure, at least within the range examined (3-50 mbar). The degree of nitridation was relatively easy to approximate since nanocrystalline aluminum is black and nanocrystalline AlN is white. A pure white powder was produced at an ammonium concentration of ≥25 vol% with a total gas flow rate of ≥2 slpm. At lower flow rates, the evaporation of aluminum was faster than the ammonia addition rate, and a gray powder was produced unless the ammonia concentration was increased. The effects of reactor pressure, gas composition, and gas velocity on the surface area, crystallite size, and microstructure of nanocrystalline AlN particles were then systematically studied.

4.2.1 Effects of Reactor Pressure and Gas Composition

The effect of pressure on gas-phase reactors has been previously investigated by a number of researchers. In general, it has been found that as the reactor pressure is reduced, the vapor from the evaporation zone diffuses more rapidly, resulting in (a) less frequent collisions and (b) more rapid motion away from the growth zone [2]. Both of these effects result in smaller crystallite sizes as the reactor pressure is decreased. This trend was observed for the forced-flow reactor used in this study as well. The AlN powder produced in this reactor had a crystallite size of 10 to 100 nm with a surface area of 40-360 m^2/g (Figures 4-5 and 4-6).

One interesting phenomenon that was not anticipated was the effect of the carrier gas on the crystallite size and surface area of the resulting powder. As shown in Figures 4-5 and 4-6, the use of nitrogen rather than helium nearly doubled the crystallite size and significantly reduced the surface area of the nanocrystalline AlN powders produced. This was unexpected since the nitrogen did not appear to interact very strongly with the aluminum during initial screening experiments (i.e. no AlN was produced in a pure nitrogen stream). However, it appeared that nitrogen as a carrier gas affected the morphology and size of the AlN particles significantly. During much of this research, the goal was to optimize the reactor conditions for producing AlN with the finest crystallite sizes and the highest surface areas attainable. Only after many iterations between powder synthesis and sintering experiments was it discovered that the most easily densified powders were produced when nitrogen was used as the carrier gas and the reactor was operated at high pressures (30 mbar). Transmission electron microscopy, surface area analysis, and XRD crystallite size analysis suggested that the powders produced under a N_2/NH_3 flow probably sintered more easily because the particles were more discrete and equiaxed. Generally, the powders produced in a He/NH_3 flow consisted of many more needle-shaped particles and tended to form aggregates, thereby lowering the particle packing efficiency during dry pressing and affecting the crystallographic texture of the hot-pressed material. These effects will be described in detail in Chapter 5.

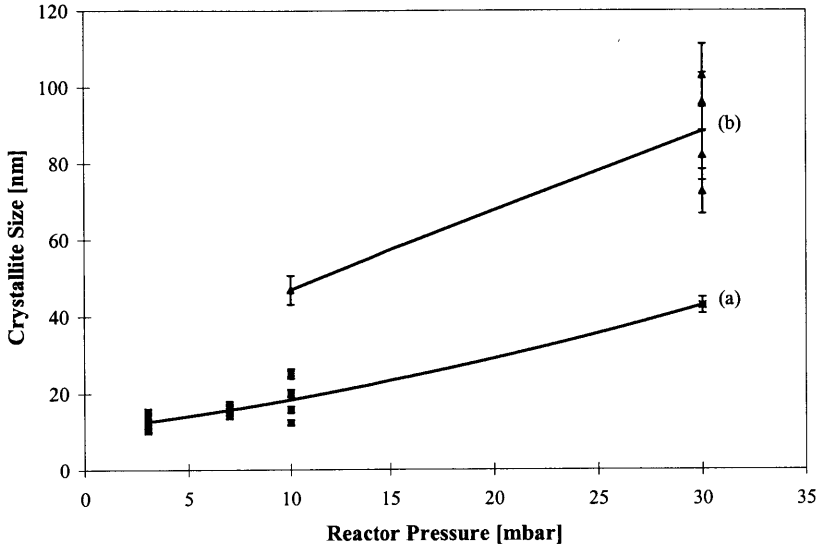

Figure 4-5. Crystallite sizes of AlN produced at various reactor pressures with (a) helium and (b) nitrogen as the carrier gas. The variability in the data was due to differences in the gas velocity used (see Section 4.2.2), and the increased error in Scherrer's analysis as the crystallite size approached 100 nm.

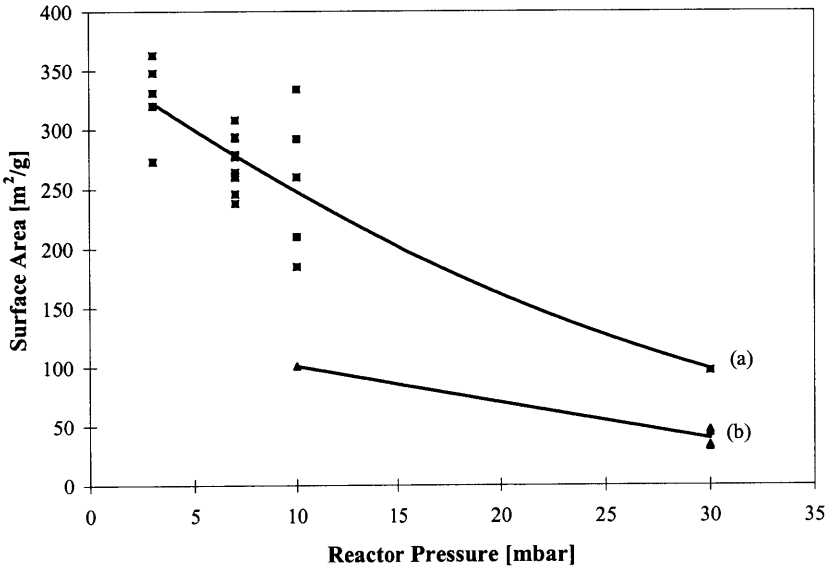

Figure 4-6. Surface areas of AlN produced at various reactor pressures with (a) helium and (b) nitrogen as the carrier gas. The variability in the data at a given pressure was due to differences in the gas velocity used (see Section 4.2.2).

4.2.2 Effect of Gas Velocity

The effect of gas velocity on crystallite size and surface area was not as clear as the effect of reactor pressure. At the lower pressures (e.g. 3 mbar), changes in gas velocity did not affect the powder characteristics significantly, as seen by the small scatter in the crystallite sizes and surface areas shown in Figures 4-5 and 4-6. However, at higher pressures (e.g. 10 mbar), there was an inverse correlation between surface area and gas velocity as shown in Figure 4-7. This was somewhat unexpected, since higher gas velocities should quench the particles more rapidly, reduce the concentration of particles above the melt, and remove the particles from the growth zone more rapidly, all of which should have reduced the crystallite size and increased the surface area. In this reactor, however, the more rapid flow might have increased the average crystallite size through two mechanisms. One possible mechanism was that the gas flow over the crucible might have become more turbulent as the gas velocity was increased. This would result in an increased residence time for the particles within the hot growth zone, producing larger crystallites. The second possible mechanism was that size-selective transport of the particles was taking place at the high reactor pressures. This would mean that while only the finest particles made it to the filter at lower gas velocities, as the gas velocity was increased, larger particles could be carried to the collection filter, thus increasing the volume-averaged crystallite size (as determined by Scherrer's method). Further investigation to support or refute these hypotheses would be difficult with this reactor because of the variation in the system, due primarily to fluctuations in the aluminum evaporation rate and changes in the crucible temperature.

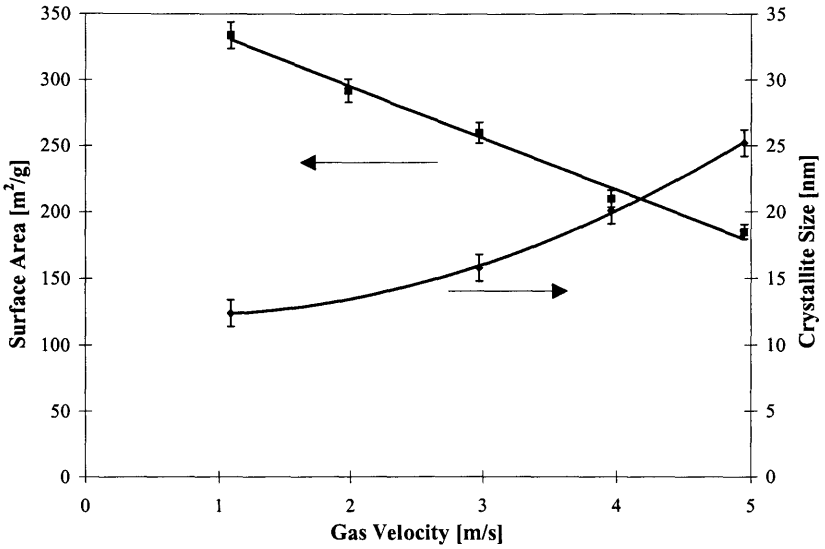

Figure 4-7. Surface areas and crystallite sizes of AlN powders produced with a He/NH_3 gas mixture at 10 mbar under different gas velocities.

Based upon the powder characterization data and the feedback from sintering experiments, the standard operating conditions listed in Table 4-1 were adopted. The 30 mbar operating pressure was chosen because (a) the gradually increasing pressure drop across the filter has less of an effect on run uniformity at high pressures, (b) the reactor yield tended to drop significantly at higher pressures, and (c) the sinterability of the powders decreased when they were synthesized at lower pressures. To achieve fully nitrided nanocrystalline AlN, the ammonia concentration was kept at 27 vol% and the total gas flow rate was maintained at 3.2 slpm; higher ammonia concentrations or gas flow rates would result in lower yields and coarser powders.

4.3 Particle Characterization

4.3.1 Electron Microscopy

Transmission electron micrographs of AlN particles produced in the forced-flow reactor are shown in Figures 4-8 and 4-9. High-resolution TEM confirmed that the particles were generally a single crystal without any obvious internal defects. The particles produced

via in-situ nitridation, and particularly at low pressures with helium as the carrier gas, contained as many as three morphologies: spheres, needles, and plates (Figure 4-8). A very large fraction of the particles produce in a He/NH_3 gas mixture were elongated particles. These needles generally had an aspect ratio between 3 and 10, whereas the plate-like particles had a hexagonal morphology and were only ~10 nm thick and 10-35 nm wide. Despite the presence of needle- and plate-like particles, X-ray diffraction patterns of the powders (Figure 4-4(c)) did not show any preferential growth direction. Particles produced in the N_2/NH_3 gas stream (Figure 4-9(a) and (b)) were significantly larger and generally more equiaxed with substantially fewer needle-shaped particles present than those produced in the He/NH_3 gas stream (Figure 4-9(c) and (d)).

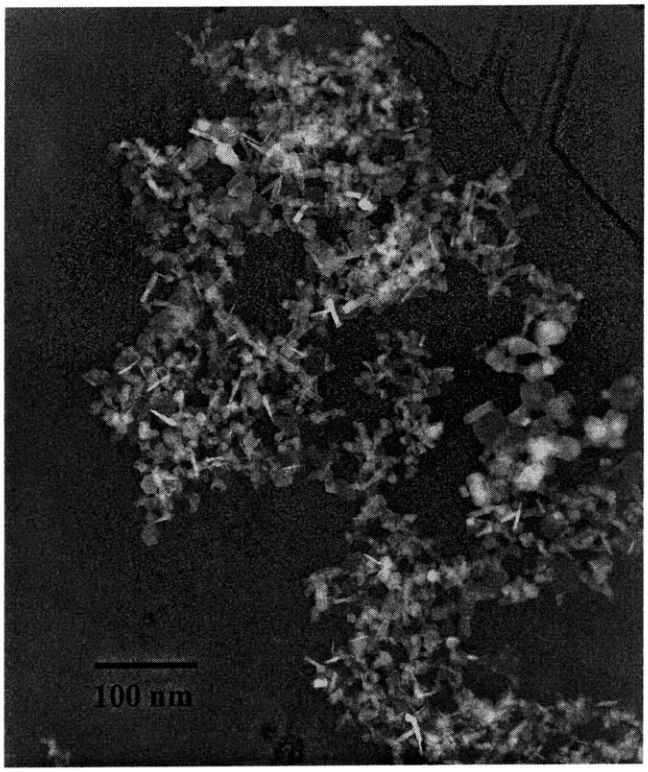

Figure 4-8. TEM micrograph of nanocrystalline AlN produced at 7 mbar in a 2.3-slpm gas stream with 27 vol% NH_3 and 73 vol% He.

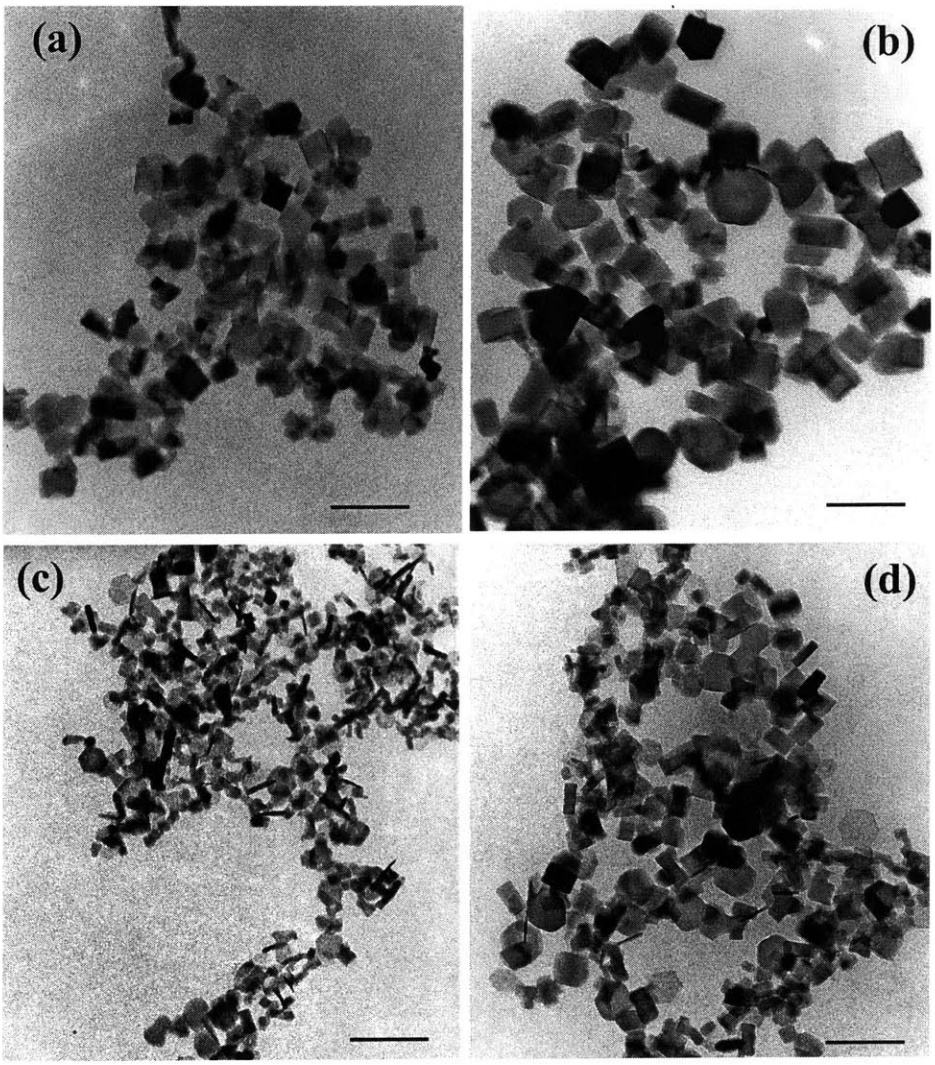

Figure 4-9. Transmission electron micrographs of nanocrystalline AlN powders synthesized in the forced-flow reactor via in-situ nitridation with NH_3. The powders were produced with (a,b) nitrogen or (c,d) helium as the carrier gas. The reactor pressure was 20 mbar for samples (a) and (c), and 30 mbar for samples (b) and (d). The scale bar is 100 nm.

High-resolution TEM micrographs of nanocrystalline AlN powder (produced by in-situ nitridation) and commercial AlN powder (Alfa Aesar) are shown in Figure 4-10. The commercial AlN powder had a relatively thick amorphous surface layer (see arrows marked in Figure 4-10(b)), which was probably AlOOH or Al_2O_3 produced from exposure to the atmosphere. The nanocrystalline AlN powder, however, did not have any visible surface

contamination and displayed continuous crystal lattices to the edges of the particles (Figure 4-10(a)). In addition, the nanocrystalline AlN particles did not contain any of the defect structures associated with high concentrations (>0.75 wt%) of oxygen within the grains. This suggested that any oxygen present in nanocrystalline AlN would be due to surface contamination.

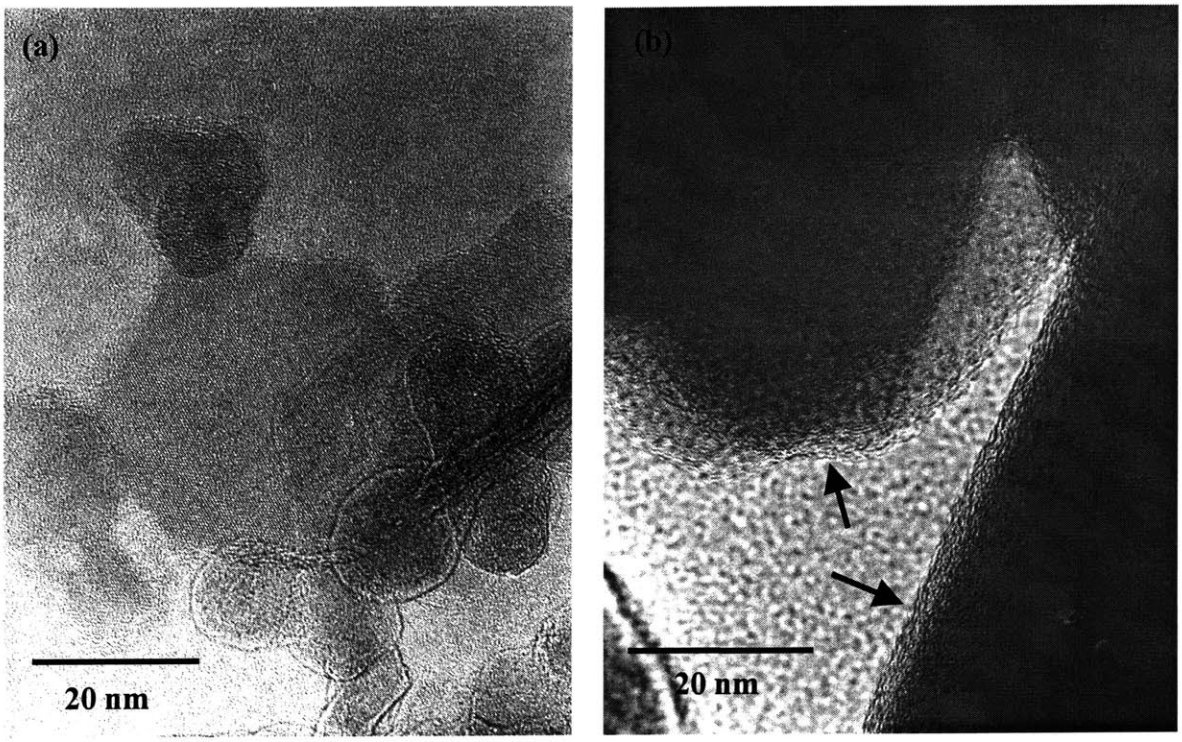

Figure 4-10. High-resolution TEM micrographs of (a) nanocrystalline and (b) commercial AlN powders.

4.3.2 Chemical Analysis

Nanocrystalline AlN powders produced via in-situ nitridation with NH_3 were sent to Element Analysis Corporation (Lexington, Kentucky) for determination of oxygen content by fast neutron activation analysis (FNAA). The oxygen content in the as-synthesized, high surface area powder was 3 wt%, which was higher than ideal, but is significantly lower than

that obtained by other researchers [4-6]. Although other researchers have produced nanocrystalline AlN, they have been unable to sufficiently protect it from hydrolysis after synthesis. The surface area, particle size, and oxygen content of AlN powders produced by various groups are compared in Table 4-2. Although the nanocrystalline AlN powder produced via aluminum evaporation and in-situ nitridation with our forced-flow reactor possessed one of the highest surface areas, it had the lowest oxygen content of the nanocrystalline AlN powders reported. This suggested that the precautions taken here during powder synthesis and handling effectively reduced the oxygen contamination. In fact, the oxygen content reported was probably an upper bound for this process due to the fact that the nanocrystalline AlN powder had to be exposed to air briefly by Element Analysis Corporation prior to sample analysis.

Table 4-2. Comparison of commercial and nanocrystalline AlN powders.

Surface Area (m^2/g)	Particle Size (nm)	Oxygen Content (wt%)	Synthesis Method	Reference
2.5	3660	1.2	Carbothermal Nitridation	H. C. Starck, Inc. [3]
30	60	5	RF Plasma	Baba *et al.* [4]
100	23	12	Transferred Arc	Moura and Munza[5]
220-260	8	11	RF Plasma	Canteloup and Mocellin [6]
250	16	3	Evaporation and In-situ Nitridation	This Work

4.3.3 Surface analysis

In order to examine the surface chemistry of nanocrystalline AlN, photoacoustic Fourier-transform infrared (PA-FTIR) spectra of the powders were obtained using a Bio-Rad FTS-60A/896 spectrometer with a MTEC Model 200 photoacoustic cell (Figure 4-11). Data were collected at a scan speed of 5 kHz for wavenumbers of 400-4000 cm^{-1} at a

resolution of 4 cm^{-1}. The PA-FTIR spectra shown in Figure 4-11 were collected for powders that had been unexposed, or had been exposed for various periods to the air in the laboratory environment. For Figure 4-11(a), the powder was loaded into the photoacoustic cell and sealed within a glovebox, and analyzed shortly thereafter to avoid exposure to the atmosphere. This spectrum was very similar to that reported by Merle-Méjean *et al.* for AlN that had been in-situ heated to 500°C under vacuum prior to analysis [7]. The experimental mode that Merle-Méjean *et al.* used (transmission FTIR) precluded analysis below 1000 cm^{-1} due to strong phonon vibrations, so that we could not compare the lattice vibrations of our samples to their system. For the unexposed powder, the doublet band at 725 and 840 cm^{-1} was due to Al-N lattice vibrations, and the small peak at 1560 cm^{-1} was assigned to NH_2 vibrations [7]. The sharp peaks at 2010 and 2085 cm^{-1} were probably due to adsorbed CN or HCN, which could be formed in low concentrations when the hot graphite crucible reacted with the ammonia gas in the forced-flow reactor. The minor peaks at 2160 and 2260 cm^{-1} were reportedly due to Al-H bonds within the AlN and on the AlN surface, respectively [7]. The broad band centered at 3200 cm^{-1} was attributed to NH surface species. There appeared to be a small amount of OH species on the unexposed sample as shown by the small peak at 3740 cm^{-1} [7].

As the sample underwent hydrolysis during exposure to air, a number of peaks disappeared and some additional peaks (primarily those associated with OH) emerged. After only 5 minutes of exposure to the atmosphere, the peaks at 2010 and 2085 cm^{-1} were reduced significantly as the CN or HCN species desorbed or reacted with water in the environment (Figure 4-11(b)). The broad band of physisorbed or weakly chemisorbed water at 3400 cm^{-1} [7] also developed with exposure to air. In addition, the Al-N lattice vibrations lost some intensity as water reacted with the powder and consumed the surface nitride. The broadening of the phonon bands and the appearance of a shoulder at 550 cm^{-1} were attributed to Al-O lattice vibrations [8] as the AlN surface was converted to AlOOH. The NH_2 peak at 1560 cm^{-1} became dominated by the water bending mode at 1645 cm^{-1} and the $CO_3^{=}$ vibrations at 1395 and 1530 cm^{-1} [8].

It was evident that even a 5-minute exposure, such as a sample might experience during removal from a powder collection device or in loading into a furnace, could have a large effect on the surface chemistry of these nanocrystalline powders. The PA-FTIR study highlighted the importance of maintaining an oxygen-free and moisture-free environment during the synthesis and processing of nanocrystalline AlN. The processing and handling procedures that were used to minimize oxygen and moisture contamination prior to and during sintering are discussed in Chapter 5.

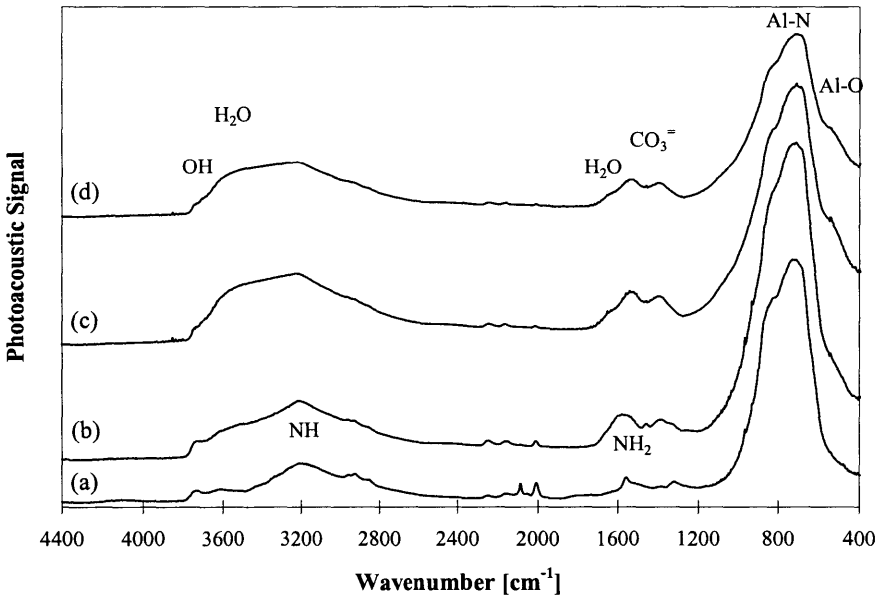

Figure 4-11. PA-FTIR spectra of nanocrystalline AlN powders (a) before exposure, and after (b) 5 minutes, (c) 12 hours, and (d) 18 hours of exposure to laboratory air.

4.4 Conclusions

Nanocrystalline AlN was successfully synthesized through the use of a forced-flow reactor. The effects of several reactor variables on the resulting powder morphology, surface area, purity, and yield were investigated and described. In most cases, the variables investigated had the expected effect. For example, lower reactor pressures resulted in smaller crystallite sizes and higher surface areas, the microwave-generated plasma

increased the degree of nitridation attainable when nitrogen was used as the nitriding gas, and NH_3 readily reacted with the Al vapors allowing high-purity AlN powders to be produced. However, in several instances the reactor variables had unexpected results. For instance, the choice of carrier gas during in-situ nitridation synthesis had a profound effect on the morphology of the particles produced. By understanding the effects of synthesis conditions and developing air-free powder processing, nanocrystalline AlN materials with high surface areas and low oxygen contents were achieved. The surface chemistry of these powders was examined, and it was shown that even a brief exposure to ambient atmosphere would lead to surface hydrolysis and oxidation of the AlN nanocrystals.

4.5 References

[1] D. T. Castro, *Synthesis, Processing, and Properties of Nanocrystalline Nitrides*, Sc.D. Thesis. Massachusetts Institute of Technology, Cambridge, MA, 1997.

[2] R. Flagan, "Gas Phase Synthesis of Nanoparticles"; pp. 15-30 in *Nanostructured Materials*. Edited by G.-M. Chow and N. Noskova. Kluwer Academic Publishers, Dordrecht, The Netherlands, 1998.

[3] H. C. Starck, Inc., Grade B AlN data sheet.

[4] K. Baba, N. Shohata, and M. Yonezawa, "Synthesis and Properties of Ultrafine AlN Powder by RF Plasma," *Appl. Phys. Lett.*, **54** [23] 2309-11 (1989).

[5] F. J. Moura and R. J. Munz, "Vapor-Phase Synthesis of Nanosize Aluminum Nitride Particles Using a Two-Stage Transferred Arc Reactor," *J. Am. Ceram. Soc.*, **80** [9] 2425-28 (1997).

[6] J. Canteloup and A. Mocellin, "Synthesis of Ultrafine Nitrides and Oxynitrides in an R.F. Plasma," *Proceedings of the Sixth Symposium on Special Ceramics*. Edited by P. Popper. British Ceramic Society, Stoke-on-Trent, U.K., 1975.

[7] T. Merle-Méjean, M.-I. Baraton, P. Quintard, Y. Laurent, and V. Lorenzelli, "Fourier-transform Infrared Characterization of an Aluminum Nitride Surface," *J. Chem. Soc. Faraday Trans.*, **89** [16] 3111-15 (1993).

[8] J. B. Benziger, S. J. McGovern, and B. S. H. Royce, "IR Photoacoustic Spectroscopy of Silica and Aluminum Oxide"; pp. 448-63 in *Catalyst Characterization Science*, ACS Symposium Series No. 288. Edited by M. L. Deviney and J. L. Gland. American Chemical Society, Washington, D.C., 1985.

5. Densification and Characterization of Aluminum Nitride

The purpose of synthesizing nanocrystalline AlN was to produce a powder that would allow pressureless and additive-free densification at relatively low temperatures; this would produce a material with a potentially high thermal conductivity for electronic packaging applications. Since nanocrystalline AlN powders were very hygroscopic, the samples were removed from the filter assembly, stored, and processed within a glovebox where the oxygen concentration was <5 ppm (generally <1 ppm) and the water concentration was maintained at <1 ppm. A large number of synthesis-processing-sintering experiments were conducted in order to determine which variables affected powder sinterability. Several of the early challenges were associated with purity and engineering issues. For example, a "high-purity" BN spray that had been used as a die lubricant was found to contain several weight percent of clay as a binder. AlN and BN powders that had been employed as packing powders to prevent AlN sublimation and carbon contamination during sintering were found to contain several weight percent oxygen. There had also been a problem with the molybdenum-sheathed thermocouples in the nitrogen-purged graphite furnace failing regularly at sintering temperatures above 1700°C. Having addressed these issues, interesting correlations between the synthesis conditions and the powder sinterability were unraveled. High-purity AlN powders were reproducibly synthesized and successfully sintered to give high thermal conductivities. Furthermore, some intriguing potential applications of these nanocrystalline AlN powders were discovered as bulk textured piezoelectric materials.

5.1 Pressureless Densification

Samples were prepared for pressureless densification by combining several batches of powder, passing them through a 325-mesh sieve (to improve mixing), and pressing them into a pellet within a glovebox using a BN-lubricated stainless steel die at ~1000 psi. The pellets were then placed in latex bags, evacuated, sealed, and removed from the glovebox to be cold isostatically pressed at 410 MPa. While still sealed, the samples were returned to

the glovebox, removed from the latex bag, and placed inside a high-purity BN casket with commercial AlN (H. C. Starck, Grade B) as a packing powder. The BN casket was then placed in a covered molybdenum crucible and sealed with Parafilm®. This tightly sealed casket was then rapidly transferred to the graphite furnace where it was immediately evacuated to $<2x10^{-2}$ mbar and refilled with 99.999% pure nitrogen three times prior to heating. The vacuum was maintained during the heating ramp until approximately 1000°C, when the furnace was filled to 4 psig and purged (0.4 slpm) with high-purity nitrogen. The standard heating cycle included a ramp of 10°C/min to the sintering temperature, followed by a 2-hour soak. The sample and furnace were then allowed to cool fairly rapidly (~50°C/min) back to room temperature.

5.1.1 Effect of Synthesis Conditions

One unexpected result of this study was the effect of carrier gas on crystallite size and surface area, as described in Section 4.2.1. Not surprisingly, however, the effect of carrier gas was also manifested in the sinterability of the powders produced. Figure 5-1 shows the large effect that synthesis conditions had on the densification of the resulting powders. The samples were made from powders produced with the two different carrier gases (He or N_2) and at various reactor pressures, under otherwise similar reactor conditions. The samples with the higher densities were made from powders synthesized with nitrogen as the carrier gas. This was not initially expected as these powders have a larger crystallite size and a lower surface area, thus presumably, a lower driving force for sintering. However, the aspect ratio of the particles, the particle size distribution, and the strength of the agglomerates within a powder can dominate the sinterability. As described in Section 4.3.1, the powders produced with He as the carrier gas consisted of smaller crystallites but with many more needle-shaped particles that might be detrimental toward packing and sintering. Another possible reason for the differences in densification behavior could be incomplete nitridation of the nanocrystalline AlN when synthesized with helium as the carrier gas. However, there were several arguments to refute this: (a) these powders were white - any residual aluminum would have made the powders darker in color, (b) X-

ray diffraction showed no residual aluminum in these samples, and (c) chemical analysis actually indicated a slight excess of nitrogen in these AlN powders. Presumably then, the nitridation of aluminum clusters (or the growth of AlN from the vapor phase) was sufficiently affected by the different carrier gases that the particle morphology was changed, thereby altering the sinterability of the powders drastically, despite the fact that the powders in both cases were pure AlN.

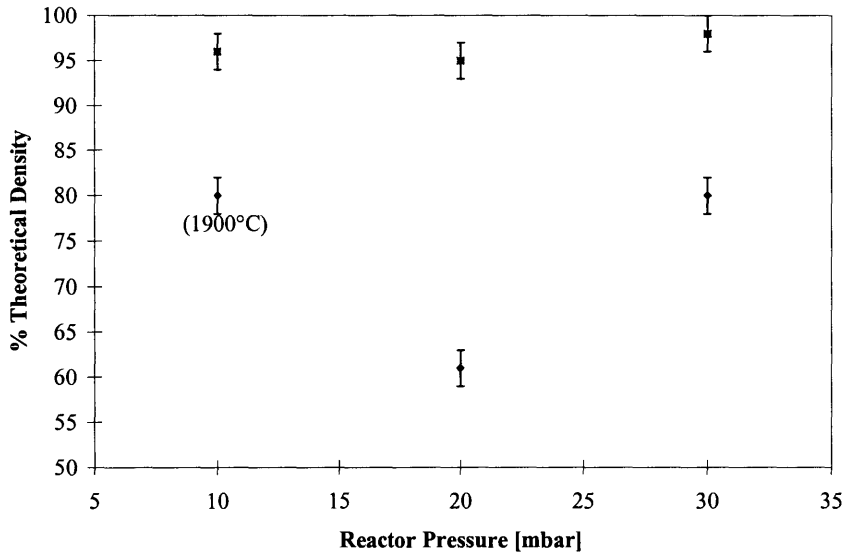

Figure 5-1. Effects of carrier gas and reactor pressure on the sinterability of nanocrystalline AlN powders. The carrier gas for in-situ nitridation synthesis was either (■) nitrogen or (◆) helium. All samples were pressurelessly sintered for two hours at 1700°C, unless otherwise indicated.

5.1.2 Additive-free Sintering

Since the nanocrystalline AlN synthesized with nitrogen as the carrier gas gave the best densification results, the powders used in subsequent sintering experiments were synthesized with nitrogen as the carrier gas at the standard reactor operating conditions given in Table 4-1. This resulted in pure AlN powders with a crystallite size of 80-100 nm and surface areas of 40-50 m^2/g. The additive-free sintering curve for the nanocrystalline

AlN powder created in the forced-flow reactor is shown in Figure 5-2, along with that of a commercial AlN powder (H. C. Starck, Grade B) and the best sintering results available in the literature (Hashimoto *et al.* [1]). Our nanocrystalline material densified much more readily than the H. C. Starck AlN powder (3.6 μm), achieving >95% of theoretical density by 1700°C. Interestingly, the sintering curve of our nanocrystalline AlN powder followed closely with that of Hashimoto *et al.*'s sample. Hashimoto *et al.* produced their powder by carbothermal nitridation of a mixture of basic aluminum chloride (BAC) and glucose. By carefully controlling the BAC:glucose ratio and the nitridation conditions, and using several post-synthesis oxidation and nitridation steps to remove the residual carbon and reduce the oxygen content, they were able to produce a sinterable powder with a moderate surface area (16 m^2/g) and a low oxygen content (1-2 wt%). The sintering results obtained with our nanocrystalline powder and Hashimoto *et al.*'s powder were both excellent considering that even the best commercially available AlN powders would require several hours at 1900°C to obtain >95% of theoretical density in additive-free sintering.

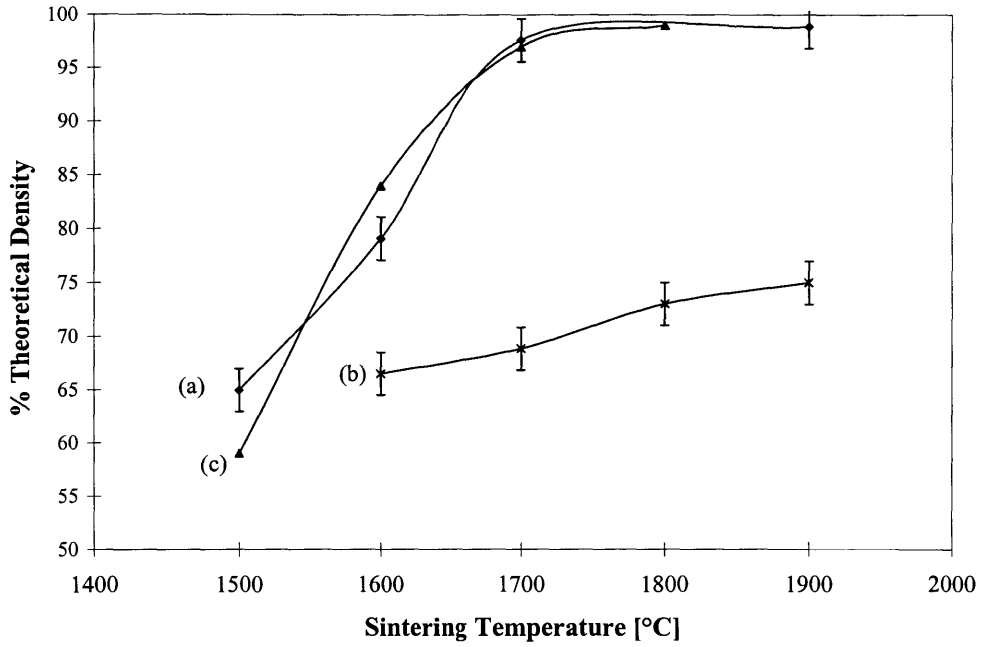

Figure 5-2. Pressureless, additive-free sintering curves of (a) nanocrystalline AlN (surface area = 44 m^2/g), (b) H. C. Starck Grade B AlN, and (c) Hashimoto *et al.*'s AlN (data from [1]). The samples were soaked at the sintering temperatures for 2 hours in (a) and (b), and for 3 hours in (c).

X-ray diffraction patterns for the nanocrystalline and H. C. Starck AlN samples sintered at 1900°C are shown in Figure 5-3. All peaks present corresponded to AlN. The fact that no secondary phases were detected suggested that either the oxygen content of these samples was below the solubility limit for oxygen in AlN, or the secondary phases were present at very low levels. Several authors have attempted to correlate the oxygen contents with crystallographic cell parameters. However, since the method of defect incorporation changes depending on the oxygen level, the cell parameters go through a maxima making oxygen determination via X-ray diffraction very difficult. Therefore, instead of XRD analysis, the sintered samples were sent out for fast neutron activation analysis to determine the oxygen content. These results are discussed in Section 5.2, along with the thermal conductivity results.

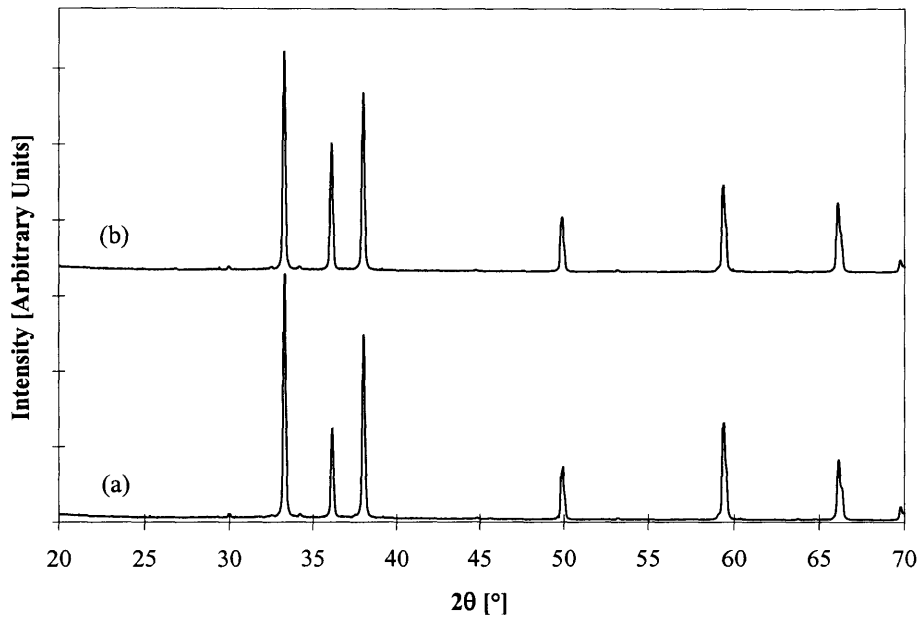

Figure 5-3. X-ray diffraction patterns of (a) nanocrystalline AlN and (b) H. C. Starck Grade B AlN after pressureless, additive-free sintering at 1900°C for 2 hours.

Scanning electron micrographs of the fracture surfaces of AlN pellets after sintering at 1600°C, 1700°C and 1900°C for two hours are shown in Figure 5-4. Samples were fractured, coated with gold, and examined using a JEOL 6320FV field emission gun scanning electron microscope. It was noted that the densification of nanocrystalline powders (Figures 5-4(a) and (b)) was superior to that of the commercial microcrystalline powders (Figure 5-4(c)). The grain growth of the nanocrystalline AlN was quite rapid so that when >90% of the theoretical density was attained, the grain size was on the order of 2-3 microns. The final grains were over 20 times larger than the initial grain size (<100 nm). Therefore, over 99.98 vol% of the AlN had crossed a grain boundary and been consumed by a growing grain during sintering. In contrast, the commercial AlN would have to grow to a final grain size of ~50 μm to achieve the same degree of material transport. Although this might be possible, the long diffusional paths and relatively slow diffusion rates meant that achieving a grain size of ~50 μm would take a very long time at high temperatures. This

result suggested that if oxygen has to be at a grain boundary in order to be removed (by either an additive or a highly reducing atmosphere), then nanocrystalline AlN would have an important advantage in rapid processing of ceramics with low lattice oxygen contents.

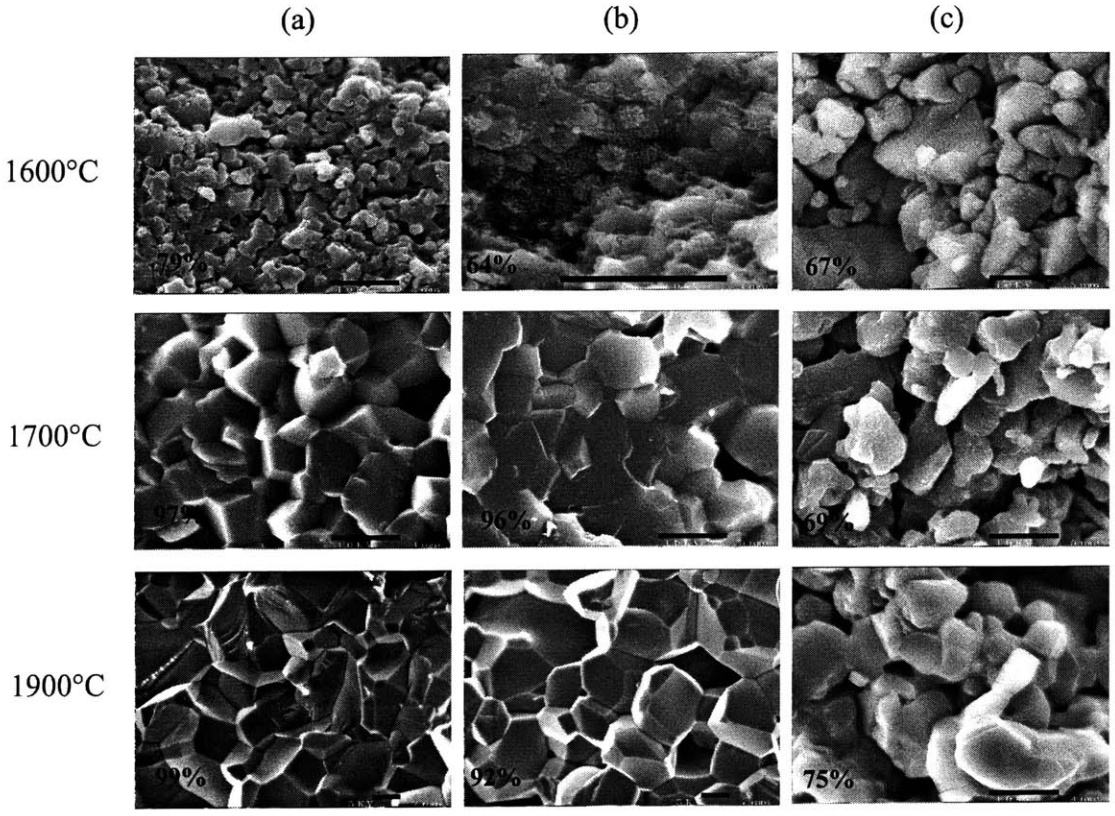

Figure 5-4. SEM micrographs of fracture surfaces for AlN pellets pressurelessly sintered for 2 hours at the given temperature. Samples were prepared from (a) nanocrystalline AlN synthesized at 30 mbar, (b) nanocrystalline AlN synthesized at 10 mbar, and (c) commercial H. C. Starck Grade B AlN. The scale bar represents 1 μm; the % theoretical density attained during additive-free sintering of the samples is noted in the lower left corner of each micrograph.

5.1.3 Effect of Y_2O_3 Additions

In order to examine the effect of sintering aids, 4 wt% of a micron-sized Y_2O_3 powder was added to the nanocrystalline AlN and the H. C. Starck Grade B AlN powders. The samples were then formed into pellets, isostatically pressed at 410 MPa, and heated at 10°C/min to

the sintering temperature where they were soaked for two hours. The densities of these samples were determined by Archimedes' method and are shown in Figure 5-5. The theoretical density for AlN samples with 4 wt% Y_2O_3 (incorporated as $Y_3Al_5O_{12}$) was calculated to be 3.33 g/cm^3, although this value would change slightly depending on which yttrium aluminate phases were present and their relative amounts. The sintering curves shown in Figure 5-5 are for (a) the best sintering results reported in the literature (Hashimoto *et al.* [1], AlN with 2 wt% Y_2O_3, 3-hour dwell), (b) nanocrystalline AlN with 4 wt% Y_2O_3, (c) H. C. Starck Grade B AlN with 4 wt% Y_2O_3, and (d) H. C. Starck Grade B AlN without any additive. The Y_2O_3 additives have a large effect on the densification of both the nanocrystalline and commercial AlN powders. Whereas the pure commercial material did not exceed 75% of theoretical density even after sintering at 1900°C, it attained >90% of theoretical density at 1800°C with 4 wt% Y_2O_3 additives. The large increase in densification for the commercial AlN with the Y_2O_3 additions at temperatures between 1700° and 1800° was due to the well-known formation of a liquid phase in the Y_2O_3-Al_2O_3 system at temperatures around 1760°C. This liquid phase greatly increased material transport and enhanced densification. However, there was also an increase in density for the nanocrystalline sample at temperatures well below 1700°C. The addition of yttria to the nanocrystalline AlN increased the density attained at 1600°C from 78% to 93%; Hashimoto *et al.* [1] found that the temperature required to achieve >95% of theoretical density could be reduced by 100°C (to 1600°C) with the addition of 2 wt% Y_2O_3. There were two likely mechanisms for the increased low-temperature densification of ultrafine AlN systems with Y_2O_3 additions: (a) an Al-Y-O-N liquid could form and promote material transport via liquid-phase sintering, or (b) solid-state grain boundary diffusion could increase due to Y_2O_3 doping of the grain boundaries. It is well accepted that a ternary liquid (Al_2O_3-Y_2O_3-AlN) can be present at temperatures >1700°C [2], but these results suggest that a liquid phase may form at even lower temperatures (<1600°C) or that Y_2O_3 doping significantly increases solid-state diffusion.

Although the pure AlN samples prepared in this work and by Hashimoto *et al.* [1] have similar sintering behaviors (Figures 5-2(a) and (c)), the AlN sample prepared by Hashimoto *et al.* benefited more from the Y_2O_3 sintering additive. There were two possible reasons for the latter observation. The first was that Hashimoto *et al.* [1] used an ultrafine, high surface area Y_2O_3 powder (57 m^2/g) as the additive, whereas the Y_2O_3 used in sintering nanocrystalline AlN (Figure 5-5(b)) was much coarser (~1 μm diameter, 8.7 m^2/g). This could lead to significant differences in the reactivity of the Y_2O_3 with the surface oxide and nitride species of the AlN. The second explanation involves the different amounts of Y_2O_3 that were added: 4 wt% Y_2O_3 was added to the nanocrystalline AlN sample while Hashimoto *et al.* [1] used 2 wt% Y_2O_3. There might exist an optimal concentration of Y_2O_3 additive depending on the crystallite size and/or oxygen content of the AlN sample. Other researchers have shown that there was an optimal additive content to maximize the thermal conductivity of AlN [3,4], and the amount necessary could be affected by both the oxygen content and the powder used. This concept might extend to the densification of AlN as well.

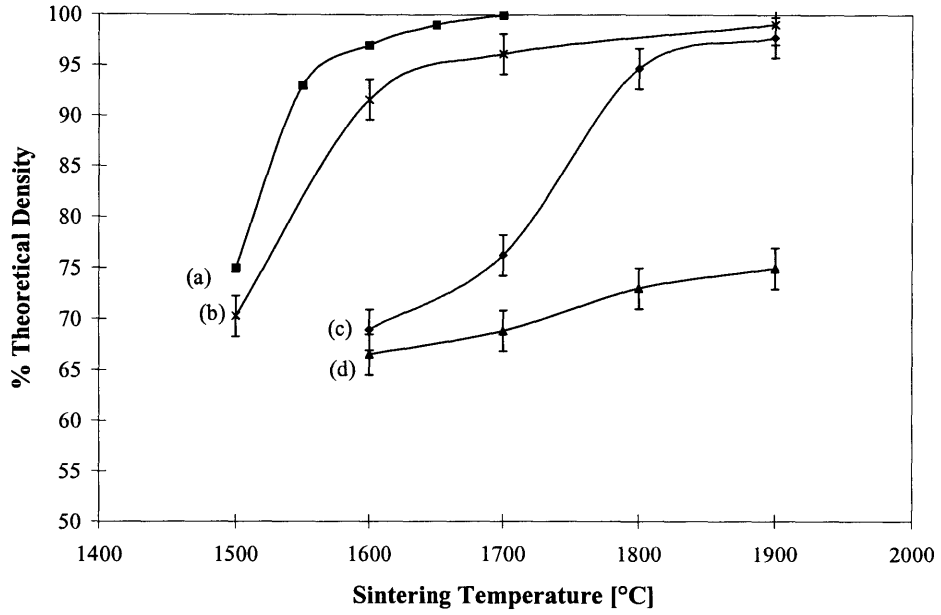

Figure 5-5. Pressureless sintering curves of (a) Hashimoto *et al.*'s AlN with 2 wt% Y_2O_3 (data from [1]), (b) nanocrystalline AlN with 4 wt% coarse-grained Y_2O_3, and H. C. Starck Grade B AlN with (c) 4 wt% coarse-grained Y_2O_3 or (d) no additive. The samples were soaked at the sintering temperatures for 3 hours in (a), and for 2 hours in (b)-(d).

In order to investigate these possibilities, an additional set of nanocrystalline AlN samples were sintered with 2 and 4 wt% nanocrystalline Y_2O_3 that had been synthesized by the method of Fokema and Ying [5] and had a surface area of 56.5 m^2/g. The resulting sintering curves are shown in Figure 5-6. The nanocrystalline Y_2O_3 additive with a high surface area enhanced the low-temperature densification of nanocrystalline AlN considerably (by ~6% of theoretical density at 1500°C), and the resulting sintering behaviors were similar to that of Hashimoto *et al.*'s sample for sintering temperatures ≤1550°C [1]. The different amounts of Y_2O_3 added did not appear to lead to different densification behaviors. Interestingly, although the nanocrystalline AlN samples attained ~95% density at 1550°C with nanocrystalline Y_2O_3 additives, they did not undergo substantially more densification above this temperature. Such sintering behavior might be

attributed to the presence of large residual pores. Shown in Figure 5-7 are optical micrographs of polished surfaces of nanocrystalline AlN samples densified (a) without additives and (b) with 2 wt% nanocrystalline Y_2O_3. Both samples had approximately the same density (95%) since the additive-free sample was sintered at 1700°C, while the sample with Y_2O_3 was sintered at 1650°C. The pore size distribution, however, was significantly different. While the sample without additives had uniform pores of only a few microns in size, the sample with the nanocrystalline Y_2O_3 additions had some pores as large as 40 μm. These pores were believed to be a result Y_2O_3 agglomerates that were not broken down during the relatively gentle hand-mixing process. With a less agglomerated, nanocrystalline Y_2O_3 powder, the densification would undoubtedly improve during the final stages of sintering. In spite of the Y_2O_3 agglomerates limiting the final densification of nanocrystalline AlN, the initial densification to 95% of theoretical density by 1550°C was impressive, as was the effect of changing the Y_2O_3 source to one containing finer particles.

One striking observation in comparing our sintering results to those of Hashimoto *et al.* [1] was the similarity in the densification behaviors of ultrafine, high-purity AlN powders that were synthesized and processed via very different methods. This similarity suggests that that (a) these two very different processes have produced high-quality powders of very similar characteristics, or (b) a lower temperature limit for densification of AlN has been approached. To investigate the latter possibility, we note that Sternitzke and Müller [6] and Solmon *et al.* [7] measured the oxygen-nitrogen interdiffusion coefficient for Y_2O_3-doped polycrystalline AlN at 1600°C to be ~$3x10^{-15}$ cm^2/s and ~$3x10^{-14}$ cm^2/s, respectively. Although the interdiffusion coefficients are not the most desired values to compare with densification studies, nitrogen is expected to be the slowest diffusing species so that oxygen-nitrogen interdiffusion values will give an order-of-magnitude estimate for the rate-limiting step in AlN sintering. Since the activation energies reported for diffusion in AlN is very large (240-430 kJ/mol), the diffusion coefficients will decrease rapidly with temperature, making sintering even more difficult. For example, assuming an activation energy of 300 kJ/mol, the interdiffusion coefficient will decrease by an order of magnitude

between 1600°C and 1400°C. At 1600°C, the oxygen-nitrogen interdiffusion coefficients are already ~4 orders of magnitude lower than the oxygen diffusion coefficient in Al_2O_3 [6]. Compared to Y_2O_3-doped AlN, pure AlN presumably has even lower diffusion rates given its lower sinterability. Therefore, to compensate for the decrease in diffusion rate with temperature, the particle size of the nanocrystalline AlN would have to decrease by another order of magnitude to further reduce the sintering temperature below 1550°C and 1700°C for Y_2O_3-doped and pure AlN systems.

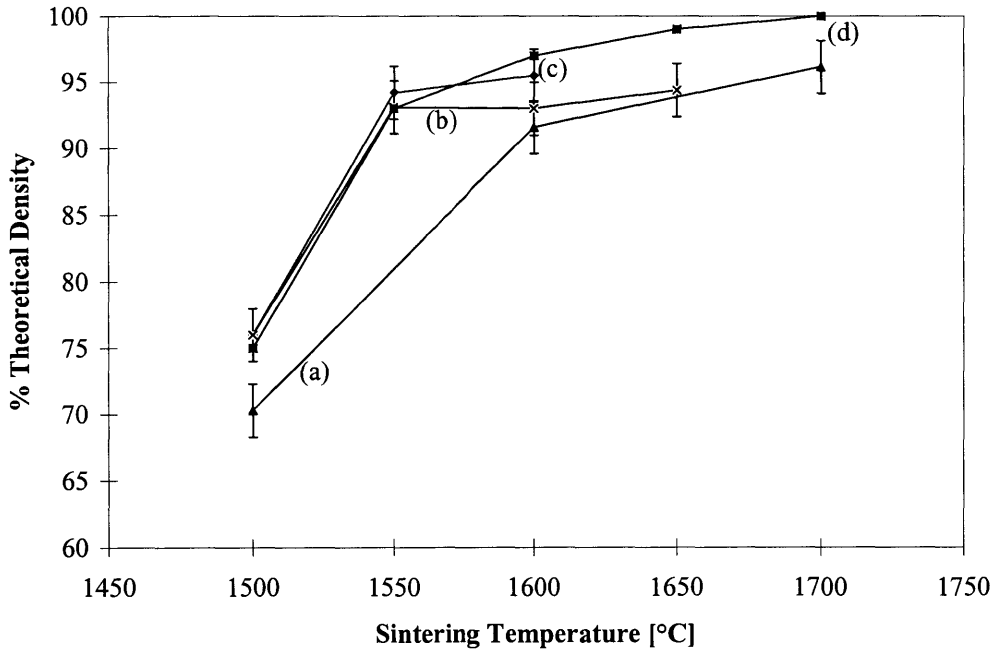

Figure 5-6. Sintering curves for nanocrystalline AlN with (a) 4 wt% micron-sized Y_2O_3, (b) 2 wt% nanocrystalline Y_2O_3, and (c) 4 wt% nanocrystalline Y_2O_3. Curve (d) represents the best sintering results reported in the literature (Hashimoto *et al.*'s AlN with 2 wt% high surface area Y_2O_3). The samples were soaked at the sintering temperatures for 2 hours in (a)-(c), and for 3 hours in (d).

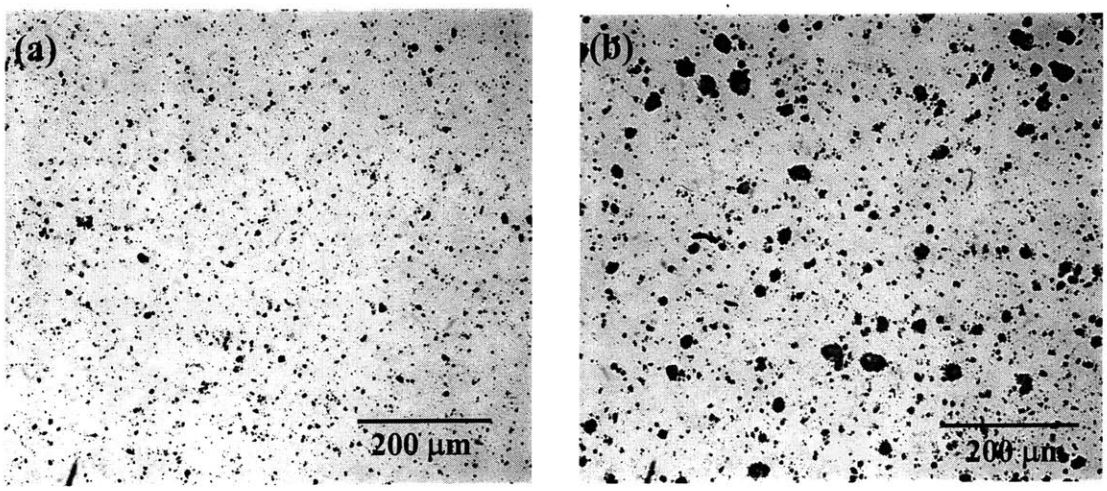

Figure 5-7. Polished cross-sections of nanocrystalline AlN samples sintered (a) without additives at 1700°C for 2 hours, and (b) with 2 wt% nanocrystalline Y_2O_3 at 1650°C for 2 hours.

X-ray diffraction patterns of the AlN pellets sintered at 1900°C with 4 wt% coarse-grained Y_2O_3 are shown in Figure 5-8. Both the nanocrystalline and commercial AlN samples sintered with Y_2O_3 contained secondary phases corresponding to yttrium aluminates, but the phases present were quite different. The commercial AlN sample had both $AlYO_3$ and $Al_5Y_3O_{12}$ as secondary phases, while the nanocrystalline AlN sample contained only $Al_2Y_4O_9$ as the secondary phase. The Al:Y ratios in the secondary phases of the commercial AlN sample were between 1 and 1.7, while that of the nanocrystalline AlN sample was only 0.5. This suggested that there was considerably less oxygen available in the nanocrystalline AlN sample for the Y_2O_3 to react with, so that a low Al_2O_3-containing phase was formed. Therefore, less Y_2O_3 additive might be needed to scavenge oxygen to acceptable levels for the more carefully processed, higher purity nanocrystalline AlN than for the commercial AlN. The secondary phases detected by XRD of nanocrystalline AlN pellets sintered with 2 wt% and 4 wt% nanocrystalline Y_2O_3 were $Al_5Y_3O_{12}$ and $Al_2Y_4O_9$, respectively. As a comparison, Hashimoto *et al.* [1] also found that $Al_5Y_3O_{12}$ was present as the secondary phase when only 2 wt% Y_2O_3 was added to their most sinterable, lowest oxygen-containing (2 wt%) AlN powders.

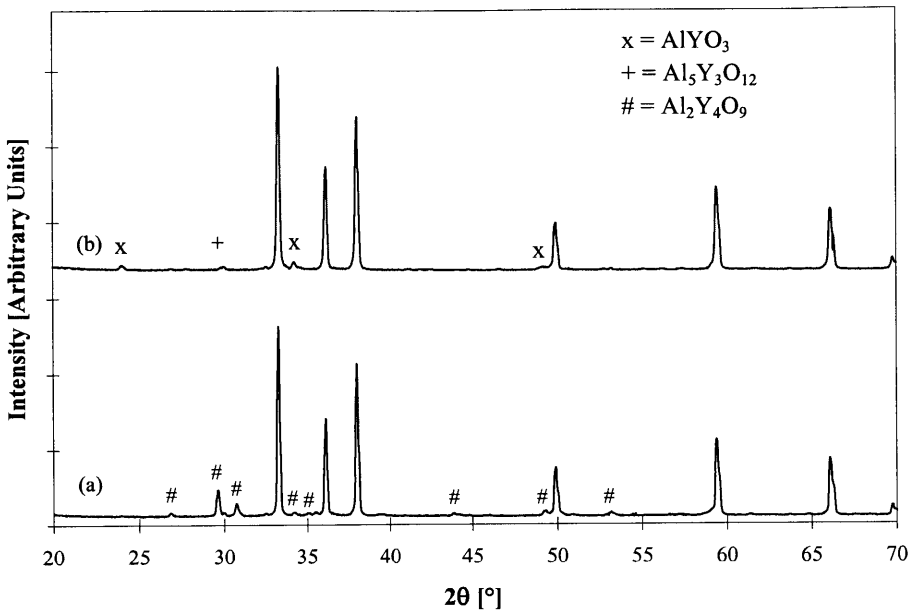

Figure 5-8. X-ray diffraction patterns of AlN pellets sintered at 1900°C for 2 hours with 4 wt% coarse-grained Y_2O_3. The AlN powders used were (a) nanocrystalline and (b) commercial (H. C. Starck Grade B AlN).

5.2 Thermal Conductivity Properties

The thermal conductivity of selected samples were determined by the laser flash thermal diffusivity method by Holometrix Corporation (Bedford, Massachusetts). The samples were machined into 1/2 inch-diameter disks of 1-2 mm thick, and polished until the faces were parallel. Coating of the samples with an optical absorbing layer was necessary to prevent transmission of the laser light, especially through the highly translucent specimens. The thermal conductivity K of a sample can be obtained from the thermal diffusivity α as follows,

$$K = \rho C_p \alpha \qquad \text{(Equation 5-1)}$$

where ρ is the density of the sample as determined by Archimedes' method and C_p is the specific heat. The samples examined had been pressurelessly sintered at 1900°C for 2 hours and were >98% dense to allow for direct comparison. The density, specific heat,

thermal diffusivity and the calculated thermal conductivity for three different samples are shown in Table 5-1.

Table 5-1. Laser flash thermal diffusivity results for AlN samples pressurelessly sintered at 1900°C for 2 hours. Y_2O_3 additives used were low surface area powders.

Sample	Density (g/cm^3)	Specific Heat (J/g·K)	Diffusivity (cm^2/s)	Conductivity (W/m·K)
Nano AlN, no additive	3.22	0.748	0.297	71.6
Nano AlN, 4 wt% Y_2O_3	3.30	0.730	0.615	148
H. C. Starck, 4 wt% Y_2O_3	3.26	0.714	0.664	155

These thermal diffusivity results corresponded very well with results of other researchers. The two parameters that most strongly affect the thermal conductivity of undoped AlN specimens are density and oxygen content. Enloe *et al.* [8] investigated the densification and thermal conductivity of five different microcrystalline AlN powders processed with and without additives. As shown in Figure 5-9, the powders without additives achieved only ~70% of theoretical density through pressureless sintering, and with the exception of a single sample, had a maximum thermal conductivity of only 45 W/m·K [8]. Only by hot pressing their powders at 1900°C under 20 MPa for 1 hour were densities and thermal conductivities comparable to those reported here (the pressurelessly sintered, undoped nanocrystalline AlN (shown as • in Figure 5-9)) obtained by Enloe *et al.* [8]. Hashimoto *et al.* [1], who has prepared an undoped AlN powder that sintered very similarly to our pure nanocrystalline powders, reported a thermal conductivity (68 W/m·K) nearly identical to that obtained here. The undoped sample prepared from H. C. Starck Grade B AlN powder was not sent out for thermal conductivity testing because it had too low a density (~73%) to merit further analysis. The oxygen content of the undoped, sintered sample prepared from nanocrystalline AlN was determined to be 0.6 wt% by FNAA. This oxygen content was considerably lower than that described earlier (Table 4-2) for nanocrystalline AlN powder that had been exposed briefly prior to analysis (3 wt% oxygen).

Since the sintered sample of undoped nanocrystalline AlN did not have any oxide sintering aids nor detectable secondary phases, it was assumed that the oxygen impurities resided within the AlN lattice. Buhr *et al.* [2] plotted the thermal conductivity vs. the oxygen content for various AlN samples, along with the correlation for single-phase AlN ceramics as reported by Slack [9]. Their plot showed that the highest thermal conductivity that could be expected for AlN containing 0.6 wt% oxygen was ~100 W/m·K.

The thermal conductivities of the 4 wt% Y_2O_3-doped nanocrystalline AlN (148 W/m·K) and H. C. Starck AlN (155 W/m·K) were very similar. This was expected since the formation of a liquid phase during sintering would overwhelm any differences in the starting powders. These results for the Y_2O_3-doped samples were not only self-consistent, but were also very similar to those obtained by other researchers under similar sintering conditions. Enloe *et al.* [8] found that AlN doped with Y_2O_3 and sintered to >98% dense possessed thermal conductivities ranging from 125 to 160 W/m·K, depending primarily upon the oxygen content of the powder used.

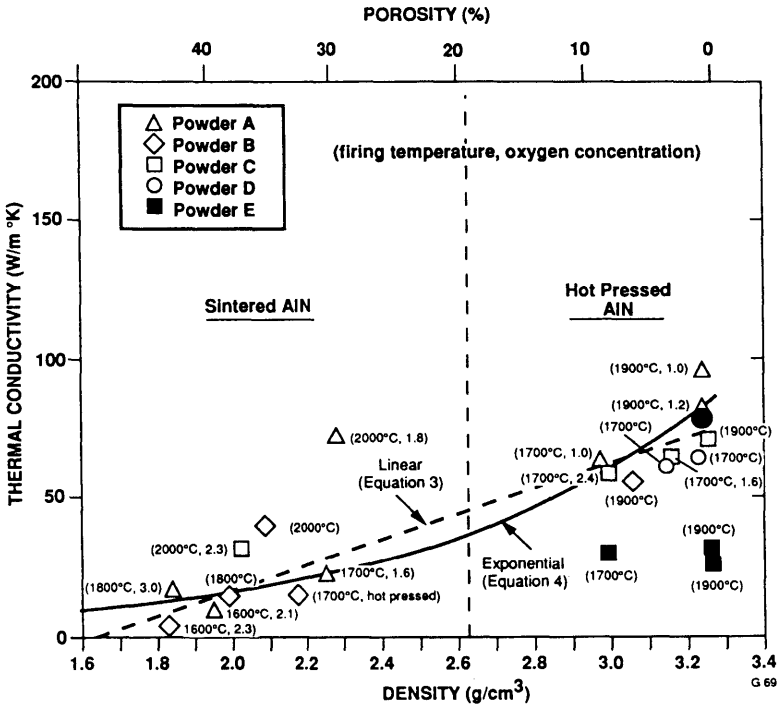

Figure 5-9. Thermal conductivity of additive-free, pressurelessly sintered nanocrystalline AlN from this research (•) compared to that of pressurelessly sintered and hot-pressed AlN (adapted from Enloe *et al.* [8]).

Higher thermal conductivities can be attained for both undoped and doped samples by annealing them at high temperatures and for long times in a highly reducing atmosphere. Hirano *et al.* [10], for example, reported a thermal conductivity of 114 W/m·K for an undoped AlN sample that had been sintered at 1900°C for 8 hours in a graphite furnace. Other researchers have found that the thermal conductivity of Y_2O_3-doped AlN could be increased to ~260 W/m·K through similar heat treatments [11,12]. By heating the sample in a highly reducing atmosphere, oxygen is removed from the AlN lattice and secondary phases are gradually vaporized, thereby increasing the purity, grain size, and thermal conductivity of the AlN material.

5.3 Hot Pressing

During the initial stage of the sintering studies experiments were focused on powders prepared in a He/NH_3 gas stream at low reactor pressures, which gave the highest surface area and smallest crystallite size possible for AlN. However, as shown in Figure 5-1, these powders did not densify well via pressureless sintering, so hot pressing was investigated as an alternative method for densification. Hot pressing was performed with a BN-coated ½ inch-diameter graphite die. The powders were loaded into the die and the rams inserted while inside a glovebox. The assembly was then rapidly transferred from the glovebox to a resistively heated graphite furnace (Materials Research Furnaces, Inc.), where it was quickly evacuated and purged three times with 99.999% pure nitrogen. Samples were then heated at 10°C/min to 1900°C in 4 psig N_2 (1 slpm purge) and soaked for 1 or 2 hours. As shown in Figure 5-10, densification of these nanocrystalline AlN powders was difficult even with hot pressing. Pressures of 50 to 100 MPa and temperatures of 1900°C were necessary to obtain densities >90%. This is in stark contrast to the powders generated at higher reactor pressures in a N_2/NH_3 atmosphere, which achieved >95% of theoretical density at temperatures as low as 1700°C during pressureless sintering (Figure 5-2). As discussed previously, the large difference in powder sinterability was believed to be due to the higher number of needle-shaped particles that were produced when the reactor was operated at lower pressures with a He/NH_3 gas stream.

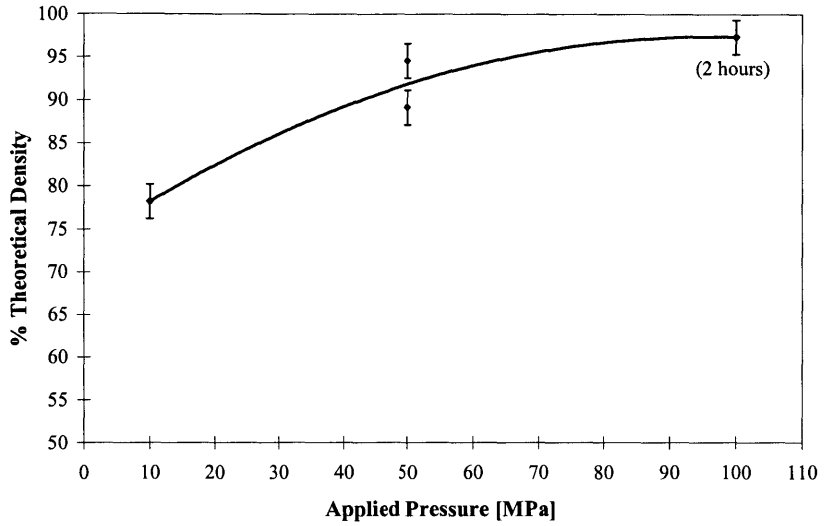

Figure 5-10. Densification of nanocrystalline AlN powder produced at 7 mbar in a He/NH_3 gas stream. The samples were hot pressed at 10°C/min with the applied pressure specified and held at 1900°C for 1 hour (except otherwise noted).

X-ray diffraction patterns of hot-pressed nanocrystalline AlN and commercial AlN are shown in Figure 5-11. The samples were hot pressed at 1900°C for 1 hour under 50 MPa. The extraordinarily intense (002) and (004) peaks of the nanocrystalline AlN sample in comparison to those of the commercial AlN sample (whose pattern matched the standard diffraction pattern of randomly distributed, uniform AlN crystals) suggested that the nanocrystalline sample was highly oriented.

AlN, besides having a high thermal conductivity, might also be useful as a high-temperature piezoelectric. Although the value of its piezoelectric constant d_{33} (5 pC/N) is not very high, it has been suggested that AlN can be used at higher temperatures (up to 1150°C) than many other piezoelectric materials [13]. The preferred orientation along the (002) direction achieved in pellets prepared by hot pressing nanocrystalline AlN powders containing large numbers of needle-shaped particles may be useful for piezoelectric applications. Although the degree of orientation attained in this case was low compared to that achieved with AlN thin film piezoelectrics prepared by CVD and RF sputtering

techniques [14-16], it was very high for bulk polycrystalline AlN samples. Sandlin *et al.* have attempted to attain preferred orientation in bulk AlN by using a seeding approach with SiC plates [17]. In this technique, they combined submicron AlN particles with readily available SiC plate-like particles. By slipcasting a mixture of these particles (with up to 30 vol% SiC), they were able to align the SiC platelets. The texturing of the SiC was then transferred to the surrounding AlN, and the samples were densified by hot pressing at 1800°C for 1 hour. The dense samples were then annealed for up to 18 hours at 2150°C to improve the degree of orientation. It was difficult to make a direct comparison of our results to those of Sandlin *et al.* [17], since they used neutron diffraction instead of X-ray diffraction to characterize their samples. However, while the relative (002) and (100) peak heights would be different for neutron vs. X-ray diffraction, an approximate correction factor could be determined by using one of the common diffraction pattern modeling programs. By entering the crystal structure and atomic positions for AlN, the X-ray derived thermal parameters, and the neutron wavelength used by Sandlin *et al.* into the freeware program PowderCell©, a neutron powder diffraction pattern was created. The estimated (002)/(100) peak ratio for untextured AlN was 0.75 and 0.63 for neutron diffraction and X-ray diffraction, respectively, which suggested that the X-ray peak ratio data should be multiplied by a factor of 1.2 to obtain data directly comparable to that of Sandlin *et al.* The highest (002)/(100) neutron diffraction peak ratio reported by Sandlin *et al.* was 4.8 after 18 hours of annealing at 2150°C. The hot-pressed sample derived from nanocrystalline AlN powder (Figure 5-11(a)) has a remarkably high (002)/(100) X-ray diffraction peak ratio of ~10.8, which would be ~13 when corrected to a neutron diffraction peak ratio. Interestingly, the powders that could be pressurelessly sintered easily (i.e. those produced at higher gas pressures and in a N_2/NH_3 gas stream) did not show any preferred alignment when hot pressed. The reason for the difference in texturing behavior is not clear, however, it may have been an effect of either (a) the large number of needle-like particles that may have influenced the packing of the plate-like particles or (b) the finer crystallite size of the powders produced at lower pressures and in a He/NH_3 gas stream. The smaller

crystallite size may have affected the texturing by allowing plastic deformation of the particles and texturing of the sample to occur during high-temperature densification under the applied load.

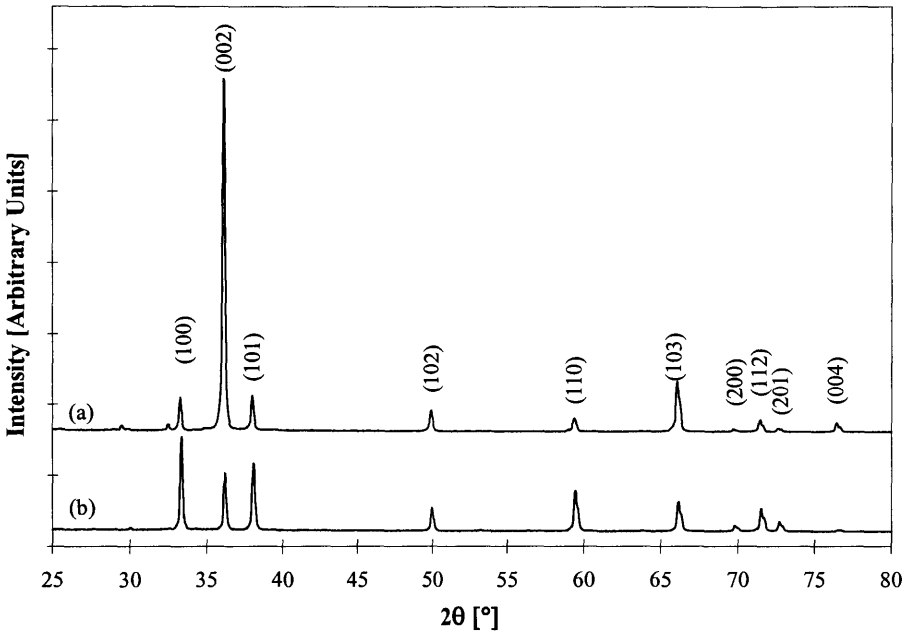

Figure 5-11. X-ray diffraction patterns of AlN pellets after hot pressing at 50 MPa and 1900°C for 1 hour. The powders used were (a) nanocrystalline AlN synthesized at 10 mbar in a He/NH_3 gas stream and (b) H. C. Starck Grade B AlN.

To further quantify the alignment and characterize the texturing that was obtained, pole figures of a textured sample and a standard AlN sample were created. The intensity of the (002) diffraction peak for each sample was measured and plotted versus rotational angle and tilt angle. The data showed that both the hot pressed nanocrystalline and reference AlN samples were radially symmetric about the compaction axis, so the results could be simplified by plotting the radial average of the (002) peak intensity as a function of the tilt angle. To further elucidate the degree of alignment in the hot-pressed nanocrystalline sample, a ratio of the (002) peak height of the textured nanocrystalline sample vs. that of the untextured standard was obtained (Figure 5-12). Due to the different densities of the

textured and standard AlN samples, a different number of planes would diffract, making a direct comparison of the X-ray counts incorrect. However, a ratio of their (002) peak intensities should give an accurate representation of the relative degree of orientation of the textured material. Figure 5-12 showed that a much larger fraction of the (002) diffraction intensity was observed for the textured sample at higher tilt angles than for the standard. These results confirmed that there was indeed a high degree of texturing along the (002) direction, and that the texturing was symmetrically oriented about the compaction axis. However, no electric response was detected from this sample when it was subjected to an applied load. Since, the crystals in these samples were not perfectly textured, the piezoelectric response was expected to be small. More samples would need to be examined and additional research is necessary to determine whether extended heat treatments can increase the degree of alignment as reported by Sandlin *et al.* for the SiC-seeded AlN system [17], and whether sufficient alignment can be introduced to make the textured bulk AlN attractive for piezoelectric devices.

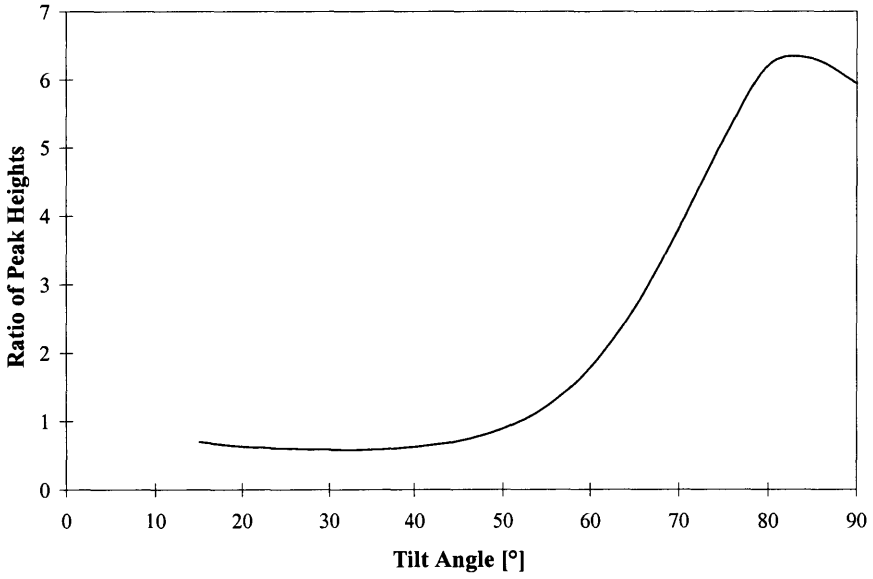

Figure 5-12. Ratio of the (002) XRD peak height in hot-pressed nanocrystalline AlN sample and that in an untextured AlN standard as a function of tilt angle.

5.4 Conclusions

The densification of the nanocrystalline AlN powders was evaluated as a function of the synthesis conditions, sintering additives, and dopant levels. The nanocrystalline AlN powders synthesized at low pressures in a He/NH_3 gas flow consisted of a large number of needle-shaped particles, which were difficult to densify without using pressure-assisted sintering. On the other hand, powders synthesized at 30 mbar in a N_2/NH_3 gas stream could be pressurelessly sintered without additive to >95% of theoretical density by 1700°C. Dopant effects were also examined, and it was found that for the nanocrystalline AlN powders, nanocrystalline Y_2O_3 powders promoted low-temperature densification more than microcrystalline Y_2O_3 dopants. Interestingly, nanocrystalline Y_2O_3 additives greatly increased the densification of nanocrystalline AlN at temperatures significantly lower than the expected onset of a bulk liquid phase. It was hypothesized that nanocrystalline Y_2O_3 acted as a grain boundary dopant and increased the diffusivity of the AlN, thereby enhancing densification. Thermal conductivities of the densified samples were obtained by laser flash thermal diffusivity measurements and, in the case of additive-free samples, were found to be comparable to the best results reported in the literature for similarly processed materials. The additive-free AlN samples attained a thermal conductivity of 72 W/m·K, while the 4 wt% Y_2O_3-doped AlN sample achieved a thermal conductivity of 148 W/m·K. An additional, very interesting result of this research was that the nanocrystalline powder synthesized in a He/NH_3 gas stream, which consisted of many needle-shaped particles, would produce a highly textured AlN material after hot pressing. This may be of interest for high-temperature piezoelectric sensing applications.

5.5 References

[1] N. Hashimoto, H. Yoden, and S. Deki, "Sintering Behavior of Fine Aluminum Nitride Powder Synthesized from Aluminum Polynuclear Complexes," *J. Am. Ceram. Soc.*, **75** [8] 2098-106 (1992).

[2] H. Buhr, G. Muller, H. Wiggers, F. Aldinger, P. Foley, and A. Roosen, "Phase Composition, Oxygen Content, and Thermal Conductivity of AlN(Y_2O_3) Ceramics," *J. Am. Ceram. Soc.*, **74** [4] 718-23 (1991).

[3] P. Sainz de Baranda, A. K. Knudsen, and E. Ruh, "Effect of Yttria on the Thermal Conductivity of Aluminum Nitride," *J. Am. Ceram. Soc.*, **77** [7] 1846-50 (1994).

[4] Y. Kurokawa, K. Utsumi, and H. Takamizawa, "Development and Microstructural Characterization of High-Thermal-Conductivity Aluminum Nitride Ceramics," *J. Am. Ceram. Soc.*, **71** [7] 588-94 (1988).

[5] M. D. Fokema and J. Y. Ying, "The Selective Catalytic Reduction of Nitric Oxide with Methane over Scandium Oxide, Yttrium Oxide and Lanthanum Oxide," *Appl. Catal. B: Environ.*, **18** [1-2] 71-77 (1998).

[6] M. Sternitzke and G. Müller, "EELS Study of Oxygen Diffusion in Aluminum Nitride," *J. Am. Ceram. Soc.*, **77** [3] 737-42 (1994).

[7] H. Solmon, D. Robinson, and R. Dieckmann, "Oxygen Transport in Aluminum Nitride Substrates," *J. Am. Ceram. Soc.*, **77** [11] 2841-48 (1994).

[8] J. H. Enloe, R. W. Rice, J. W. Lau, R. Kumar, and S. Y. Lee, "Microstructural Effects on the Thermal Conductivity of Polycrystalline Aluminum Nitride," *J. Am. Ceram. Soc.*, **74** [9] 2214-19 (1991).

[9] G. A. Slack, "Nonmetallic Crystals with High Thermal Conductivity," *J. Phys. Chem. Solids*, **34**, 321-35 (1973).

[10] M. Hirano, K. Kato, T. Isobe, and T. Hirano, "Sintering and Characterization of Fully Dense Aluminum Nitride Ceramics," *J. Mater. Sci.*, **28** [17] 4725-30 (1993).

[11] A. Virkar, T. B. Jackson, and R. A. Cutler, "Thermodynamic and Kinetic Effects of Oxygen Removal on the Thermal Conductivity of Aluminum Nitride," *J. Am. Ceram. Soc.*, **72** [11] 2031-42 (1989).

[12] K. Watari, M. Kawamoto, and K. Ishizaki, "Sintering and Chemical Reactions to Increase Thermal Conductivity of Aluminum Nitride," *J. Mater. Sci.*, **26**, 4727-32 (1991).

[13] R. C. Turner, P. A. Fuierer, R. E. Newnham, and T. R. Shrout, "Materials for High Temperature Acoustic and Vibration Sensors: A Review," *Appl. Acoustics*, **41** [4] 299-324 (1994).

[14] L. Zheng, S. Ramalingam, T. Shi, and R. L. Peterson, "Aluminum Nitride Thin Film Sensor for Force, Acceleration, and Acoustic Emission Sensing," *J. Vac. Sci. Technol. A*, **11** [5] 2437-46 (1993).

[15] M. Akiyama, K. Nonaka, K. Shobu, and T. Watanabe, "Crystal Orientation and Piezoelectricity of AlN Thin Films Prepared on Polycrystalline Substrates," *J. Ceram. Soc. Jpn., Int. Ed.*, **103**, 1084-86 (1995).

[16] C.-C. Cheng, Y.-C. Chen, H.-J. Wang, and W.-R. Chen, "Morphology and Structure of Aluminum Nitride Thin Films on Glass Substrates," *Jpn. J. Appl. Phys.*, **35**, 1880-85 (1996).

[17] M. S. Sandlin, K. J. Bowman, and J. Root, "Texture Development in SiC-Seeded AlN," *Acta. Mater.*, **45** [1] 383-96 (1997).

6. Conclusions

This thesis focused on improving the densification of two very different materials through the use of nanocrystalline processing. The first part of this thesis described how high-energy ball milling affected the phase transformation kinetics, densification, and microstructure of nanocrystalline alumina. Although nanocrystalline transitional aluminas are readily synthesized, they are usually difficult to densify due to the effects of phase transformation on grain size and porosity. Through high-energy ball milling, the nucleation density was greatly increased and a much more sinterable powder was achieved. The high-energy ball milling reduced the phase transformation temperature by >250°C, decreased the time required for transformation, and lowered the apparent activation energy for the transformation to 333 kJ/mol. The reliability of the Johnson-Mehl-Avrami-Kolmogorov (JMAK) kinetic analysis was examined by creating a finite particle model and analyzing the kinetics of the phase transformation as a function of particle size under both heterogeneous and homogeneous nucleation conditions. The JMAK results were found to be reliable even at small particle sizes (0.1 μm) when high seed densities (~10^{13} seeds/cm^3) were present in the system. Hot-pressed pellets from high-energy ball milled powders had a microstructure that was considerably different from that made from unmilled powders, and this difference was attributed to the increased nucleation density from milling. After low-temperature densification, pellets from milled powders consisted of dense and discrete grains with the porosity at the grain boundaries, where it could be easily removed during the final stages of densification.

The second part of this thesis focused on the synthesis and air-free processing of nanocrystalline AlN. Through the use of a forced-flow reactor, nanocrystalline AlN with crystallite sizes of 10-100 nm and surface areas of 45-370 m^2/g could be produced. Although the nanocrystalline AlN powders were highly moisture-sensitive (as shown by PA-FTIR studies), they could be processed and handled without exposure to air, thereby keeping the oxygen content as low as 0.6 wt% in fully dense samples. These powders showed excellent sinterability, achieving >95% of theoretical density after pressureless

sintering at 1700°C for 2 hours. The use of a high surface area Y_2O_3 powder as a sintering aid allowed comparable densities to be attained at a lower sintering temperature of ~1550°C. These findings compared very well to the best sintering results on AlN reported in the literature. The thermal conductivities of the densified pellets corresponded well to the best results in the literature attained under similar sintering conditions. Further improvements in thermal conductivity could be achieved by annealing at high temperatures and for extended periods in a highly reducing atmosphere for removal of trace oxygen in the AlN lattice. An additional noteworthy result was that powders produced at low reactor pressures in a He/NH_3 gas stream tended to form highly textured (002) pellets after hot pressing at 1900°C. Texturing of bulk, polycrystalline AlN is usually very difficult to achieve; hot pressing nanocrystalline AlN powders that contain needle-like particles may provide a new method for manufacturing high-temperature piezoelectric sensors.